# LOCAL MAGNETIC FIELD SYSTEM DESIGN AND CONTROL FOR INDEPENDENT CONTROL OF MULTIPLE MOBILE MICROROBOTS

A Dissertation

Submitted to the Faculty

of

Purdue University

by

Benjamin V. Johnson

In Partial Fulfillment of the

Requirements for the Degree

of

Doctor of Philosophy

May 2020

Purdue University

West Lafayette, Indiana

# THE PURDUE UNIVERSITY GRADUATE SCHOOL
# STATEMENT OF DISSERTATION APPROVAL

Dr. David J. Cappelleri, Chair

School of Mechanical Engineering

Dr. George T. Chiu

School of Mechanical Engineering

Dr. Babak Ziaie

School of Electrical and Computer Engineering

Dr. Dan Popa

School of Electrical and Computer Engineering, University of Louisville

**Approved by:**

Dr. Nicole Key

Head of the School Graduate Program

To Acha, Amma, Jacob and Rebecca

for all the love, support and prayers during my graduate studies.

# ACKNOWLEDGMENTS

I would like to express my sincere gratitude to my advisor, Prof. David J. Cappelleri for his continuous support, guidance, patience, and for providing the resources and environment for the course of this dissertation. I would like to thank the current and past members of the Multi-Scale Robotics Automation Lab who helped me through research discussions and valuable suggestions that helped shape this dissertation. I would like to especially thank Dr. Sagar Chowdhury for helping me transition to this work and for continuous guidance through discussions that extended beyond his stay at the lab. I am also grateful to Dr. Maria Guix Noguera for her expert guidance in the field of microrobotics that helped me broaden my point of view of the field. My workplace was made wholesome through the wonderful company of such colleagues and other members like Georges Adam, Vinoth Venkatesan, Ze An, Yang Ding, Cara Koepele, Nathan Esantsi, and Chenghao Bi.

I would like to acknowledge the support of Bert Gramelspacher from the Mechanical Engineering e-Shop for his help in the construction and debugging of the coil drive boards and circuits. I would also acknowledge the facility access at Purdue University's Birck Nanotechnology Center, and Dr. Neil Dilley for the use of magnetometry equipment. Quick turnaround of prototyping of mechanical components was also enabled through the support of Mr. Stephen Florence of the machine shop at Mechanical Engineering, who also provided an outlet in outreach to support the FIRST robotics community at Purdue.

I would also like to thank the National Science Foundation for providing financial support through NSF-IIS Award 1358446 which helped me conduct research uninterrupted. I would like to appreciate the School of Mechanical Engineering for the financial support during this work here, both with teaching assistantships and support through the Bilsland Dissertation Fellowship through the Purdue Graduate School.

I would also like to thank the staff and students at Purdue and the people of West Lafayette for a friendly and accepting atmosphere that helped make it my home away from home. I would like to thank Ninad, Maria, Rohit, Drupad, Raghu, Anand, Aswin, Anirudh, Shambhavi, Ashish, David, Dong, Kumaraguru and Shubhankar for the good company outside of the lab that helped me have a good time in West Lafayette.

Finally, I would like to thank my parents, Mr. Johnson Varughese and Dr. Shaly John, my brother Jacob, and my wife Rebecca, for their constant encouragement and prayers, and for teaching me that 'I can do all things through Christ who gives me strength'.

TABLE OF CONTENTS

Page

Page

Page

# LIST OF TABLES

# LIST OF FIGURES

Figure Page

Figure Page

Figure Page

Figure Page

# ABSTRACT

Johnson, Benjamin V. Ph.D., Purdue University, May 2020. Local Magnetic Field System Design and Control for Independent Control of Multiple Mobile Microrobots. Major Professor: David J. Cappelleri, School of Mechanical Engineering.

This dissertation describes the evolution of the different local magnetic field generating systems for independent actuation of multiple microrobots. A description of the developed hardware, system characterization tests, and experimental results are presented. The system is designed for automated control of multiple microrobots. Finally, sample micromanipulation tasks are demonstrated using the new microrobot design, showcasing its improved manipulation capabilities.

First, a mm-scale local magnetic field generating system designed for single layer coils is used to control 3.175 mm size N52 magnets as robots independently in the workspace. The controller used a set of local equilibrium points that were generated from a sequence of coil currents around the robots from one state to the next. The robots moved along paths computed through optimal control synthesis approach to solve complex micromanipulation tasks captured by global LTL formulas. However, the use of local equilibrium points as the states limited the motion of the robot in the workspace to simple tasks. Also, the interaction between the robots limited the robots to stay within far distances with each other. Hence a larger workspace based coil is designed to actuate up to four mm-scale robots in the workspace.

To improve the resolution of motion of these robots in the workspace, the mm-scale coils are modeled extensively. The forces generated by various coil combinations of the array are modeled and solutions for different actuation force directions are discovered for different locations in the coil. A path planning problem is formulated as a Markov decision process that solves a policy to reach a goal from any location in the workspace. The MDP formulation is also expanded to work when other robots are

present in the workspace. The formulation considers the interaction force between the robots and changes the policy to reach the goal location which reduces in the uncertainty of motion of the robot in the presence of interactions from other robots in the workspace.

The mm-scale coils are difficult to scale down for microrobotic applications and hence a new microscale local magnetic field system was designed. A new microscale local magnetic field system which consisted of two $8 \times 8$ array of coils aligned in two axes in two layers of a PCB was designed which could actuate robots as small as 1 $mm$ in the plane. The microcoils in the second layer are also able to generate sufficient magnetic field gradients in the workspace, while the traces below it are spaced adequately to eliminate their influence in the workspace. A new microrobot design also enabled the orientation control of the microrobot for performing micromanipulation tasks. However, only two robots could be independently actuated in this workspace due to interaction between the robots.

In pursuit of actuation smaller and multiple robots in a small workspace, a serpentine coil based local magnetic field generating system was designed to control of the motion of magnets as small as 250 $\mu m$. The net size of the robot is 750 $\mu m$ to enable orientation control and prevent tipping during motion. This system is capable of simultaneous independent closed loop control of up to 4 microrobots. The motion of the robot using the coils resembled that of a stepper motor which enabled the use of sine-cosine functions to specify currents in the coils for smooth motion of the microrobot in the workspace. The experiments demonstrated the capability of the microrobot and platform to simultaneously actuate up to four robots independently and successfully perform manipulation tasks. The ability to control the orientation of the magnet is finally demonstrated that has improved ability to perform manipulation tasks.

# 1. INTRODUCTION

## 1.1 Motivation

Mobile microrobots are small-scale agents which have dimensions less than 1 $mm$, where the dominant forces are microscale physical forces and effects. Inertial and bouyancy forces are negligible or comparable to surface area or perimeter forces such as surface tension, adhesion, drag and friction forces [1]. Traditional methods of microfabrication are long and arduous due to the limitations in 2.5D manufacturing techniques. Recently, other forms of micromanufacturing has led to the creation of more complex 3D structures. However, there is an interest in the assembly of small parts manufactured using such techniques [2]. Independent control of teams and swarms of microrobots can be used for collaborative and parallel control tasks such as: 1. manipulating single cells for arranging tissue scaffolds; 2. controlling functionalized microrobots for targeted drug delivery; or 3. manipulating microcomponents in order to realize low-cost additive manufacturing tasks. Independent control of the mobile microrobots will increase the speed and throughput of all of these tasks. A system capable of such independent control of multiple mobile microrobots will have applications in manufacturing, healthcare and bioengineering applications.

Microassembly and micromanipulation methods improve manufacturability of hybrid MEMS which integrate solid-state ICs with MEMS sensors and actuators [3]. Traditional methods use specialized microgrippers, fixtures, and positioning systems to assemble microparts. The key requirements of such microassembly systems are high precision and high throughput at low cost. This can be achieved through parallel manipulation and modular system designs [4]. Traditional micromanipulation involves two to four micromanipulators with point contacts that are coordinated to grasp an object and transport it to a goal location have been demonstrated in [5–10].

Rather than using multiple manipulators, a flexible microgripper attached to a multi DOF manipulator can be used to realize a pick-and-place operations as demonstrated in [11, 12]. Manipulator and micro-gripper based manipulation for micro-assembly operations based on micro snap fasteners has also been demonstrated [13–16]. These systems however are relatively large compared to the size of the workspace and have limited travel range which makes parallelization difficult. The design of smaller millirobots that can perform a wide range of assembly tasks such as micro-joining, electrical interconnection and micro-manipulation was demonstrated in [17].

Small-scale agents have the potential to assist in minimally invasive procedures that have several benefits to patients. Traditionally, these procedures have shown to reduce risk of infection, recovery time, medical complications etc. [1, 18, 19]. The ability to scale down from the current centimeter scale devices enables access to areas in the body that were previously difficult in an untethered form. Although, most of these concepts are in the concept stage, various examples of microrobots assisting in tasks include targeted drug/cargo delivery [20, 21], biopsy [22], sensing [23] and tissue scaffolding [24].

## 1.2 Background

With recent advances in microfabrication techniques, 3D printing, and robotics, microrobots for a variety of applications are being developed. In fact, several review articles have been published on mobile microrobotics in the past decade [1, 18, 25–33]. The main challenge to design a viable mobile microrobot is determining an effective power storage and locomotion system.

### 1.2.1 Actuation Methods

Representative power and actuation mechanisms applied to mobile microrobots include electrostatic [34, 35], thermal and optical [36–42], pieozoelectric [43], biological [44–48], electromagnetic [49–51], and combined piezoelectric-electromagnetic [52]

approaches. In this section, power and actuation methods for microrobots are discussed.

### Electrostatic Actuation

Electrostatic actuation uses the attraction between two surfaces when the circuit is charged. An example is the untethered MEMS microrobot powered through capacitive coupling with an interdigitated electrode array in [53]. Orientation control of this robot was also achieved by using a steering arm which could snap down at a higher voltage to pivot the robot to induce a rotation. This electrostatic control scaled favorably with size due to matching scaling of adhesive friction forces and electrostatic friction which aided in successful actuation [35]. However, these microrobots couldn't be driven backwards due to the surface properties and couldn't stay in place. Independent actuation of these robots using a global control signal were demonstrated in [54] through robots with varying properties that respond differently to the global signal. However the assemblies formed were of the robots themselves and did not demonstrate manipulation capabilities.

### Thermal Actuation

In [36], thermally induced curvature of legs of a microrobot lead to stepwise translation on low friction surfaces. However, they generate only pN level forces during actuation. In [37], cilia-like thermal bimorph actuator arrays which can be powered through a tether or an in-built battery pack generate walking gaits for the robot to move in the workspace. These robots are long (3 $cm$) and generate high heat during execution and are susceptible to surface roughness. In [55], chevron actuator based sub-mm sized robots were successfully actuated in the workspace combining stick-slip locomotion gaits with optically induced thermal actuation. Although these robots demonstrated ability to move in dry surfaces, their motions are slower and require a laser source.

### Optical Manipulation

Optical manipulation methods have been recently developed where a single laser beam is split into multiple paths with the help of a spatial light modulator or high speed mirror technology [39, 40, 42, 56–63]. Optical manipulation is achieved using holographic optical tweezers that function as special robot end-effectors that can manipulate single or a group of microparticles [39]. However, the parts that can be manipulated is limited to tens of nanometers to tens of micrometers. In [40], bubble microrobots that use infrared laser to assemble glass beads were demonstrated. However, the applications of optical tweezers are demonstrated for cleaning microfluidic chamber [41] and in the manipulation of biological cells [42]. The assembly of the beads took a long time due to issues with heating and releasing the beads during manipulation. Also, optical manipulation is only suitable for objects that are less than 10 $\mu m$ in size due to the very small actuation force (on the order of pico-Newtons) that can be generated by the laser beam.

### Biological Actuation

Biological actuation uses microorganisms such as bacteria or algae for actuation of microrobots. These microorganisms are capable of converting chemical energy to mechanical energy. In [46], flagellated bacteria employed as fluid actuators propel custom microstructures in low Reynolds number fluidic environments. In [48], flagellated bacteria is driven by chemical gradients generated using chemoattractant L-aspartate. These bacteria are used to carry payloads, which are microbeads as large as diameter 20 $\mu m$ in a microfluidic device. [47] has developed a MRI-based medical nanorobotic platform for tracking and closed loop control of magnetic nanoparticles or flagellated bacteria for target interventions in human capillaries. Many such biohybrid microrobots have been developed in the past decade, however they have key challenges in such as fabrication efficiency, and requires large swarms to carry sufficient payloads [64].

### Electro-Magnetic Actuation

In the past decade, several electromagnetic systems have been designed for the control of untethered mobile microrobots [65–73]. The microrobots used with these systems are made of either permanent magnetic, ferromagetic, or paramagnetic material and their designs are in most cases planar magnetic bodies. Any magnetic microrobot placed in the workspace of the electromagnetic control system will experience force and torque due to the applied magnetic field. Thus, the microrobots can be controlled by modulating the amount and direction of current administered to the magnetic coils surrounding the workspace. Microrobot actuation using magnetic field is possible in a variety of surfaces. In [49–51, 73], microrobots were actuated on dry surfaces using oscillating magnetic fields. Another approach is to use magnetic field gradients to pull the microrobots towards the coils. Such systems usually rely on an iron core to magnify the field gradients in the workspace. Several magnetic actuation systems [65, 71, 72, 74] are able to control the position and orientation of the robots without oscillating fields. The microrobots developed have demonstrated capabilities like cell manipulation [71], in-situ force sensing [70] etc.

Magnetic actuation is widely used in microrobotic actuation due to its ability to penetrate a wide range of materials. They are also relatively strong compared to other microrobot actuation methods. It is also easy to integrate magnetic materials in existing microfabrication methods [75]. In fact, several neodymium micro magnets are available commercially [76].

### 1.2.2 Indepedent Control of Multiple Microrobots

There has been much interest recently in attempting to control multiple microrobots independently, primarily using global magnetic fields [33, 77, 78]. A reconfigurable magnetic micromodule of dimensions less that 1 $mm$ in all directions which can be selectively immobilized by applying force through the electrostatic surfaces was presented in [79]. The control system used a combination of selective immobilization

of the microrobot modules from clamping forces provided by an electrostatic surface and mobilization of the microrobots through the use of external magnetic fields. The system was shown to be capable of the assembly and disassembly of the magnetic micromodules. However, it operated at slow speeds and can not handle simultaneous control of more than one microrobot at a time. The heterogeneity of magnetic microrobots smaller than 1 $mm$ in all directions was exploited in [80] to obtain individual control of the microrobots using a global magnetic field. While the non-uniformity of the microrobots magnetic properties allowed them to respond differently to the global field, their motions were still coupled. This approach also does not scale well to handle large numbers of microrobots.

A unique microrobot design consisting of two non-identical nickel bodies with the same magnetization direction was presented in [81]. The nickel bodies are attached to each other with a spring structure with the total dimension less than 300 $\mu m \times$ 300 $\mu m \times$ 70 $\mu m$. An oscillating magnetic field is used to compress the spring. During the part of the cycle when the magnetic field is off, the spring uncompresses which results in a driving force on the robot to propel it in a desired direction. By varying the natural frequency of the spring-nickel mass system, independent control of two microrobots was achieved. A controller design for these types of microrobots was developed in [82]. By taking advantage of the microrobot heterogeneity, the robots were able to be simultaneously controlled at different speeds moving in the same direction using one global input. Similarly, in [83], a global magnetic field was used to independently control two magnetic microrobots in the plane. However, fine control of the robot position and system singularities are issues with this approach. The work in [84] utilized the property that all magnetic microrobots orient according to a global magnetic field to control the local attraction and repulsive forces between nearby microrobots at a water-air interface for multi-agent formation control. The control of two microrobots was demonstrated in this manner. Again, these motions are inherently coupled through the use of the global magnetic field input.

Instead of using a single global magnetic field for multi-robot control, multiple local magnetic fields can be utilized instead. An array of solenoids was used to create local magnetic fields to control multiple cm-sized robots independently in [85]. Mm-scale magnetic robots have been actuated with magnetic fields with an array of traces on a printed circuit board in [86].

## 1.3 Objectives

The objective of this dissertation is to design and evaluate specialized substrates to generate local magnetic fields to independently control the position and orientation of multiple microrobots in a 2D plane. Three specialized substrates that can independently actuate multiple robots in the $\mu m$ scale and in the microscale are designed. These substrates generate sufficient fields in the workspace for the microrobots to perform manipulation tasks.

## 1.4 Contributions

In this dissertation, three novel localized magnetic field generating systems have been developed. They can generate localized magnetic fields in the workspace that enables actuation of multiple magnetic robots independently. The main contributions of this work include

- Design of novel local magnetic field generating systems
- Modeling and characterization of local magnetic fields generated by planar coils
- Development of a platform to control microcoils, host multiple local magnetic field generating systems, and control multiple microrobots
- Closed loop control of multiple microrobots in the workspace to perform assembly tasks

- Path planning of robots to avoid obstacles, considering other robots in the workspace
- New microrobot design to allow orientation control

In the following chapters, the modeling of planar coils and forces generated by such coils are discussed. Then, the experimental test-bed used to generate such local fields is presented. The following chapters describe a millimeter (mm) scale local magnetic field system, a micro ($\mu$) scale local magnetic field generating system, and finally a serpentine shaped coil based local magnetic field generating system. The characterization of coils, validation experiments, path planning for motion of the robots in the workspace, and demonstration experiments of capabilities of these systems are discussed. Finally, the future direction of this work is discussed.

# 2. LOCAL MAGNETIC FIELD MODELING

In this chapter, the magnetic forces generated by current carrying wires, that are to be configured for use as planar coils, on magnetic robots in their vicinity are studied. First, the magnetic field generated by current carrying wires are computed. The magnetic field gradients generated by these wires are then analyzed. Lastly, the requirements for robots to move based on these gradients are studied.

## 2.1 Magnetic Fields

In order to study the local magnetic force generated by the current carrying conductors, first, the magnetic fields generated by a single strip of wire is computed. The fundamental law that describe the magnetic field generated by a current carrying conductor, the Biot-Savart Law, which can described in SI units as:

$$\boldsymbol{B}(\boldsymbol{r}) = \frac{\mu_0}{4\pi} \int_C \frac{I\boldsymbol{dl} \times \boldsymbol{r'}}{|\boldsymbol{r'}|^3} \tag{2.1}$$

where $I$ is the current flowing through the wire, and $\boldsymbol{B}$ is the magnetic field generated at a point P at distance $\boldsymbol{r}$ from the origin. Planar coils can be modeled as segments of wire arranged either in the X or Y axis of the workspace, superimposing the fields to find the net field. Several wires combine together to form single coils, or

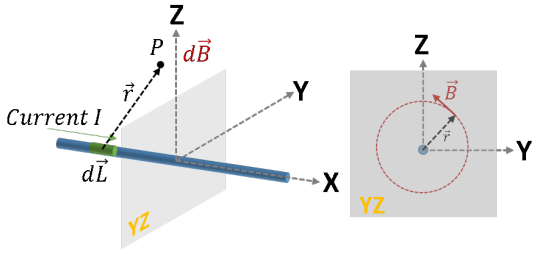


Figure 2.1. : Biot-Savaart law example

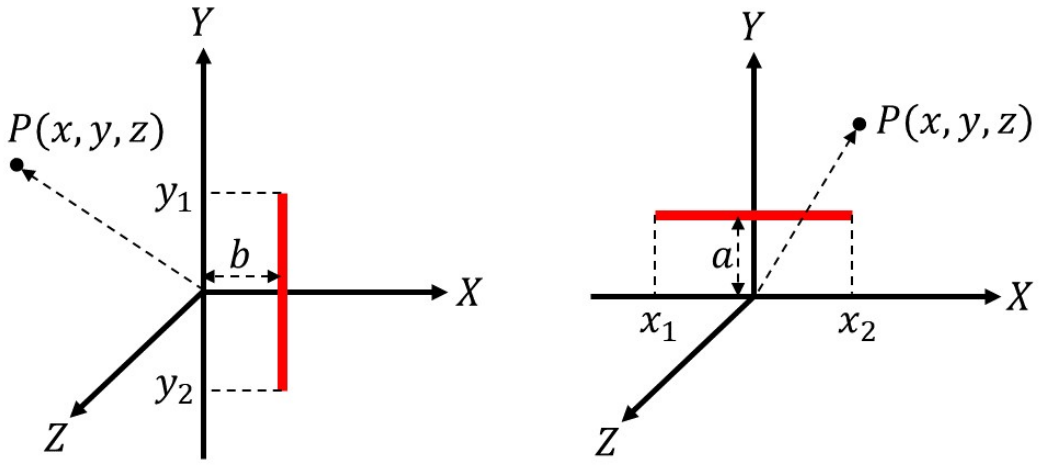


Figure 2.2. : Magnetic field modeling of microcoil: Microcoil orientated parallel to (a) YZ plane, and the (b) XZ plane.

single segments of wire can also act as planar coils. These segments are connected to the current controllers through traces, which create the underlying circuits needed for control. These traces are designed to be far away from the workspace and hence, for the analytical study, it is assumed that the magnetic field generated by these traces do not affect the magnetic field in the workspace.

For this analysis, a refined formulation of eq. 2.1 is used. Here, a simple cases of current carrying wires oriented along the X axis or Y axis (Fig. 2.2(a)) is considered for analysis. The magnetic flux $\mathbf{B} = [B_x, B_y, B_z]$ from the current carrying wire parallel to the Y axis, at a location $P(x, y, z)$ can be calculated as follows [87]:

$$B_x = -\frac{\mu_0 z I_c}{4\pi\left[(b-x)^2 + z^2\right]} \times \left[\frac{y_2 - y}{\sqrt{(y_2-y)^2 + (b-x)^2 + z^2}} - \frac{y_1 - y}{\sqrt{(y_1-y)^2 + (b-x)^2 + z^2}}\right] \tag{2.2}$$

$$B_y = 0 \tag{2.3}$$

$$B_z = -\frac{\mu_0(b-x)I_c}{4\pi\left[(b-x)^2+z^2\right]} \times \left[\frac{y_2-y}{\sqrt{(y_2-y)^2+(b-x)^2+z^2}} - \frac{y_1-y}{\sqrt{(y_1-y)^2+(b-x)^2+z^2}}\right] \tag{2.4}$$

Similarly, for a current carrying wire with the current flowing parallel to the X axis (Fig. 2.2(b)), the magnetic flux $\mathbf{B} = [B_x, B_y, B_z]$ at the location $P(x, y, z)$ can be calculated as follows [87]:

$$B_x = 0 \tag{2.5}$$

$$B_y = -\frac{\mu_0 z I_c}{4\pi\left[(a-y)^2+z^2\right]} \times \left[\frac{x_2-x}{\sqrt{(x_2-x)^2+(a-y)^2+z^2}} - \frac{x_1-x}{\sqrt{(x_1-x)^2+(a-y)^2+z^2}}\right] \tag{2.6}$$

$$B_z = -\frac{\mu_0(a-y)I_c}{4\pi\left[(a-y)^2+z^2\right]} \times \left[\frac{x_2-x}{\sqrt{(x_2-x)^2+(a-y)^2+z^2}} - \frac{x_1-x}{\sqrt{(x_1-x)^2+(a-y)^2+z^2}}\right] \tag{2.7}$$

$I_c$ is the current passing through the wire, $\mu_0$ is the permeability of the free space ($4\pi \times 10^{-7}\ Hm^{-1}$), and the parameters $x_1$, $x_2$, $y_1$, $y_2$, $a$ and $b$ are defined in Fig. 2.2.

For example, for a strip of wire which is 254 $\mu m$ wide, 860 $\mu m$ long and 35 $\mu m$ thick, carrying 0.2 A along the length of the wire is studied. The magnetic field generated by this wire along the X-axis at a height $z_0 = 150\ \mu m$ is compared to a FEM model based on COMSOL, and are shown in Fig. 2.3. The analytical model was found to be a good estimate of the distribution of the magnetic field in the workspace. The analytical equations 2.2 - 2.4 are useful in determining magnetic field gradients in the workspace which are directly proportional to the magnetic forces.

The peak intensity of magnetic field of such a strip of wire is $\approx 0.15\ mT(B_z)$ at the center of the wire. The intensity of $B_y$ is highest at either sides of the wire, about $\approx 0.07\ mT$. However, the direction of $B_y$ is opposite on either sides of the wire. The magnetic field gradients can be seen in Fig. 2.4. The intensity of $dB_x/dx$, and $dB_z/dz$ also change signs on either side of the width of the wire and produces a zero gradient at the center of the wire. The gradients $dB_x/dz$ and $dB_z/dx$ both produce higher

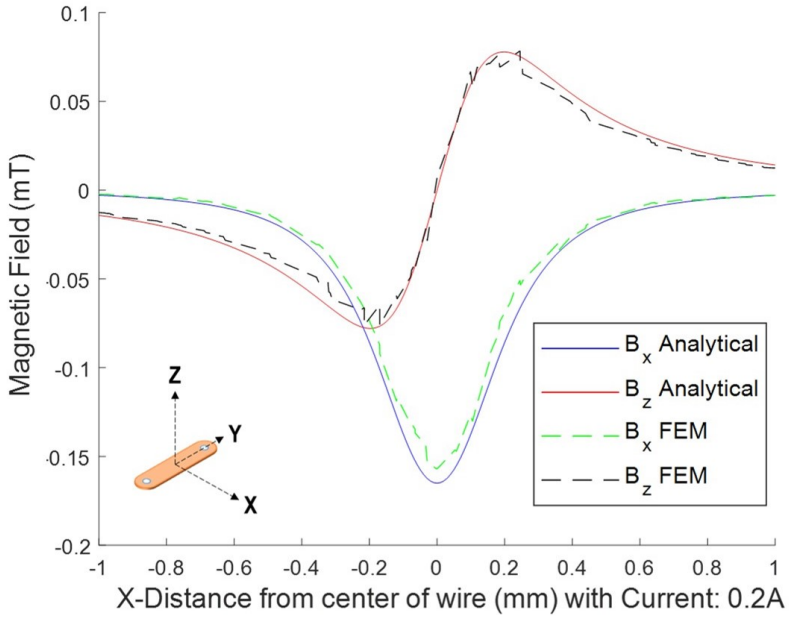


Figure 2.3. : Magnetic field along $z = 150\ \mu m, y = 0$ due to a strip of wire carrying 0.2 $A$ current along the Y axis.

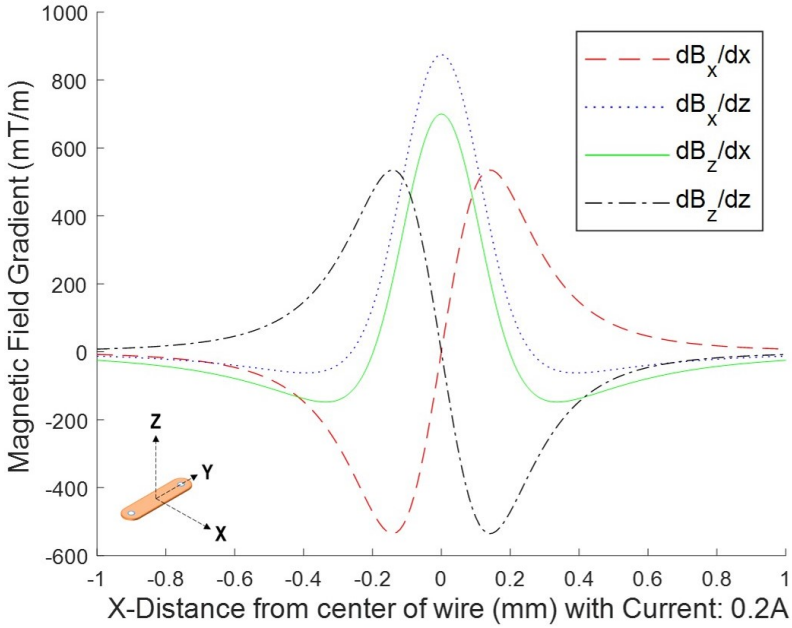


Figure 2.4. : Magnetic field gradients along $z = 150\ \mu m, y = 0$ due to a strip of wire carrying 0.2 $A$ current in the Y axis by differentiating analytical solution.

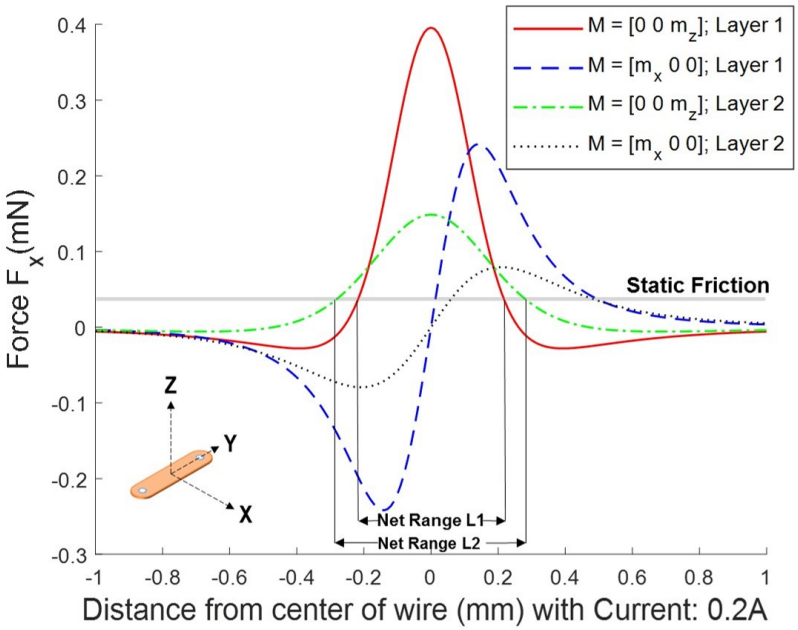


Figure 2.5. : Magnetic force along the X axis generated by a strip of wire for 0.2 $A$ current in the Y axis for a N52 disc magnet. Robots have magnetization along the X and Z, and the microcoils are in layer 1 or layer 2. The microcoil net actuation range is the distance on either side of the microcoil where the actuation force is greater than the static friction force.

field gradients of intensity $600 - 900\ mT/m$ at the center of the wire. However, the sign of the gradient changes outside a specific distance from the wire on either side of its thickness.

The magnetic field generated in the workspace by the single strip of wire is of the order of 0.1 $mT$. This field is insufficient to saturate soft magnetic materials, which require fields in the range of $3 - 5\ mT$ for full saturation. Instead, hard magnetic materials with inherent magnetization must be used as robots. Also, the magnetic field generated is low enough not to demagnetize such magnets.

## 2.2 Magnetic Forces

The magnetic force on a magnet, $\mathbf{F_{mag}}$, due to the magnetic field $\mathbf{B}(x, y, z)$ is a function of the field gradients and can be computed with the following equation:

$$\begin{aligned} \mathbf{F}_{mag} &= V_r(\mathbf{M} \cdot \nabla)\mathbf{B}(x, y, z) \\ &= V_r \begin{bmatrix} M_x \frac{\delta B_x}{\delta x} + M_y \frac{\delta B_x}{\delta y} + M_z \frac{\delta B_x}{\delta z} \\ M_x \frac{\delta B_y}{\delta x} + M_y \frac{\delta B_y}{\delta y} + M_z \frac{\delta B_y}{\delta z} \\ M_x \frac{\delta B_z}{\delta x} + M_y \frac{\delta B_z}{\delta y} + M_z \frac{\delta B_z}{\delta z} \end{bmatrix} \end{aligned} \tag{2.8}$$

where, $V_r$ is the volume of the magnet, $\mathbf{M}(M_x, M_y, M_z)$ is the magnetization of the magnet, and $\mathbf{B}(B_x, B_y, B_y)$ is the magnetic flux produced by the current carrying wire. It can be assumed, without loss of generality that the robots have magnetization in either their X (in plane) or Z axis(out of plane), and that the current carrying wire is parallel to the Y axis. This results in zero magnetic field, $B_y$, and zero magnetic field gradients associated with $B_y$. Considering, a N52 disc magnet of diameter 1 $mm$ and thickness 0.5 $mm$ with a magnetic flux density of 1.45 $T$, the magnetic force along the X axis when the magnetization is aligned in X or Z axis at two different heights in the Z direction is shown in Fig. 2.5.

## 2.3 Microrobot Dynamics

The forces generated in the workspace can be seen in Fig. 2.5. The peak forces in the X direction are at the center of the current carrying wire and they decreases at locations farther away from the center of the wire. The Z-direction forces are zero at the center of the wire and non-zero at either sides of the wire. For the same magnitude of current, the magnetic force generated on a magnet with magnetization in the Z direction has a larger range than the force generated on a magnet with magnetization in the X direction. Hence, the ideal robot is a magnet with magnetization in the Z direction.

The dynamics of the microrobot under the influence of a magnetic force $F_{mag}$ can be described by the following equation:

$$\mathbf{F}_{mag} - \mathbf{F}_{fric} - \mathbf{F}_{drag} = m\ddot{\mathbf{s}} \tag{2.9}$$

where $m$ represents the mass of the robot, $\mathbf{s}$ is the state/position of the robot, $\mathbf{F}_{fric}$ is the friction, and $\mathbf{F}_{drag}$ is the drag force, respectively. The drag force of a disc-shaped robot in size range of 0.50 $mm$ to 1.50 $mm$ in a workspace with fluid with a viscosity 100 $mPa.s$ is $10 - 60$ $nN$, which is negligible compared to the actuation forces. However, the net normal force on the robot is a sum of its weight and the maximum $F_z$ experienced, which is $\approx 0.26$ $mN$ at its peak. A dry surface with a friction coefficient of $\approx 0.5 - 0.7$ will significantly impact the motion of the robot. Therefore, a bed of fluid that reduces the frictional coefficient to $\approx 0.1 - 0.2$ is used. This results in a frictional force of $0.02 - 0.04$ $mN$. As shown in Fig. 2.5, the microcoil can provide approximately 0.4 mN of actuation force (for robots with magnetization along the Z-axis). This is enough to overcome the friction forces encountered and induce motion. Thus, the net actuation range of the microcoil is defined as the distance on either side of the microcoil where the actuation force is greater than the friction force.

## 2.4 Conclusions

In this chapter, the magnetic field, gradients and forces are studied for a planar coil. The peak forces along the plane are for magnets with magnetization aligned out of plane. This forms the basis of design of the microcoil systems and microrobots in this dissertation. The local forces generated are sufficient to actuate the robot in the workspace in the presence of surface forces.

# 3. EXPERIMENTAL TEST-BED CORE COMPONENTS

The experimental test-bed consists of the local magnetic field generating system, electronics, interface to communicate with the coils, and feedback systems that allow for closed loop control. Local magnetic field generating systems here are specialized substrates designed to actuate small-scale robots. They consist of traces of wire that form coils. These coils have the capability to exert sufficient forces on the robots in the workspace for smooth motion and manipulation tasks. In this dissertation, several such systems are presented. Chapter 4 and Chapter 5 introduces a millimeter (mm) scaled local magnetic field generating system for robots of size 3.175 $mm$. In Chapter 6, a magnetic field generating system capable of driving robots as small as 1 $mm$ was designed with 128 local coils that provide independent motion in any direction in the plane. Lastly, Chapter 7 considers a serpentine shaped coil system that is capable of actuating robots as small as 250 $\mu m$ in the workspace. These systems are designed for traditional and advanced PCB manufacturing techniques to reduce cost and improve compactness. The currents in these coils are controlled using the same set of core-components that are discussed in this chapter.

## 3.1 Electronics

The current in each coil is controlled independently using custom coil controller boards. Currently, the experimental setup has eight such controller boards which can control up to 128 coils. Each board controls up to sixteen coils individually, through individual motor control boards (DRV8838, Pololu Corporation). The motor control board controls the current on the basis of inputs from two separate boards, which are controlled by an Arduino microcontroller (Uno R3). The direction of current is provided by a voltage shifter I/O (SX1509, Sparkfun Electronics), and the magnitude

Table 3.1. : Coil Controller Boards

| Board No. | TCA PWM | PWM Board Addr | TCA I/O | I/O Board Addr |
|---|---|---|---|---|
| 1 | 7 | 0x7F | 6 | 0x3E |
| 2 | 7 | 0x45 | 6 | 0x3F |
| 3 | 7 | 0x79 | 6 | 0x71 |
| 4 | 5 | 0x7C | 4 | 0x3E |
| 5 | 1 | 0x60 | 0 | 0x3E |
| 6 | 1 | 0x61 | 0 | 0x3F |
| 7 | 3 | 0x7E | 2 | 0x3E |
| 8 | 1 | 0x63 | 0 | 0x71 |

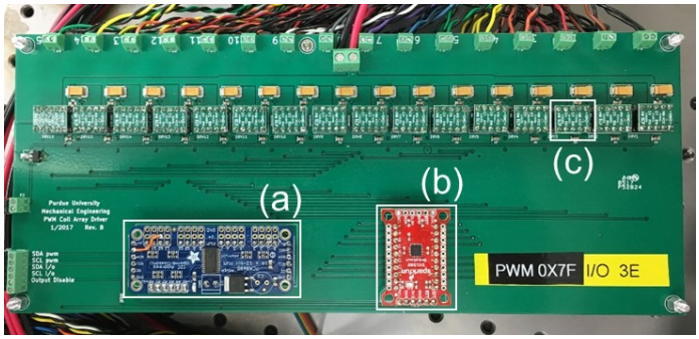


Figure 3.1. : Coil control electronics: coil control board. (a)PWM driver (PCA9685), (b)voltage shifter I/O (SX1509), (c) motor control boards (DRV8838)

of current is controlled by regulating the supply voltage using a PWM (Pulse Width Modulation) driver (PCA9685, Adafruit), which are both housed in the controller board and can each control sixteen coils at a time, as seen in Fig. 3.1. These boards have specific $I^2C$ addresses that enable the arduino to communicate to a specific board. The list of controller boards are shown in Table. 3.1.

The I/O board has only four possible $I^2C$ addresses available. Out of the four, the address 0x70 is an internal address for the PWM board, and hence would interfere with the communication with the arduino when used. To control eight I/O boards

with three addresses, a $I^2C$ multiplexer (TCA9548A, Sparkfun Electronics) is used to split the I2C signals to separate channels that can then be independently switched on to communicate with boards on that channel.

### 3.2 Power Supply

The motor driver provides currents up to 1 $A$ to each coil, and the external power supply (Mean Well RSP-320-2.5) can supply up to 60 $A$ of current to the system at 2.5 $V$. This allows for sufficient current to be supplied up to 60 coils at the same time, if needed. There are two such power supplies, each for 64 coils. In practice, only a few coils are activated at a time.

For a total of 64 coils, 4 controller boards are used. Each unit is connected to the workspace using a circular power connector. For the larger platform, a total of 121 coils were controlled using 8 controller boards. An Arduino Uno microcontroller is used to communicate with each controller board using I2C signals. The microcontroller is connected to a CPU with an Intel®Core™i7-4771 (3.50 GHz) processor and 16 GB RAM. All computations are performed using Matlab® and the commands are sent to the controller boards through the Arduino microcontroller interface.

### 3.3 Current Control

This coil controller cannot do current control based on the existing setup. To ensure the desired current intensities across a coil, the resistances of the coil has to be measured to apply the appropriate voltage. The resistances in the coils range from 0.70 Ω to 4.10 Ω due to varying length of traces and layers for each coil. Additionally, each controller board has a 2.20 Ω resistor in series to avoid high current generation in the coils. For a given coil, the output 12-bit PWM signal for a prescribed output current $I$ is given by

$$PWM = \frac{I \times R}{V_{max}} \times 2^{12} \tag{3.1}$$

where $V_{max}$ is the supply voltage, and $R$ is the resistance of the coil.

Table 3.2. : Decoded coils from the string from MATLAB.

| Sl. No. | Board Number | Coil Number | Direction | PWM Signal |
|---|---|---|---|---|
| 1 | 0 | 1 | 1 | 2457 |
| 2 | 0 | 2 | 1 | 2416 |
| 3 | 0 | 5 | 1 | 2252 |

### 3.4 Matlab-Arduino Interface

The coils can be controlled through MATLAB for open-loop and closed loop experiments. MATLAB communicates with the Arduino microcontroller to control the coils through the serial communication. The sequence of how MATLAB sends commands to operate the coils are shown below:

- The serial connection is initialized in MATLAB by creating an object which is used to write serial commands in the buffer. The microcontroller initializes the serial port with the same baud rate, and awaits the serial command from MATLAB.

- According to the control algorithm, MATLAB generates a string with information such as number of coils, boards numbers, coil numbers, and the PWM signal. Such a string is shown below:

  `'3,0,1,1,2457,0,2,1,2416,0,5,1,2252'`

- Once microcontroller recognizes that a serial command is available, it receives the string. It then decodes the string, where the first number denotes the number of coils that will be activated. The three coils and their details are shown in Table. 3.2

- After keeping the coils switched on for a prescribed amount of time, Matlab sends the switch-off signal which would send the 0 PWM values in a similar string.

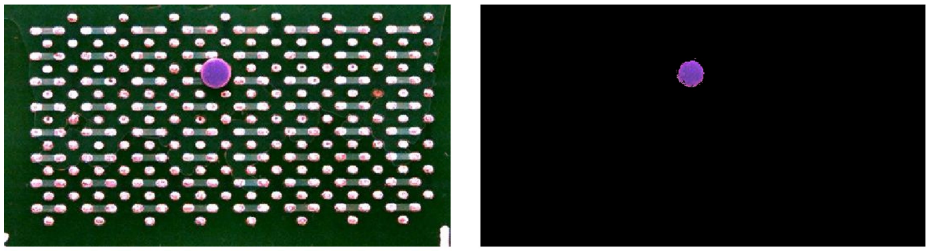


Figure 3.2. : (i) Image of the workspace captured by the camera. (ii) Image of the filtered image after image processing.

```
'3,0,1,1,0,0,2,1,0,0,5,1,0'
```

To ensure successful serial communication, longer strings are broken down to smaller segments.

### 3.5 Robot Tracking for Feedback Control

The view of the workspace is captured using an overhead CCD camera (FL3-U3-13E4C-C, FLIR Integrated Imaging Solutions Inc.). The positions of the coils are pre-calibrated and stored for reference. For tracking, the robots are colored on the side facing the camera with a color that is distinct from the background coils.

The image of the workspace can be taken up to 13 frames per second using Matlab, and up to 25 frames per second using Visual Studio. For fast image processing, simple RGB filter that separates the colors of the image returns centroid of blobs of the colors on the image with the robot as shown in Fig. 3.2. For position feedback, the mean position of a single blob would then give us the position of the robot in the workspace. In case of multiple robots, the robots are identified by the user in the beginning of the experiment, and every time a new image is taken and positions of the robots are figured, it is compared with the previous position and assigned the identity based on the closest position. Since the robots do not move long distances at an instant, do

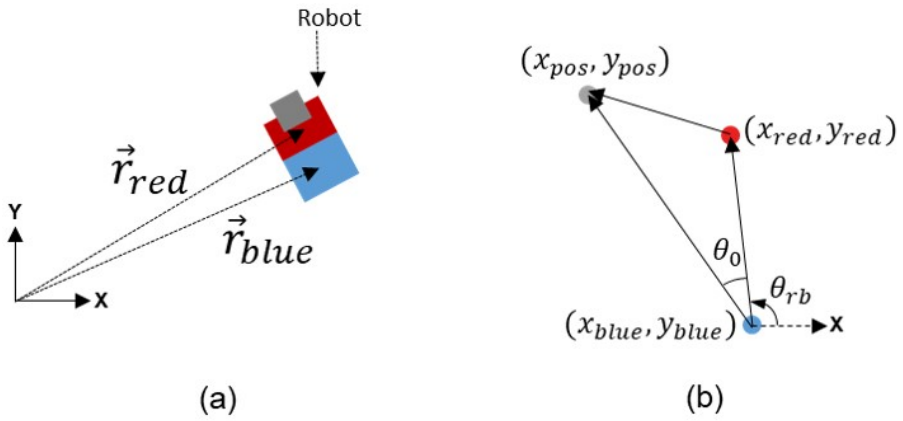


Figure 3.3. : (a) $\mathbf{r}_{red}$ and $\mathbf{r}_{blue}$ measured as centroids of the color segments. (b) $\mathbf{r}_{pos}$ measured from $\mathbf{r}_{red}$ and $\mathbf{r}_{blue}$, and the angle $\theta_{rb}$, of the vector from $\mathbf{r}_{blue}$ to $\mathbf{r}_{red}$ and the fixed angle, $\theta_0$.

not come close or cross over each other, the identities of the robots are conserved throughout the experiment.

For calculating position and orientation of the robots, a single point on the robot is insufficient. A second color is added to the robot to calculate the orientation of the robot. For advanced control, position of the magnet is also tracked to ensure accurate control of the magnet using the generated magnetic fields. To calculate the position and orientation of a microrobot from an overhead camera image, the position of the robot $r_{pos} = x_{pos}\hat{\imath} + y_{pos}\hat{\jmath}$ is assumed to be the location of centroid of the magnet and the orientation ($\theta_{pos}$) is calculated as the angle of the vector joining the centroid of the blue contour and the position of the magnet. The position of the robot is estimated using the tracked centroids of the red ($\mathbf{r}_{red} = x_{red}\hat{\imath} + y_{red}\hat{\jmath}$) and blue ($\mathbf{r}_{blue} = x_{blue}\hat{\imath} + y_{blue}\hat{\jmath}$) regions, as shown in Fig. 3.3(b)), using following equation:

$$\mathbf{r}_{pos} = \mathbf{r}_{blue} + |\mathbf{r}_{red} - \mathbf{r}_{blue}|(cos\theta_{pos}\hat{\imath} + sin\theta_{pos}\hat{\jmath}) \tag{3.2}$$

$\theta_{pos}$ is estimated using the angle of the vector formed by the centroids of the red and blue segments and the fixed angle $\theta_0$ (Fig. 3.3(b)) with:

$$\theta_{pos} = \theta_{rb} + \theta_0 \tag{3.3}$$

## 3.6 Conclusion

This chapter introduces the core components of the local magnetic field generating system. These components include the electronics, power supply, interface of the coils with the computer, and the measurement of position and orientation of the robots in the workspace. The electronics include controllers to regulate the current in 128 microcoils simultaneously. In the following chapters, these components are used with the newly developed magnetic field generating systems to control the microrobots in the workspace.

# 4. MM SCALE LOCAL MAGNETIC FIELD GENERATING SYSTEM

The first design presented is a mm Scale local magnetic field generating system designed for single layer coils. Since the coils have to be planar, they are designed for sufficient number of turns to generate force to drive the robot. To fabricate such planar coils with large number of turns, they have to be spiral in structure. This chapter[1] describes the modeling of such mm scale coils and independent control of multiple robots in this system.

To test the proof of concept for a local magnetic field generating system for independent microrobot control, a milli-scale version of such a planar spiral coil system was first fabricated in [89] using PCB manufacturing techniques. The coils are limited to the top layer of the PCB and the coils are controlled using vias which are routed at a distance from the coils. There are two versions of this platform; an $8 \times 8$ array of planar coils each with a dimension of 4.33 mm $\times$ 4.33 mm, shown in Table. 4.1(i); an $11 \times 11$ array of planar coils with dimensions of 5 $mm \times 5$ $mm$, used for more advanced experiments with larger numbers of robots, shown in Table. 4.1(ii).

## 4.1 Coil Design

To generate sufficient magnetic fields in the workspace, a planar coil with multiple turns was proposed. Each winding is rectangular in shape for the ease of fabrication. Each coil is capable of generating a local magnetic field that is dominant only in its vicinity. The final design of the coil is shown in Table. 4.1.

The first version of the magnetic field generating system is a $8 \times 8$ array of planar coils. In this version, each planar coil has a winding width of 178 $\mu m$, an out-of-plane

[1]The research presented in this chapter has appeared in [88] and is partially reproduced here.
[88] Y. Kantaros, B. V. Johnson, S. Chowdhury, D. J. Cappelleri and M. M. Zavlanos, "Control of Magnetic Microrobot Teams for Temporal Micromanipulation Tasks," in *IEEE Transactions on Robotics*, vol. 34, no. 6, pp. 1472-1489, Dec. 2018. 

Table 4.1. : mm Scale Magnetic Field Generating System

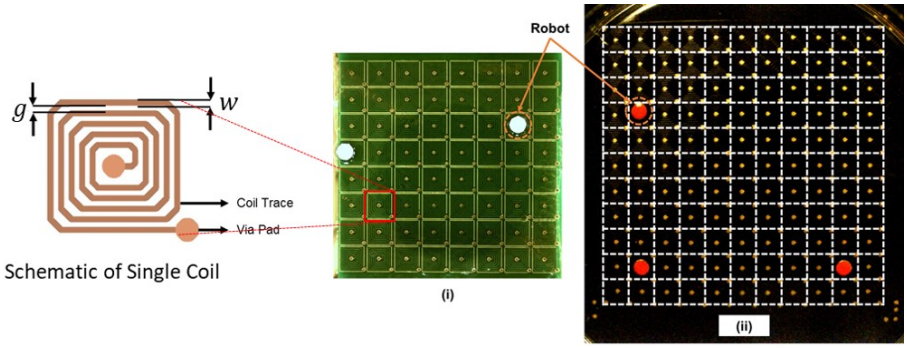


| Image Number | (i) | (ii) |
|---|---|---|
| References | [90, 91] | [88] |
| Coil Type | Spiral | |
| Number of coil layers | 1 | |
| Number of coils | 64 ($8 \times 8$) | 121 ($11 \times 11$) |
| Coil Dimensions | 4.33 $mm \times$ 4.33 $mm$ | 5.00 $mm \times$ 5.00 $mm$ |
| Coil Dimension ($w$) | 178 $\mu m$ | 254 $\mu m$ |
| Coil Dimension ($g$) | 178 $\mu m$ | 288 $\mu m$ |
| Coil Spacing | 4.33 $mm$ | 5.00 $mm$ |
| Workspace Dimensions | 41 $mm \times$ 41 $mm$ | 55 $mm \times$ 55 $mm$ |
| Movement Type | Discrete (2 $mm$) | |
| Robot Footprint | $\geq$ 2 $mm \times$ 2 $mm$ | |

winding thickness of 178 $\mu m$, and a winding spacing of 178 $\mu m$ with 5 turns. The coils and the traces are separated by a thick insulation layer of approximately 1.5 $mm$ which provides sufficient isolation.

The second version of the magnetic field generating system is a four layer printed circuit board (PCB) consisting of an $11 \times 11$ array of planar spiral coils (Table. 4.1(ii)). The additional layers were for ensuring that each coil could be independently controlled. The underlying traces in the bottom three layers connect each coil to an outlet. Each coil is 5 $mm$ long, 5 $mm$ wide, and has 5 turns. The wire traces are 152 $\mu m$ wide and 36 $\mu m$ deep, as shown in Fig. 5.1(a). The PCB has a top solder mask layer to protect the underlying circuits.

In both systems, the robots are controlled to move on a thin glass coverslip or a layer of teflon, while immersed in a layer of silicone oil providing a sufficient low-friction surface. This also insulates the coils from the working surfaces.

## 4.2 Robots

To be controllable in the workspace, the robot dimensions has to be in the order of the size of the coil. The robots used for the experiments are 3.125 $mm$ diameter and 0.79 $mm$ thick neodymium disc magnets. These magnets are of grade N42 and magnetized through their thickness. Multiple robots can move independently in this workspace provided they are approximately 15 $mm$ ($R_{I_{robot}}$) apart at all times. If they get closer than that, they repel/attract each other, affecting the robot's behavior if they are not in their equilibrium states. The motion of the robots are controlled by controlling the direction and magnitude of currents in the coils in the vicinity of the robot. These robots are placed with their north pole facing out of the plane of the PCB, with the top surface colored for ease in tracking.

## 4.3 Characterization Tests: Local Equilibrium Points

### 4.3.1 Local Equilibrium Point Modeling

The magnetic field generated by the a single planar coil can be evaluated by considering it as a series of finite wire segments in a spiral fashion. As discussed in Chapter 2, for a current carrying wire along the positive X-direction, a robot with peak magnetization in the positive Z-direction experiences force in the negative Y-direction. Thus, for a series of wires laid parallel to the X-axis, with currents all flowing in the same direction, the magnetic robot will translate in the negative Y-direction.

The currents in a spiral coil then will either repulse, force the robot outward, or attract, pull the robot towards its center, depending on the direction of current flowing through the coil. The net forces on a robot for a fixed direction of current are shown in Fig. 4.1(a) and (b). Another way to look at the coil, is to assume that the coil is an electromagnet with magnetic moment that depends on the current flowing through the coil and the number of turns. When the robot has attractive potential, it is like the coil having a magnetic moment in the same direction as that of the robot. This will attract the robot if it's inside the bounds of the coil. Meanwhile, if the robot is out of the bounds of the coil, the coil and robot will repel each other like two magnets aligned parallel in the workspace. Therefore, a repulsive potential generated by the coil will push the magnet to the outer border of the coil.

### 4.3.2 Robot Motion

To define waypoints (goal locations) for the robot, it is important that they are at local equilibrium points, i.e points of lowest magnetic potential. This ensures that the robots do not deviate in the influence of other robots or disturbances in the workspace. In previous work [91], it was believed that these equilibrium points only existed at the center of each coil, limiting the waypoints for path planning

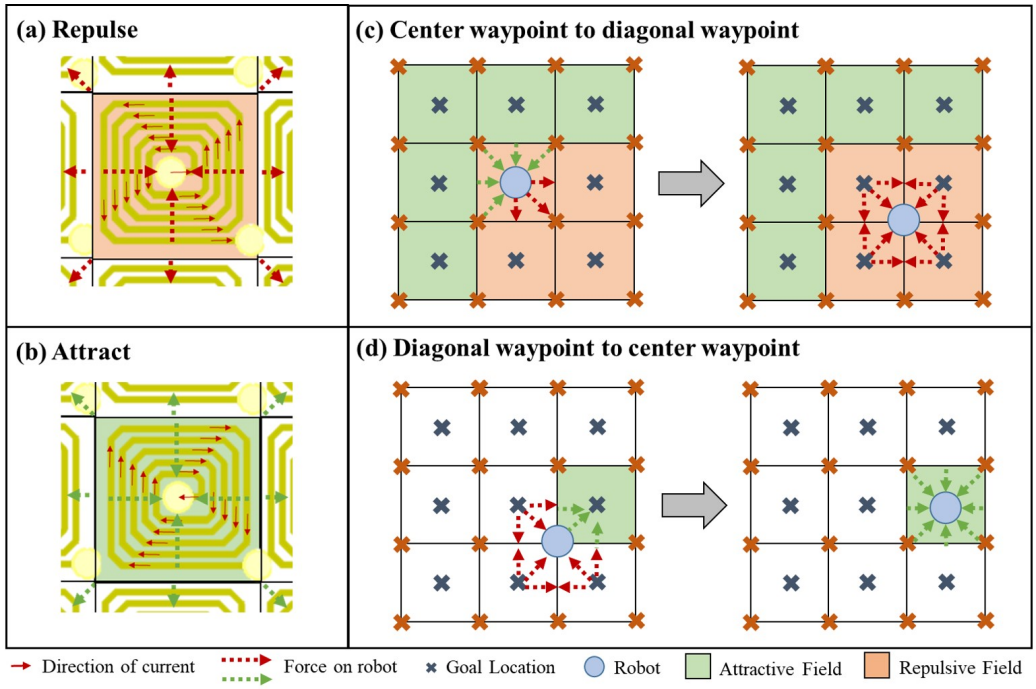


Figure 4.1. : Local magnetic field actuation. (a) Repulsive force due to clockwise wire current. (b) Attractive force due to anti-clockwise current in the planar coil. (c) Coil actuation states needed to actuate a microrobot to a diagonal waypoint from a center waypoint; (d) States needed to actuate a microrobot to a center waypoint from a diagonal waypoint.

and trajectories to orthogonal moves in the workspace. Here, additional equilibrium points were identified at the corner positions of each coil (diagonal positions in the workspace). The robot remains in the center of the coil if the coil "attracts" the robot, and it remains in the diagonal (corner) position if all the surrounding coils "repel" the robot. However, to reliably move from a center waypoint to a diagonal waypoint, all nine neighboring coils of the robot are needed, as shown in Fig.4.1(c). The repulsing coils push the robot to the diagonal goal while the outer surrounding attracting coils help direct the robot towards the diagonal. Since the robot is outside the borders of these attracting coils, they actually repulse the robot.

This makes sure that the robot moves in a predictable manner to the diagonal waypoint. In order to move from a diagonal waypoint to a center waypoint, the robot

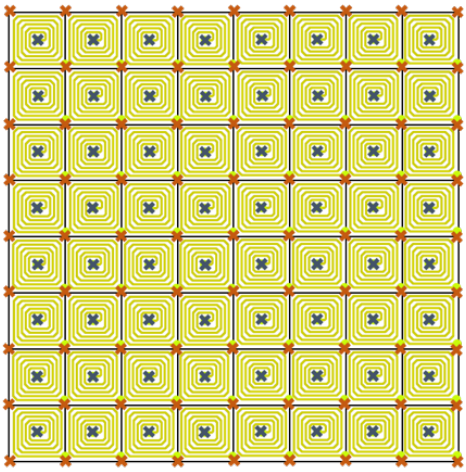

Figure 4.2. : Schematic of 8 × 8 planar magnetic coil array. Waypoints for the developed path planning algorithm consist of each coils center and corner (workspace diagonal) positions, all marked with an "x".

simply has to reside in the influence radius, $R_{I_{coil}}$, of the corresponding coil. It will then get pulled to the the static equilibrium at the center of the attracting coil, as shown in (Fig. 4.1(d)). All of these possible center and diagonal equilibrium points in the workspace yield the potential waypoints for path planning, and are denoted with 'x' in Fig. 4.2 for the 8 × 8 coil platform.

### 4.3.3 Validation Experiments

The first set of experiments conducted were to validate the models of the system presented in Section 4.3. It was confirmed that the magnetic robots have two types of static stable equilibrium points in the workspace: 1. the center of a coil when its attracting the robot, which is referred to as the *center*; and 2. the midpoint of the common diagonal of any four coils, which is referred to as the *diagonal*. This was validated by manually perturbing the robot after it reaches the equilibrium point after either a center or diagonal move and checking if the robot returns to its equilibrium

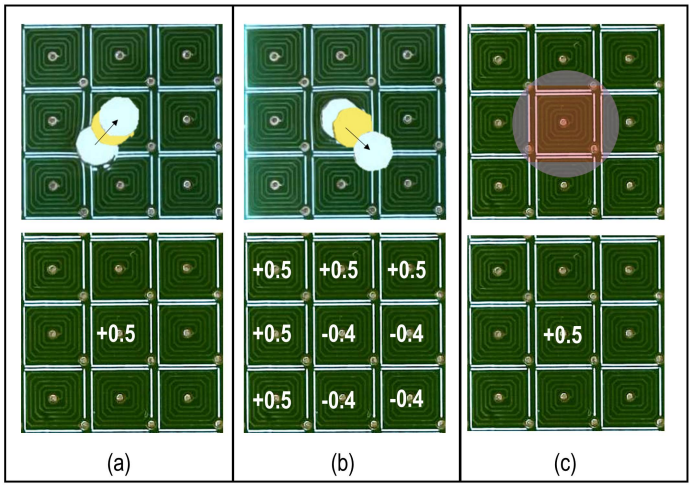


Figure 4.3. : Validation tests for (a) *center* and (b) *diagonal* moves. The direction (+ for attractive and − for repulsive potential) and magnitude of the current in Amps are shown below each moves. (c) $R_{I_{coil}}$ influence region for a coil. Red denotes region of attraction, and blue denotes region of repulsion for the current flowing in the clockwise direction.

position (Fig. 4.3(a),(b)). Also, the $R_{I_{coil}}$ influence region was measured for which the stable equilibrium is maintained for the task and is shown in Fig. 4.3(c).

The centering equilibrium point can qualitatively withstand larger perturbation forces because of the local strength of the field holding the robot in the center when compared to field applied to create a diagonal equilibrium point. The diagonal point is a result of four coils being activated which are pushing the robot away from each other. Although there are four coils, only eight traces are involved in actively pushing the robot, resulting in a weaker equilibrium point. The centering coil has sixteen traces pushing the robot to the center. This makes the diagonal equilibrium point more susceptible to errors from disturbances or uncertainties in the workspace.

## 4.4 Feedback Control

The applied magnetic force to the robots is directly proportional to the current in the coil. The current can vary from 0 to 1 A. The robot can move due to currents as low as 2.5 mA for a grade N52 disc magnet, but is slow and has a tendency to get stuck or deviate from its desired trajectory in the presence of external forces. At higher currents, the robots move faster to their equilibrium positions due to higher gradient fields and have better static equilibrium strength. However, the range $R_{I_{coil}}$ of the coils does not change as much with increased current due to the inverse square relationship of the field strength with the distance from the coil. Experimental tests have validated the robot moving from a diagonal waypoint to a center waypoint as well as the robot moving from a center waypoint to a diagonal waypoint.

The currents in the coils around the robot generates potentials which result in forces as described in Fig. 4.1. If the robot does not reach the local equilibrium point at the point of feedback, the motion control keeps the coils switched on longer and waits for the robot to eventually reach the equilibrium state. The values of the currents used to reach the equilibrium states for the validation tests are shown at the bottom of Fig. 4.3.

For closed loop control, Algorithm 1 is used to find the coils that need to be activated at a given current state $\mathbf{s_{curr}}$ and desired state $\mathbf{s_{des}}$. In cases where the robot strays from the defined path, this algorithm will bring it back to the desired waypoint based on a simpler planner.

## 4.5 LTL Task Specification and Constraints

When multiple magnetic microrobots move in the workspace, their interaction forces demand the path planning to have temporal constraints. Hence, the waypoints for the multi-robot case are computed as a temporal task, using Linear Temporal Logic(LTL). As the microrobots move to accomplish the assigned temporal task, the distance between them to be always greater than $R_{I_{robot}} > 0$, where $R_{Irobot}$ is the

**Algorithm 1** CoilActuation(): Actuate coils to reach goal.

**Input:** Current state of the robot, $\mathbf{s_{curr}}$, desired state, $\mathbf{s_{des}}$, computed by the planner, states near the robot$\mathbf{S_m}$, the microcoil array $C_n$, waypoint threshold, $W_{th}$, and the search update time, $t_c$.

**Output:** Desired microcoils $c_m \in C_n$ (a set of $m$ number of microcoils) that need to be activated and associated polarities $\{P_i\}_{i=1}^{m}$ .

1: **while** $\| \mathbf{s}_{des} - \mathbf{s}_{curr} \| \geq W_{th}$ **do**
2: $\mathbf{e} \leftarrow \mathbf{s}_{des} - \mathbf{s}_{curr}$
3: **if** $\| \mathbf{e} \| \geq R_{goals}$ **then**
4: Find all states $S_j$ near $\mathbf{s_{curr}}$, such that $\| \mathbf{s}_m - \mathbf{s}_{curr} \| \leq 1.2 \times R_{goal}$
5: Find $s_{des} \leftarrow \max_{\forall s \in S_j}(s_j - s_{curr}) \cdot \hat{\mathbf{e}}$
6: **end if**
7: $c_m \leftarrow$ ChooseAction$(\mathbf{s_{des}}, \mathbf{s_{curr}}, C_n)$
8: Activate microcoil $c_m$ for update time $t_c$.
9: Get feedback of the current state of the robot, $\mathbf{s_{curr}}$.
10: **end while**
11: **return** $c_m \in C_n$ and $\{P_i\}_{i=1}^{m}$ .

radius of influence of a robot with respect to another in the same workspace. Robots closer together than $R_{Irobot}$ will attract or repel each other. This way, it is ensured that the magnetic fields used for mobility of robot $i$ do not induce movement of any robot $j \neq i$. This requirement can encapsulated by the following LTL statement.

$$\phi_c = \square \neg_{\forall i,j} (\|\mathbf{x}_i(t) - \mathbf{x}_j(t)\| \leq R_{Irobot}) \tag{4.1}$$

The robots themselves interact between each other due to their magnetization. This influence region between the robots, $R_{I_{robot}}$, can be reduced by using lower grade magnetic robots. For example, the experiments showed that a N52 grade robot can have an $R_{I_{robot}}$ up to 20 mm while a N42 grade robot has a $R_{I_{robot}}$ of 15 mm. Demagnetization of the robots can reduce their influence regions ($R_{I_{robot}}$) but it will

**Algorithm 2** ChooseAction(): Find action.

**Input:** Current state of the robot, $\mathbf{s_{curr}}$, desired state, $\mathbf{s_{des}}$, computed by the planner, the microcoil array $C_n$, error vector $\mathbf{e}$

**Output:** Desired microcoils $c_m \in C_n$ (a set of $m$ number of microcoils) that need to be activated and associated polarities $\{P_i\}_{i=1}^{m}$ .

1: **if** $\mathbf{s_{des}} \in C_n$ **then**
2: $c_m \leftarrow$ MoveCenter($\mathbf{s_{curr}}$)
3: **else**
4: $c_m \leftarrow$ MoveDiagonal($\mathbf{s_{curr}}$)
5: **end if**
6: **return** $c_m$.

**Algorithm 3** MoveCenter(): Move to the center of a coil.

**Input:** Current state of the robot, $\mathbf{s_{curr}}$, desired state, $\mathbf{s_{des}}$, computed by the planner, the microcoil array $C_n$, waypoint threshold, $W_{th}$, and the search update time, $t_c$.

**Output:** Desired microcoils $c_m \in C_n$ (a set of $m$ number of microcoils) that need to be activated and associated polarities $\{P_i\}_{i=1}^{m}$ .

1: Find $c_{attract} \leftarrow \max_{\forall c \in C_n}(c_n - s_{curr}) \cdot \hat{\mathbf{e}}$
2: $C_{repulse} \in C_n - C_{attract}$
3: **return** $C_{attract}, C_{repulse}$

**Algorithm 4** MoveDiagonal(): Diagonal action.

**Input:** Current state of the robot, $\mathbf{s_{curr}}$, desired state, $\mathbf{s_{des}}$, computed by the planner, the microcoil array $C_n$, waypoint threshold, $W_{th}$, and the search update time, $t_c$.

**Output:** Desired microcoils $c_m \in C_n$ (a set of $m$ number of microcoils) that need to be activated and associated polarities $\{P_i\}_{i=1}^{m}$ .

1: Find $c_{repulse} \leftarrow \forall c \in C_n$ such that $(c_n - s_{des}) \leq 1.8 \times R_{goal}$
2: $C_{attract} \in C_n - C_{repulse}$
3: **return** $C_{attract}, C_{repulse}$

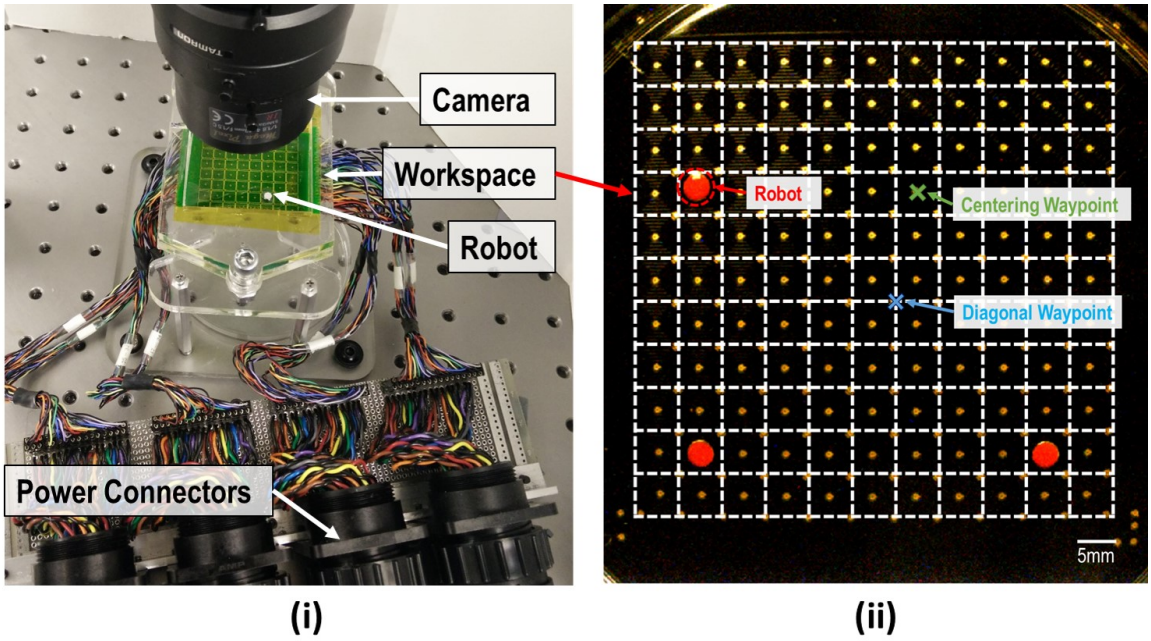


Figure 4.4. : (i)Experimental setup showing $8 \times 8$ coil (ii) Workspace view of $11 \times 11$ coil

also affect the performance of the robot since their influence from the surrounding coils, $R_{I_{coil}}$, is diminished due to their reduced magnetization. The experimental results discussed in this chapter is based on the solution to the LTL problem developed in [88].

## 4.6 Multi-Robot LTL Experiments

### 4.6.1 Experimental Setup

The view of the workspace is captured (Fig. 4.4(i)) using an overhead CCD camera (FL3-U3-13E4C-C, FLIR Integrated Imaging Solutions Inc.). The possible waypoints in the workspace are plotted on the image and the robots are identified using background subtraction and Hough transform techniques. The possible waypoints are shown in Fig. 4.4(ii). Each robot is also colored white or red to improve the image

detection algorithm accuracy as shown in Fig. 4.4. With these image processing algorithms and Matlab's Image Acquisition toolbox, the vision system is able to run at 13 frames per second.

### 4.6.2 Two Robot LTL Experiment

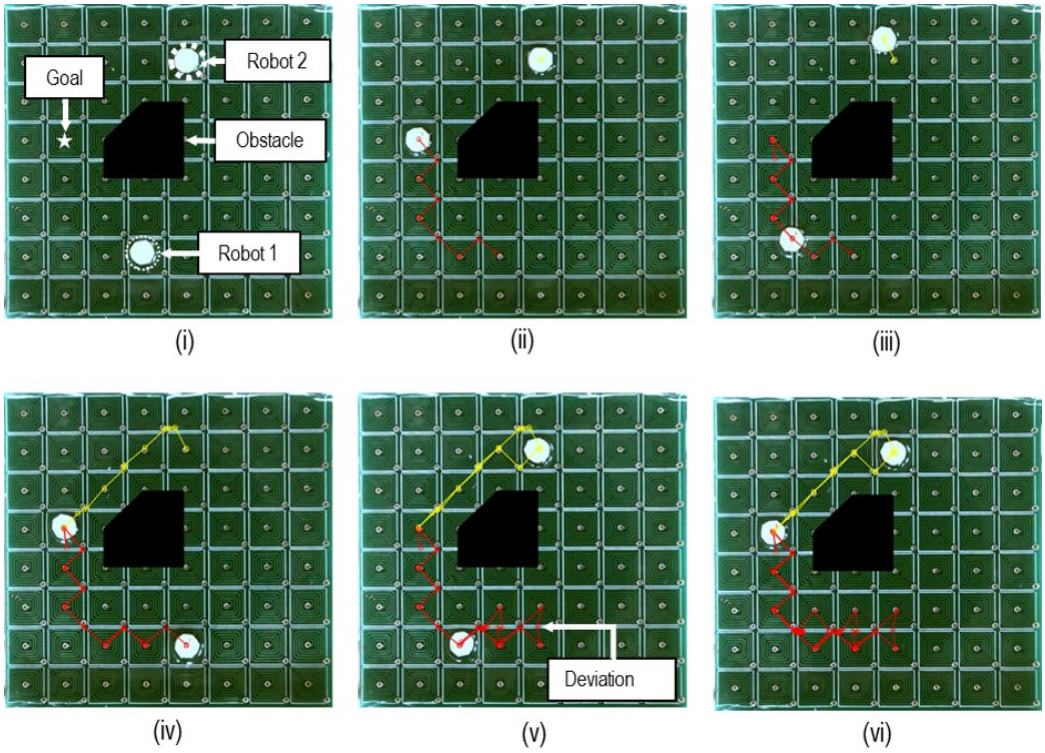


Figure 4.5. : Two-robot LTL experiment: Two robots move in the workspace to reach the goal location marked with a $\star$, while avoiding an obstacle in workspace. For the prefix goal, Robot 1 goes towards the goal location while Robot 2 stays in place (i),(ii). Next, as suffix motion, Robot 1 returns to it's original position and Robot 2 moves towards the goal location (iii),(iv). Robot 2 then goes back to its original position and robot 1 moves to the goal location (v),(vi). For this task, the suffix motion then repeats infinitely.

An experiment of two robots moving in the 8×8 workspace using the LTL planning algorithm presented in [88] is illustrated in Fig. 4.5. Here, two robots where the assigned LTL-based task is considered

$$\phi_{\text{task}} = (\square\Diamond\pi_1^0) \wedge (\square\Diamond\pi_1^*) \wedge (\square\Diamond\pi_2^0) \wedge (\square\Diamond\pi_2^*) \wedge (\square(\neg\pi_{\text{obs}})) \tag{4.2}$$

where the atomic propositions $\pi_1^*$ and $\pi_2^*$ are true if robot 1 and 2 are in the location denoted by $\star$ in Fig. 4.5, respectively. Similarly, the atomic propositions $\pi_1^0$ and $\pi_2^0$ are true if robot 1 and 2 are in the initial locations. In words the LTL formula (4.2) requires both robots to (a) visit the location $\star$ infinitely often, (b) visit their respective starting positions infinitely often, and (c) avoid the obstacles in the workspace. Also, the robots need to satisfy the constraints imposed by $\phi_c$ defined in (4.1). In Fig. 4.5, the prefix and suffix part of the synthesized plan follow: Prefix: (i) Robot 1 moves towards the $\star$ goal location while Robot 2 stays in its position. (ii) Robot 1 reaches the goal location and the prefix is completed. The suffix parts starts from (ii), (iii) Next, robot 1 returns to its starting position while Robot 2 moves towards the $\star$ position. (iv) Robot 1 reaches its starting position and Robot 2 reaches the target goal location at $\star$. (v) Robot 1 goes back to the $\star$ position while Robot 2 goes back to its original position. (vi) The robots are again in the initial suffix state shown in (ii) and the loop continues.

Note that the algorithm dictates Robot 2 to move along a diagonal trajectory in order to travel along the shortest path to the goal. By observing the trajectories in the experiment, it can be observed that the minimum robot spacing distance during each experiment is greater than the prescribed value (constraint) of $R_{I_{robot}}$.

### 4.6.3 Three Robot Experiment

An experiment of three robots moving in a workspace as in the simulation study in [88] is illustrated in Fig. 4.6 and Fig. 4.7. The three robots in the workspace are represented by the colors red(r), blue(b), and green(g). The goal locations 88 and 42

are shown as red color $\star$, 88 and 25 are shown as green color $\star$, and 24 and 12 are shown as blue color $\star$ in Fig. 4.6(i)(a). The LTL based task is described in (4.3).

$$\begin{aligned}\phi_{\text{task}} =&(\square\lozenge\pi_r^{\mathbf{c}_{42}}) \wedge (\square\lozenge\pi_r^{\mathbf{c}_{88}}) \wedge (\square\lozenge\pi_g^{\mathbf{c}_{88}}) \wedge (\square\lozenge\pi_g^{\mathbf{c}_{24}}) \\ &\wedge (\square\lozenge\pi_b^{\mathbf{c}_{24}}) \wedge (\square\lozenge\pi_b^{\mathbf{c}_{12}}) \wedge (\square(\neg\pi_{\text{obs}})).\end{aligned} \tag{4.3}$$

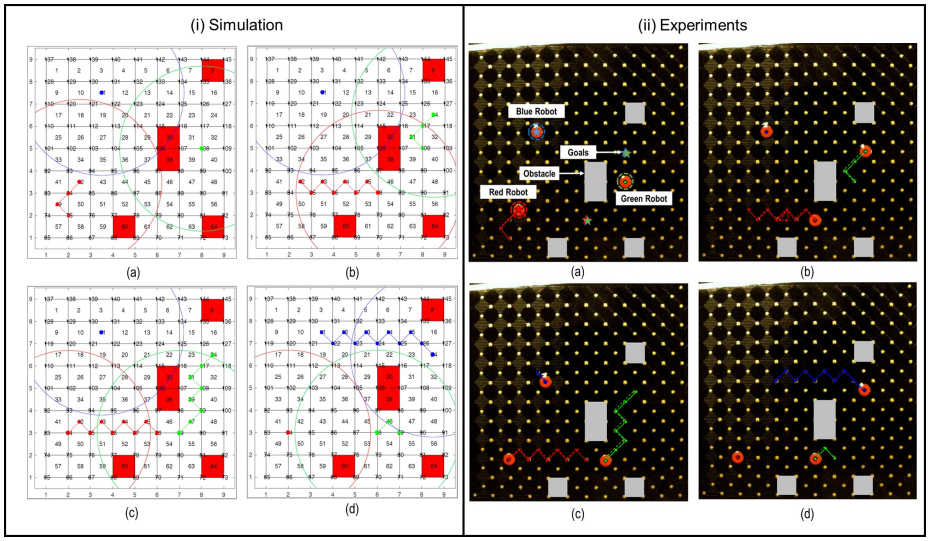


Figure 4.6. : Prefix motion of the three robot simulation(i) and experiment(ii) from Case Study II in [88]. (a),(b),(c), and (d) represent the progress of the robots at various states during the LTL motion. The paths of each robot are represented by their color, while the goals are shown as $\star$ in (a).

In words, this LTL-based task requires: (a) the red robot to move back and forth between locations $\mathbf{c}_{88}$ and $\mathbf{c}_{42}$ infinitely often, (b) the green robot to move back and forth between locations $\mathbf{c}_{88}$ and $\mathbf{c}_{24}$ infinitely often, (c) the blue robot to move back and forth between locations $\mathbf{c}_{24}$ and $\mathbf{c}_{12}$ infinitely often, and (d) all robots to avoid the obstacles in the workspace.

Fig. 4.6(i) and Fig. 4.7(i) show the prefix and suffix simulations generated in [88]. From the experimental trajectories in Fig. 4.6(ii) and Fig. 4.7(ii), it is confirmed that

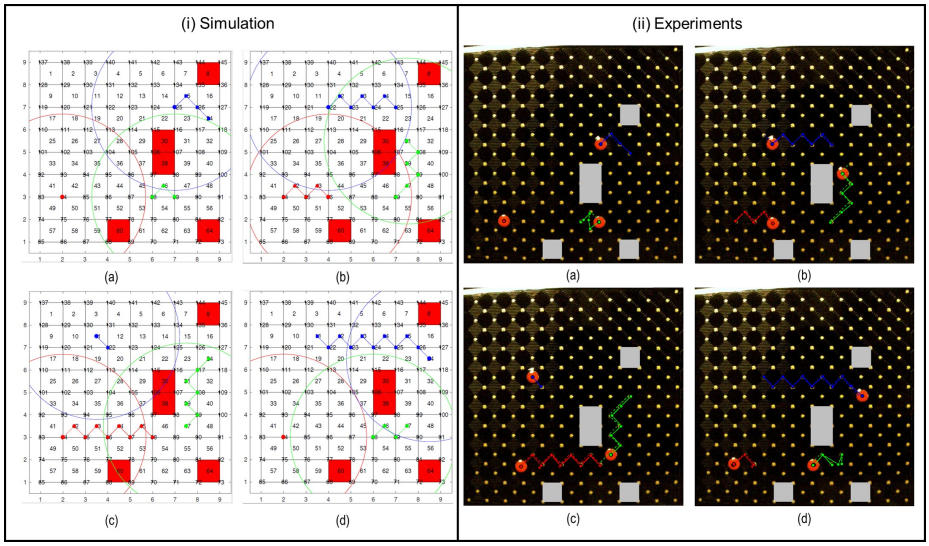


Figure 4.7. : Suffix motion of the three Robot simulation(i) and experiment(ii) from Case Study II in [88]. (a),(b),(c), and (d) represent the progress of the robots at various states during the LTL motion. The paths of each robot are represented by their color, while the goals are shown as $\star$ in (ii).

the robots maintained the minimum spacing distance while avoiding the obstacles to reach the respective goals.

### 4.6.4 Advanced Multi-Robot Experiments

A series of advanced multi-robot experiments have been conducted to explore the capabilities of the system and an actual assembly task. The results of some of these are shown in Fig. 4.8. First, an experiment of four robots moving independently in the workspace is demonstrated. The task is for the four robots to move clockwise to the starting location of the next robot. The starting positions, intermediate, and final paths of the robots are shown in Fig. 4.8(a),(b), and (c), respectively.

The ability of this system to conduct an assembly task has also been demonstrated, as shown in Fig. 4.8(d)-(f). In this experiment, two robots fitted with 3D printed end-effectors were used to assemble two hexagonal parts. The end effector and the

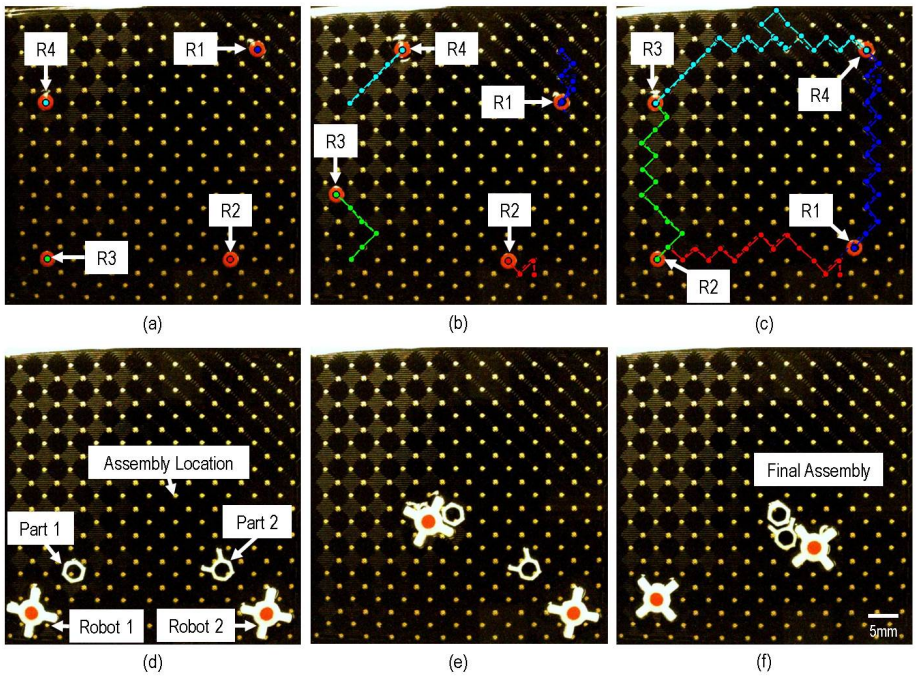


Figure 4.8. : Advanced multi-robot experiments: (a)-(c) Four-robot experiment where the robots R1, R2, R3, and R4 move clockwise to the starting location of the next robot. The paths of each robot are represented in different colors. Two robot assembly task: (d) each robot is fitted with a 3D printed end-effector to push other parts. (e) Robot 1 pushing Part 1 to the assembly location. (f) Robot 2 pushing Part 2 to the assembly location and ensuring correct orientation of part.

assembly parts were both printed using the Connex 350 (Stratasys Ltd.). printer with Vero White material. The robots were able to sequentially push the parts to the assembly location. The paths for the robots were specified on the basis of the positions of the parts. Here, this system cannot control the orientation of the robot, however position control was sufficient to position and orient the parts to form the required assembly.

## 4.7 Discussion and Conclusion

In this chapter, milli-scale robots were controlled using planar coils. A set of equilibrium points were identified in the "center" and "diagonal" positions of an array of planar coils, which were used as robustly achievable states. A maximum of 9 coils are activated to ensure that the robots transition between these two equilibrium states. For a given state, four 'actions' are possible, which moves the robot to the adjacent state. The successful implementation of a temporal task using four such robots in the workspace was also demonstrated. However, the robots were kept far enough from each other to avoid interactions that affect the motion to these "center" and "diagonal" states. When the robots came closer together, especially when four robots were operating in the workspace, the diagonal waypoints which were achieved at a local minima were susceptible to deviations.

The robots deviate from in their planned paths at times during the experiments, as highlighted for example in Fig. 4.5. This can be partially attributed to the external forces on the robot due to other robots present in the arena even though they maintain a distance greater than $R_{I_{robot}}$. The original $R_{I_{robot}}$ was determined while the robots were at rest experiencing static friction. Once the robots start moving, the $R_{I_{robot}}$ value increases due to the presence of dynamic friction, that is lower than the static friction, under the robots. Additionally, small differences between the coils due to fabrication limitations also contribute to errors. In the case of path deviations, as highlighted in Fig. 4.5, the feedback control, which runs at 3Hz, is designed to bring the robot back to its desired waypoint. Another potential cause for errors is the assumption that the net magnetization direction is through the center of the robots; a small offset in the net magnetization can affect the position of the robot at the equilibrium. There can also be a significant impact to the image processing based tracking accuracy due to small changes in the workspace which can affect the background subtraction algorithm. Therefore, the tolerance for reaching a goal location is fixed at 0.5 $mm$. It should also be noted that currently the closed loop path

involves only position control of the robot and not orientation control at this time. Nevertheless, this type of multi-robot planning and control will be useful in future micromanipulation applications, such as those that require efficient, sequential, and cyclic assembly of microscale components.

The control of the robot at any given location of the coil was not possible due to limited modeling, since the states were defined only at the two aforementioned equilibrium positions. Each coil is only capable of providing a force inward towards or outward away from the center of the coil but not in a specific direction. This can be solved by advanced modeling of the coils as discussed in Chapter 5.

# 5. MM SCALE SYSTEM POTENTIAL FIELD BASED CONTROL

In this chapter[1], the modeling of the planar array coils is extended to actuate the robot at any discretized location in a single coil. The states and actions are expanded to provide a smooth motion in the whole workspace. A single coil is discretized into $5 \times 5$ states, and actions in 8 directions are considered at each state. However, not all states have sufficient action capability to actuate the robots due to the geometry of the coil and the minimum actuation force requirements. Therefore, traditional path planning techniques cannot be used. Instead, a path planner that considers the specific action capability of the grids in the workspace is used to navigate the robot through the workspace. Also, the knowledge of forces that are associated with these actions enables the use of interaction force models between two robots to study the effect of other robots in the workspace when planning and executing the motion of a particular robot. For this method, the $11 \times 11$ array of coils of platform 2 and a N42 magnetized neodymium disc magnet of diameter 3.175 $mm$ and 0.79 $mm$ thickness is chosen.

## 5.1 Potential Field Based Modeling

### 5.1.1 Magnetic Forces

The forces in the coil can be evaluated by breaking down the coil into separate current carrying wire segments in the X and Y axes. For example, the magnetic flux $\mathbf{B} = [B_x, B_y, B_z]$ at a point $P(x, y, z)$, generated by a wire segment along the Y axis

[1]The research presented in this chapter has appeared in [92] and is partially reproduced here. [92] B. V. Johnson and D. J. Cappelleri. "Modeling, control and planning for multiple mobile microrobots". In *Proceedings of the ASME 2019 International Design Engineering Technical Conferences & Computers and Information in Engineering Conference*, Anaheim, California, USA, August 18-21 2019. 

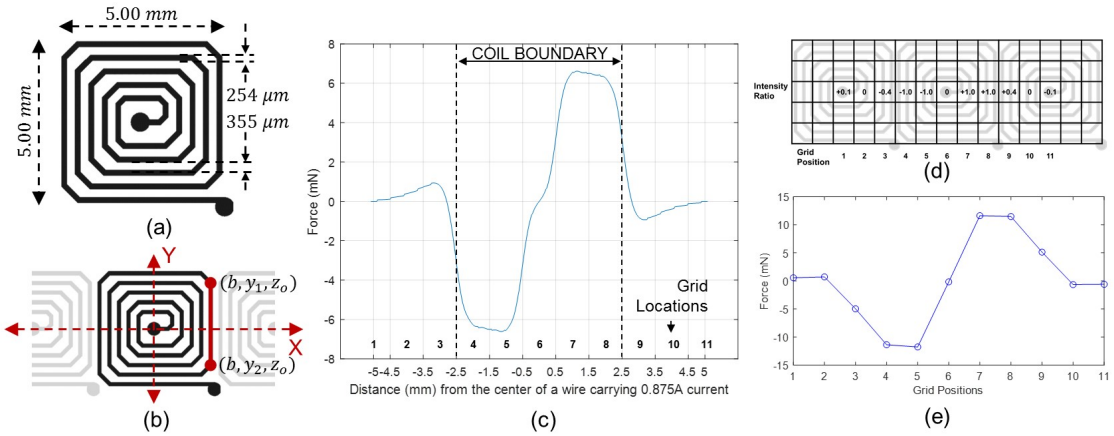


Figure 5.1. : (a) Schematic of a single coil with dimensions. (b) Schematic of coil arrangement for force measurement. (c) Measurement of forces in the X axis, due to a series of coils along the Y axis. (d) Grid locations and ratio of force intensity with respect to maximum force. (e) Combined force along the various grid locations along the X axis.

carrying current $I_c$ shown in Fig. 5.1(b) can be calculated from Eq. 2.2, Eq. 2.3 and Eq. 2.4 where the parameters $y_1$, $y_2$, and $b$ are defined in Fig. 5.1(b). Here, the net flux along the Y axis is zero. The net flux of the coil can be computed by superimposing the flux due to multiple wire segments in the workspace. Similarly, the forces from each wire segment can be superimposed to compute the net force generated by the coil. These equations can be transformed to the X axis to find the magnetic fields due to current carrying wires along the X axis. For simplicity, it is assumed that the forces generated in the X axis are the same as those in the Y axis.

The force along the X axis for a series of wires along the Y axis due to a single coil carrying current in the counter-clockwise direction is shown in Fig. 5.1(c). The net force of a single coil can be evaluated by adding the forces due to the separate segments of wires in the X and Y axes.

The range of non-zero force extends past the actual boundary of the coil. This force is in a direction opposite to that of the segments of wire inside the boundary.

The change of signs of the forces on either side of the center results in the 'center' equilibrium in Chapter 4. The net force is zero at the center of the coil due to the symmetrical geometry of the wire carrying conductors on either side of the center carrying currents in opposite directions. There is also a net zero force outside the range of the coil. The range of a coil is determined to be two coil lengths. Therefore, the forces generated by a single coil can affect robots in the boundary of the coil itself and all 8 surrounding coils.

The workspace is divided into grids to compute forces at various locations as shown in Fig. 5.1(d). A single coil is divided into a $5 \times 5$ array of grid points, evenly distributed in the 4.33 $mm$ coil. To compute the force generating capability of the coil, the eight directions for the forces that include the cardinal and intercardinal directions in the plane are considered. To study the net force on a robot, the geometry of the robot is also considered and the forces are summed over the geometry of the robot. The net force on the robot is then computed at the grid locations. The ratio of the force with respect to the absolute maximum force possible is shown in Fig. 5.1(e). The maximum force was computed to be 11.63 $mN$. However, there is a small discrepancy at the grid locations just outside the boundary of the robot (locations 2 and 10, respectively). These locations were experimentally observed as dead zones due to the friction and drag forces in the workspace. Therefore, it is assumed that these grid locations exhibit zero force on the robot.

### 5.1.2 Coil Combinations

Since the range of a coil extends to the center of adjacent coils, eight coils are used to identify the force capability of the coil at a particular grid location in the workspace. For the purpose of simplicity, the coil power is fixed at either 'on-clockwise', 'on-anticlockwise', or 'off' modes. A set of nine such coils results in $3^9$ possible combinations. Studying the various combinations of coils, the maximum force that can be generated along the eight directions are discovered. These new combinations of coils

provide new possible actions or action sets for the robot to move in the workspace. The minimum force required to move the robot is the force required to overcome the friction and drag forces. Hence, some regions of the coil have limited actions that are possible. These are shown in Fig. 5.2(a). In the previous work in Chapter 4, only motions to the 'center' and 'diagonal' positions were possible. The new actions identified here improve the motion capabilities of the system and reduce the number of coils required to actuate the robot compared to the earlier method. An example of such coil combinations for the grid position at the center of a coil is shown in Fig. 5.2(b). Here, to actuate the robot, the coil underneath the robot is not actuated. The coils surrounding the robot are used to generate sufficient force to move the robot in any desired direction. It should also be noted that by actuating only a single coil, not enough force is generated to overcome the friction and drag forces in the workspace.

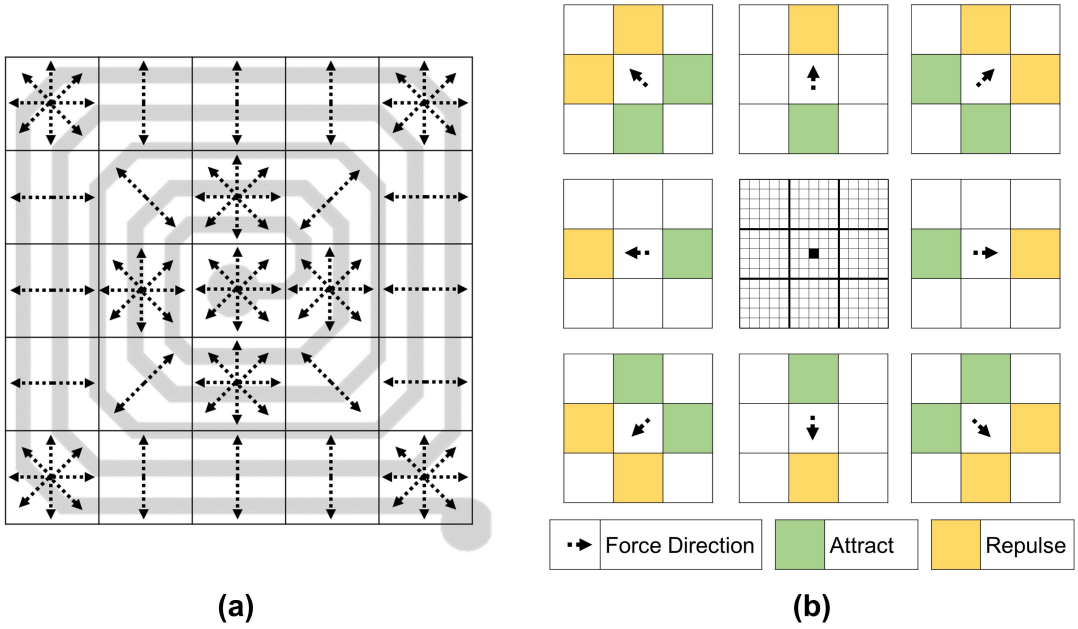


Figure 5.2. : (a) Possible actions at different states in a single coil. (b) Coil combinations of a $3 \times 3$ array of coils for generating various directions of forces along cardinal and intercardinal directions for the current state at the center of a coil. The polarity of the coil is shown in green (attract) and yellow (repulse).

## 5.2 Path Planning using Potential Fields

In view of the uncertainties in the system, the planning problem can be formulated as a Markov Decision Process (MDP) that formulates the shortest path problem in a stochastic environment. A MDP utilizes information of the robot's *(agent)* position *(state)*, *actions* that can be taken that affect the dynamics of the robot, and known rewards for transitions between these states. The solution describes the probability of transition to a state $s'$ when an action $a$ is taken, that gives a reward $r$. On writing different states and observing rewards, an optimal sequence of actions can be generated. However, due to uncertainties in the system, applying the policy might be different from the final states. The markov property is defined as the probability of reaching a future state that depends only upon the present state, and not the preceding states. MDPs are controlled stochastic processes satisfying the Markov property and assigning reward values to state transitions [93]. They are described by the 5-tuple $(S, A, T, p, r)$.

- $S \rightarrow$ State space
- $A \rightarrow$ Set of all possible actions
- $T \rightarrow$ Set of time steps for decision to be made
- $p \rightarrow$ State transition probability function
- $r \rightarrow$ Reward function definition on state transitions

The transition probability $p$ characterizes the dynamics of the system. $p(s'|s, a)$ represents the probability of the system to transition to state $s'$ from $s$ by the action $a$. This $p$ function $\forall s, s'$ is represented as $P_a$ which is a matrix of size $S \times S \times A$. Here the sum of all probabilities $\Sigma_s p(s'|s, a) = 1$. The $p()$ probability distributions over the next state $s'$ follow the fundamental property which describes them as a MDP. If $h_t$ represents the history of states and actions until time step $t$, for a MDP it is true that

$$\forall h_t, a_t, s_{t+1}, P(s_{t+1}|h_t, a_t) = P(s_{t+1}|a_{t+1}) = p(s_{t+1}|s, a) \tag{5.1}$$

As a result of the action $a$ in state $s$ at time $t$, the agent receives a reward $r_t = r(s, a)$. Here, the positive value of $r_t$ is considered as gains and negative value as costs. For this study, it is assumed that the state transition and reward functions are *stationary*, hence they do not change from one time step to another.

### 5.2.1 Discrete State Space

The planar workspace is divided into a grid of points based on the modeling of forces described earlier. Each coil consist of a $5 \times 5$ grid. Therefore, the microcoil platform with an $11 \times 11$ array of coils has a total number of states $S = 3025$. The location of a robot in the workspace is approximated as the nearest grid point to this location. The threshold for reaching a goal is half the length of the grid spacing, which is $\approx 0.43\ mm$. The obstacles in the workspace are identified by image processing techniques. The states corresponding to these obstacles are marked as obstacle states. Note: The robots located at the edges or corners of the coil array are not considered in the current formulation. These locations can simply be treated as obstacles in the planning algorithm so the robot will avoid them.

### 5.2.2 State Transitions

The transition probability matrix $P_a$ of size $S \times S \times A$ denotes the probability to move from one state to another due to a specific action $a \in A$. There are a total of nine possible actions, which includes the forces to move in the cardinal and intercardinal directions, plus the action to stay at a particular location. For the deterministic case, the probability of moving in a particular direction due to the corresponding coil combination will be 1. If motion in a particular direction cannot be achieved due to the robot position on the grid, the probability of staying at this position due to that action will be 1. However, in the presence of other robots in the workspace, the net force due to each action as well as the influence forces of the other robots is computed. If the influence of the robot changes the orientation of the net force,

the probabilities are distributed in the decomposed force into the nearest two action directions. If the net force is lower than the threshold force, the probability of staying in the same location is 1. If the robot is too close to the other robot, even the 'stay' action will force the robot to move to another state in the workspace.

### 5.2.3 Reward Matrix

The reward matrix $R$ of size $S \times A$ is the immediate reward of reaching state $s$. The reward for reaching any state other than goal is set as $-1$, while the obstacles are set as $-100$. The reward for the goal is set as 100 to ensure that the actions will eventually lead to the goal.

### 5.2.4 Dynamic Programming Solution

To solve the MDP, the task is to solve for a policy that optimizes the rewards. Although there are many criteria in literature [93] that can be used to evaluate the policy, the ($\gamma-$)discounted criterion, which is one of the most commonly used infinite horizon criterion is used here. The finite, discounted, total reward, and average criteria defines a *value function*, $V_f$, for a given policy $\pi$. The value function for the discounted criteria, for a given policy $\pi$ assuming $0 \leq \gamma < 1$, is given by

$$V(s) = \sum_{s'} P_{\pi(s)}(s, s')(R_{\pi(s)}(s, s') + \gamma V(s')) \tag{5.2}$$

With this method, it is possible to establish the *Bellman optimality principle* [94]. A dynamic programming approach to solve MDPs efficiently is used here. To solve this MDP, the *MDPtoolbox* toolbox for MATLAB [95] is used. A value iteration method is used to solve the Bellman's equation iteratively:

$$\pi(s) := argmax_a\{\sum_{s'} P_{\pi(s)}(s, s')(R_{\pi(s)}(s, s') + \gamma V(s'))\} \tag{5.3}$$

where $P$ is the transition matrix and $R$ is the reward matrix.

## 5.3 Experimental Validation and Tests

In this section, the theoretical results are validated experimentally. First, an overview of the experimental setup is presented. The model of the coil and the new actions are tested. Then, the MDP based planning algorithm is used to find a policy to move the robot to a goal location in the presence of obstacles in the workspace. A second robot is then introduced into the workspace to see its effect on the motion of the first robot. A new policy is then computed and used to successfully move the robot to its goal location while considering the presence of the second robot in the workspace, using the force models developed earlier.

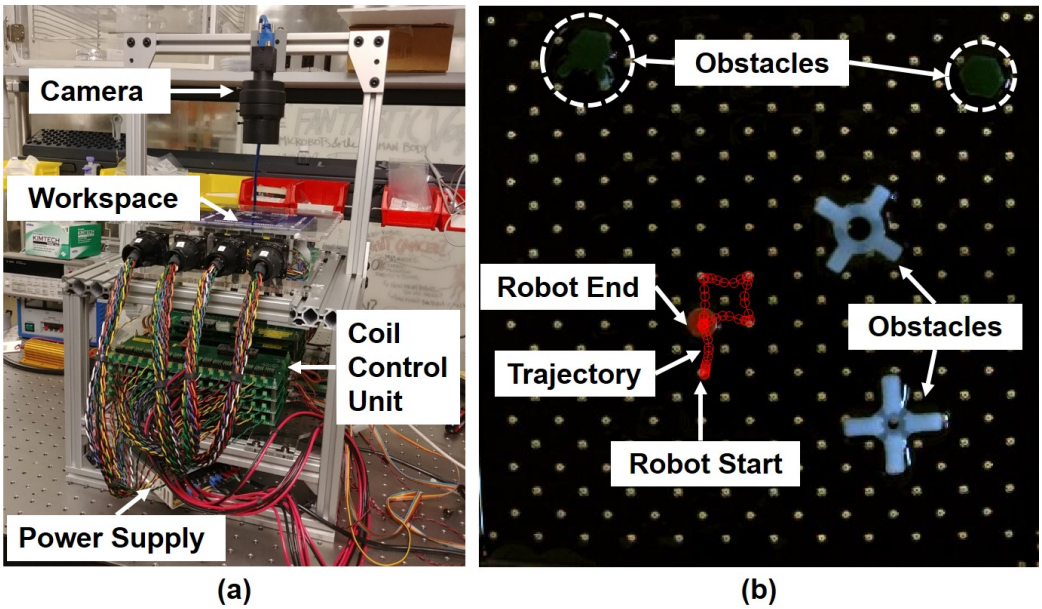


Figure 5.3. : (a) Experimental setup: The workspace which includes the coil array on a PCB and a glass coverslip with a layer of silicone oil. A camera captures images for feedback control and the coil control units supply currents to each individual coil. (b) Single robot motion test that depicts the path of the robot that goes to 'center' waypoints without using the 'diagonal' waypoints.

### 5.3.1 Experimental Setup

The experimental setup is shown in Fig. 5.3(a) which consists of the $11 \times 11$ array coil workspace provided with currents through the power connector cables. The current in each coil can be controlled with eight custom control units described in Chapter 3. A set of 16 coils are controlled using a single GPIO and PWM driver board, to which communications are sent over an $I^2C$ interface through an arduino. It is connected to a CPU with an Intel®Core™i7-4771 (3.50 GHz) processor and 16 GB RAM. All computations are performed using MATLAB and the commands are sent to the controller boards through the Arduino microcontroller interface.

The robots were tracked using color segmentation and localization using the MATLAB image processing toolbox. An overhead camera (PointGrey FL3-U3-13E4C-C, Point Grey Research Inc.) is used to capture images of the workspace at 3 $Hz$, which provides sufficient time for the robot to reach the next state. The control program analyzes the captured image and instructs the microcontroller using the COM ports to activate the required coils in the workspace.

### 5.3.2 Single robot motion tests

First, the new motion capabilities of the microcoil platform are presented. A single robot is given way-points that are in the shape of the letter 'P', as shown in Fig. 5.3(b). The robot moves smoothly along the workspace without have to alternate between the 'center' and 'diagonal' waypoints in the workspace, as was done in the previous work. A PID controller is used to keep the robot on the path; the path of the robot is highlighted in the figure. However, it is noted that the robot tends to stray from its intended straight path due to the inability of the coils to produce force along certain directions at some grid locations of a coil. This absence of multi-directional force capability at all locations in the workspace motivates the need for a path planner to help plan the actions at various locations in the workspace.

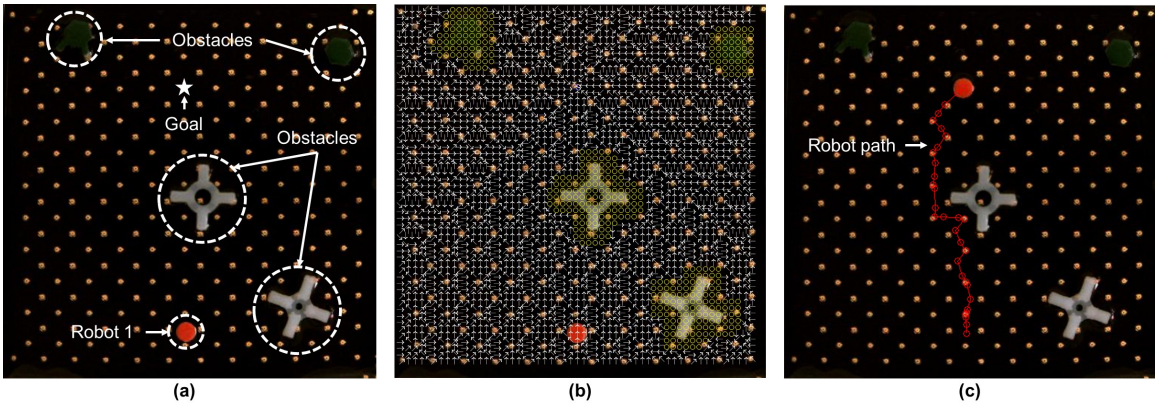


Figure 5.4. : Single robot motion tests with path planning: Robot 1 has to reach the goal location in the presence of obstacles in the workspace. (a) Overview of the workspace. (b) Computed policy to reach the goal location for any given state in the workspace. Arrows denote the action to be taken by the robot at each state in the workspace. Circles denote obstacles and unachievable states due to geometric constraints. (c) Experimental result of Robot 1 using the policy to move to the goal location.

Next, a case considering the path planning algorithm discussed in the path planning section is tested. The task is for Robot 1 to move to a goal location using any of the eight actions, considering the obstacles in the workspace as shown in Fig. 5.4(a). The shape of the obstacles are identified. An additional gap which equals the size of the robot is also considered as an obstacle to allow the robot to move close to the obstacles if necessary. The computer took $\approx$ 9 seconds to find the $P$ matrix, and $\approx$ 96 seconds to solve the MDP. The policy that describes a specific action for every state generated by solving the MDP, is shown in Fig. 5.4(b), where the arrows denote the action to be taken at that state. The motion is generated using a bang-bang controller based on the actions corresponding to the current location of the robot. The successful motion of Robot 1 using the policy to move to the goal location is shown in Fig. 5.4(c). The coil currents are scaled to ensure uniform force generation in the workspace. The maximum current used is 0.6 $A$.

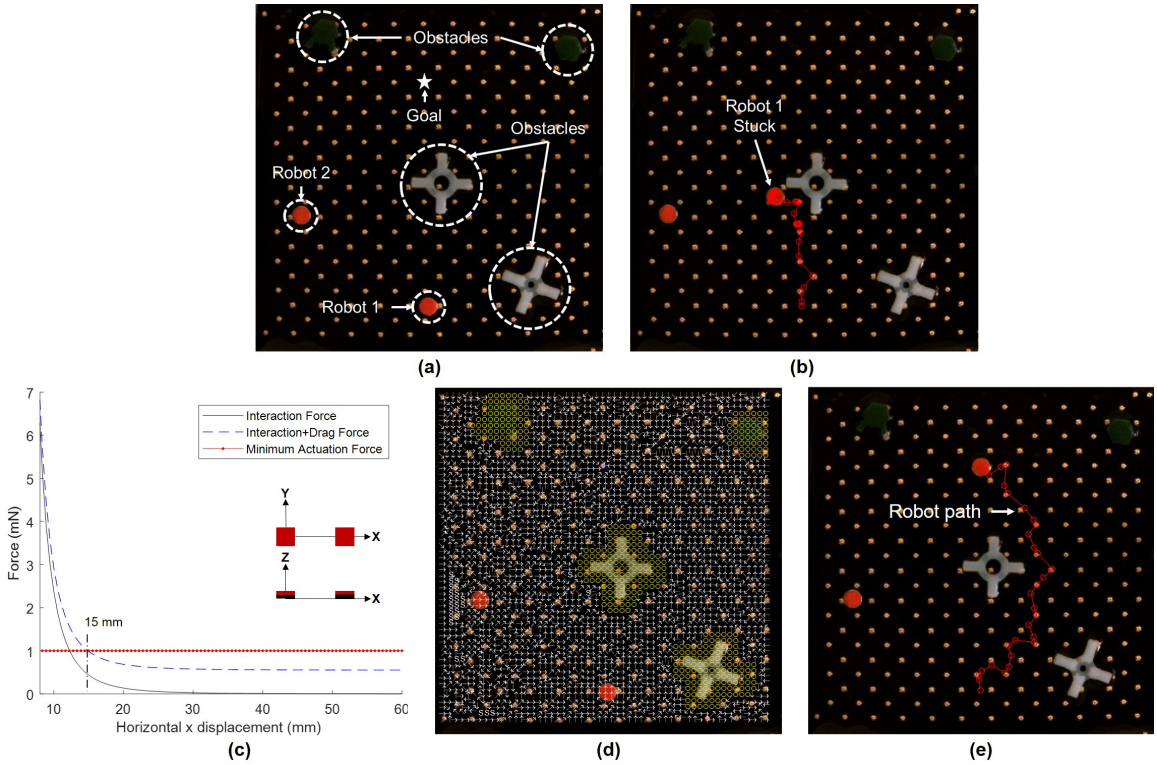


Figure 5.5. : Multi-robot path planning tests: Robot 1 has to reach the goal location in the presence of obstacles in the workspace. (a) Overview of the workspace. (b) Experimental results of Robot 1 trying to use the policy to reach the goal location in the presence of Robot 2 by only treating it as a physical obstacle. The robot gets stuck in the middle of its path. (c) Interaction forces between two square shaped 3.175 $mm$ magnets, drag force and actuation forces in the workspace. (d) New policy considering the effect of Robot 2 as another magnetic robot in the workspace. Arrows denote the action to be taken by the robot at each state in the workspace. Circles denote obstacles and unachievable states due to geometric constraints. (e) Experimental result of Robot 1 path using the new policy to reach the goal location.

### 5.3.3 Multi-robot path planning test

A case when a second robot is present in the workspace is studied next, as shown in Fig. 5.5(a). Here, using the same policy derived in the single robot case results

in the robot Robot 1 getting stuck at a location on the way to the goal as shown in Fig. 5.5(b). This is due to the interaction force between the two magnetic robots in the workspace that impacts the motion of the robots. The interaction forces between the magnets are modeled using the finite element model given in [96]. The comparison of the interaction force, with respect to the minimum actuation force is shown in Fig. 5.5(c).

The minimum force required to actuate a single magnetic robot is approximately 1 $mN$. Therefore, this force needs to be greater than the magnetic interaction force opposing it when another magnetic robot is in the workspace, as well as the drag force due to the fluid. As shown in the plot, this happens at a spacing distance of $\approx$ 15 $mm$. Thus, this is the closest spacing possible for two magnetic robots in the workspace. Note: the maximum actuation force possible is $\approx$ 12 $mN$.

A new policy is generated considering the position of the second robot $R_2$ in the workspace. This is shown in Fig. 5.5(d). The P matrix is modified to change the probability based on the net force due to the interaction and actuation forces. The computer took $\approx$ 11 seconds to find the $P$ matrix and $\approx$ 110 seconds to solve the MDP. Here, the new policy guides the robot to another path where it reaches the goal. This is illustrated experimentally in Fig. 5.5(e). Videos of the experimental results can be viewed at the following link:
`https://youtu.be/B6AM6asdBgE`.

## 5.4 Discussion and Conclusion

The new modeling approach expanded the capabilities of the platform to actuate the robot in eight directions compared to Chapter 4 which allowed only four actuation directions. The coils were also modeled to study the actuation forces generated at any location in the coil. However, the geometry of the coil limits the force capability of the robot at some areas in the coil. This is overcome with a MDP based path planner which can generate a policy for movement to a specific goal location. The

MDP formulation is also expanded to work when other robots are present in the workspace. The formulation considers the interaction force between the robots and changes the policy to reach the goal location.

However, the experiments presented consider only a stationary second robot in the workspace. In future, this formulation can be expanded to include the trajectory of other moving robots in the workspace. Also, the computation of the policy takes $\approx 100$ seconds to complete which makes it hard to implement in real time applications. This could be solved by using a faster algorithm or by constraining the states to solve the existing problem faster. However, the presence of other magnetic elements in the workspace of microrobotic platforms will require careful consideration of interaction forces. This approach presented here is a viable option for doing this.

The main limitation of the mm-scale coil array is its size. Robots smaller than 2 $mm$ cannot be controlled precisely due its low resolution in field control. In order to actuate smaller robots, the resolution of the magnetic field generated should be improved. However, in order to reduce the size of the coils further, the spiral geometry of the mm-scale robots have to be changed to small strips of wire that can generate sufficient forces in the workspace. Such a design is discussed in the next chapter.

# 6. MICRO SCALE LOCAL MAGNETIC FIELD GENERATING SYSTEM

The mm-scale coils in Chapter 4 mimic the multi-turn coils or electromagnets in the workspace. The large number of turns offers larger fields strengths and their unique geometry produces local equilibrium locations for the robots. However, the size of robot is restricted to $\geq 2mm$, and the actuation of the robot is possible only through the discrete waypoints in the workspace. To generate local magnetic fields for smaller robots (order of $1mm \times 1mm$), the spiral structures of the mm-scale coils were replaced by the $\mu$scale v1 platform [89]. In this platform, smaller strips of wire laid parallel to each other as shown in Table. 6.1. The preliminary study for the feasibility of these microcoils were conducted on this platform. Based on these results, a two layer microcoil system was designed and characterized. The details on each of these systems are described in this chapter[1].

## 6.1 Single Layer Microcoil System Design

The coil is reduced to a simple strip of wire in the workspace and is connected to a switchable and current controlled controller board. Each microcoil is 600 $\mu m$ long and 250 $\mu m$ wide. Each microcoil is much smaller than the mm-scale multi-turn coil and hence significantly increases the field resolution. Due to the smaller size of the coil, the workspace size is limited to 9 $mm \times 4.2$ $mm$. The microcoil array is located only on the top layer, and the traces are inbuilt in the multi-layered PCB to run the microcoils to the power input [89, 98]. Each microcoil can be activated independently, where both the direction and magnitude of current can be controlled through the system discussed in Chapter 3.

[1]The research presented in this chapter has appeared in [97] and is partially reproduced here.
[97] B. V. Johnson, S. Chowdhury and D. J. Cappelleri, "Local Magnetic Field Design and Characterization for Independent Closed-Loop Control of Multiple Mobile Microrobots," in *IEEE/ASME Transactions on Mechatronics*, vol. 25, no. 2, pp. 526-534, April 2020. 

Table 6.1. : $\mu$ Scale Magnetic Field Generating System v1

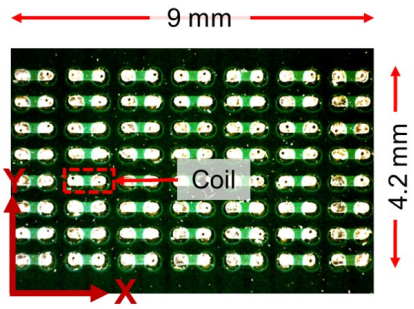


| | |
|---|---|
| References | [98] |
| Coil Type | Straight wire |
| Number of coil layers | 1 |
| Number of coils | 64 ($8 \times 8$) |
| Coil Dimensions | 0.60 $mm \times 0.25$ $mm$ |
| Coil Spacing | 0.60 $mm$ |
| Workspace Dimensions | 9 $mm \times 4.2$ $mm$ |
| Movement Type | Continuous |
| Robot Footprint | $\geq$ 1 mm $\times$ 1 mm |
| Direction Control | One (Y direction only) |

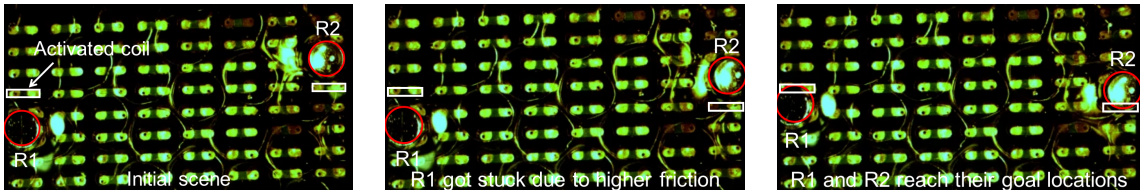


(a) (b) (c)

Figure 6.1. : Independent actuation of two robots: (a) Start locations of the robots $R1$ and $R2$ (Robots are marked with red circles and activated coils are marked with white boarder). (b)$R1$ is stuck and $R2$ reaches the waypoint on the target microcoil. New waypoint is set by activating the next microcoil and tuning off the previous coil. (c) Both $R1$ and $R2$ reach their respective goal locations[2].

The open-loop independent actuation of two robots was demonstrated using this system. Two robots $R1$ are $R2$, are transported to their respective goal locations in opposite directions. Fig. 6.1a shows the initial positions of the robots. Each robot is made of a circular neodymium magnet of 1 mm diameter, N50 magnetization (marked in red circle). The coils were successful in actuating the robots in the Y axis at the ends of the workspace as shown in Fig. 6.1c.

These microcoils can apply gradients to move the robots along the Y-axis, as illustrated in Fig. 6.1. However, the gradient (and hence forces) along the X-axis due to these coils is negligible. Also, the effect of current in the lower trace layers were significant and caused robots to move when the neighboring coils were not activated. Thus a two layer $\mu$-scale microcoil platform (v2) was developed after observing these limitations of driving the robot in the workspace. It was identified that specific coils were needed to be oriented in two axes in the plane to drive the robot through complex trajectories. The traces also needed to be carefully designed to not interfere with the forces generated in the workspace.

[2]Reprinted by permission from Springer Nature Customer Service Centre GmbH: Springer Nature Springer Journal of Micro-Bio Robotics [98] Chowdhury et al. "Designing local magnetic fields and path planning for independent actuation of multiple mobile microrobots". *J Micro-Bio Robot* ©2017

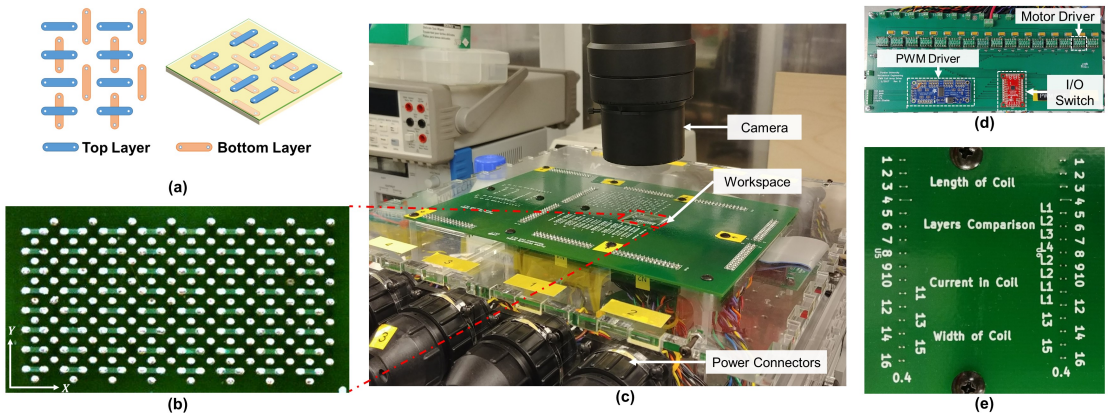


Figure 6.2. : (a) Schematic showing how the two sets of coils are arranged in the workspace. (b) Workspace view through the camera (c) Overview of the hardware platform for microrobot actuation. (d) Current control board. The I/O switch and PWM drivers control the magnitude and direction of current that runs through the motor driver. (e) Characterization arena section with different geometrical and microcoil properties.

## 6.2 Two Layer Microcoil Design

The coil layout is now modified to include coils in two layers that can independently control magnetic field and gradients along both the axes locally, as shown in Fig. 6.2(a). Due to doubling of number of coils in the workspace, the workspace contains 128 microcoils. The trace layers are designed to be isolated from the top two coil layers so that they will not influence the robots in the workspace. To also track the position of the coils, a coordinate system is also displayed on the silkscreen for the ease of tracking the coil number.

To generate sufficient force in both axes, microcoils along orthogonal axes were included in the design of the coil platform. In order to accommodate the additional vias needed for this, the spacing between the coils was increased to 0.86 $mm$. The new set of microcoils has been laid out in a staggered, but parallel fashion to keep the spacing between the microcoils equal as shown in Table 6.2 and Fig. 6.2(a). This

Table 6.2. : Microscale Magnetic Field Generating System

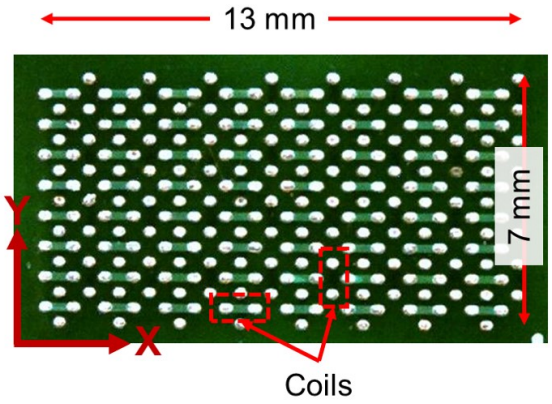


| | |
|---|---|
| References | [97] |
| Coil Type | Straight wire |
| Number of coil layers | 2 |
| Number of coils | 128 $(8 \times 8)$in each coil layer |
| Coil Dimensions | 0.86 $mm \times 0.25$ $mm$ |
| Coil Spacing | 0.86 $mm$ |
| Workspace Dimensions | 13 $mm \times 7$ $mm$ |
| Movement Type | Continuous |
| Robot Footprint | $\geq$ 1 mm $\times$ 1 mm |
| Direction Control | X and Y |

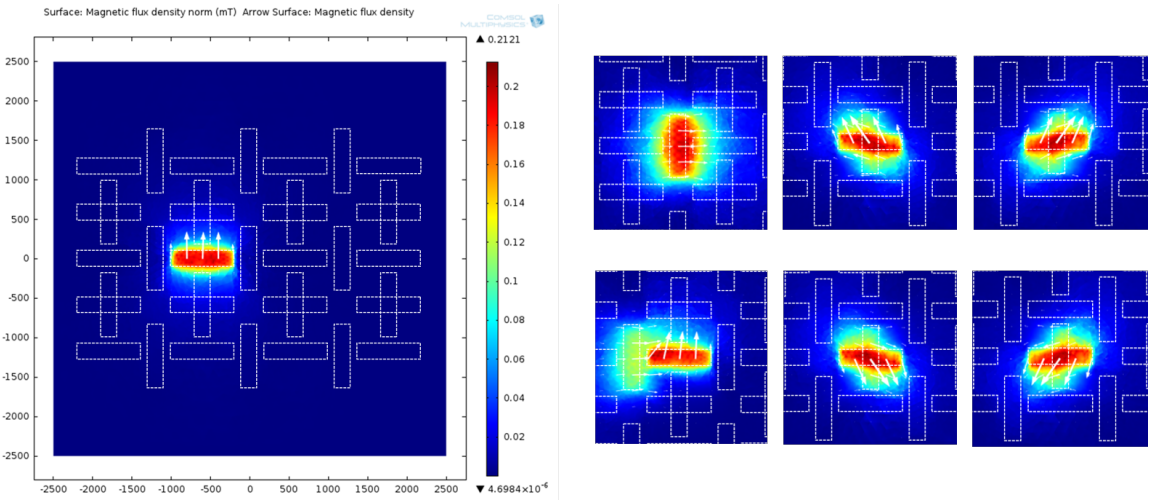


Figure 6.3. : Simulation results from COMSOL analyzing fields in the workspace[3].

involves 128 microcoils in two orthogonal 8×8 arrays with each microcoil individually connected to a power source. These microcoils can individually provide forces in the X and Y directions and also in intermediate directions by the superposition of currents in multiple microcoils simultaneously. The increase in spacing increases the minimum size of the robot that can be controlled. However, it is sufficient to actuate a robot $\geq 1\ mm \times 1\ mm$ footprint. The constraint is that it may require activating up to four microcoils (a maximum of two each in X and Y axes) at a time to move the robot in all directions.

## 6.3 Modeling

An analysis of the new design shows significant magnetic field and gradient along both the axes which will yield a more complete control of robots in the workspace. Fig. 6.3 shows simulation results for this new coil design. The arrows indicate the direction of field gradient and thus the predicted motion for the microrobot. The arrows indicate the direction of field gradient and thus the predicted motion for the

[3]Reprinted by permission from Springer Nature Customer Service Centre GmbH: Springer Nature Springer Journal of Micro-Bio Robotics [98] Chowdhury et al. "Designing local magnetic fields and path planning for independent actuation of multiple mobile microrobots". *J Micro-Bio Robot* ©2017

microrobot. For a coil carrying current aligned along the X axis, the field gradients are along the Y axis. Similarly, for a coil carrying current aligned along the Y axis, the field gradients are along the X axis. For two coils carrying current in orthogonal directions, the net field gradient is along a diagonal direction as shown in Fig. 6.3.

This coil design alleviates critical issues from the previous design. However, there are critical areas in the coil schematic which do not have any magnetic field being generated when all its surrounding coils are activated. The magnet used for actuation should be therefore large enough to experience force from any of the surrounding coils.

## 6.4 Experimental Platform

The hardware for independent microrobot control consists of the two layer microcoil platform and the coil current drive electronics. The microcoil platform hosts the PCB, mount, and power connectors that connect to all the coils. The PCB contains the robot workspace and a specially designed characterization arena.

### 6.4.1 Microcoils and traces

Each of the microcoils is 860 $\mu m$ in length and 254 $\mu m$ wide. The PCB has 10 layers in total where the top two layers form the microcoils and the bottom eight layers form the required connections to the control electronics, as shown in Fig. 6.2(c). This layout was designed so that it could be fabricated with standard PCB technology. The top layer of the PCB consists of horizontal (X-direction) microcoils and the second layer (at a depth of 162 $\mu m$) contains the vertical (Y-direction) microcoils. The thickness of the top layer microcoils are 35 $\mu m$ and the second layer microcoils are 14 $\mu m$ thick. All traces are 76 $\mu m$ wide and 14 $\mu m$ thick. All the traces have a separation distance of 452 $\mu m$ below the second microcoil layer to minimize their effect in the magnetic field generated in the workspace. The connectors linking these systems are placed away from the workspace to also limit any interference in the magnetic field being generated.

### 6.4.2 Microcoil Control Substrate

The microcoil platform consists of the PCB with the microcoils mounted on an acrylic box with four power connectors on two sides of the box. The PCB contains a 13 $mm \times 7$ $mm$ workspace (Fig. 6.2(b)), which is clamped to the top surface of the box to ensure that the workspace is flat. The microcoils in the workspace have vias and traces that lead to a set of jumper pins in the PCB. Straight connectors are used to connect the coils to circular power connector pins, which are then accessible to the coil current driver circuits. A section of the PCB has microcoils with varying parameters that are used for microcoil characterization tests. A camera is mounted above the workspace to observe the robots moving in the workspace, as shown in (Fig. 6.2(c)).

### 6.4.3 Characterization Arena

A characterization arena (Fig. 6.2(e)) was designed to validate simulations and evaluate various parameters of the system. It was designed with microcoils with varying properties, such as microcoil board layer, length, and width. Additionally, some microcoils were designated to evaluate current limits in the hardware. All the traces for the arena are in the lowest layer of the PCB and have very low resistances. Thus, an additional high power resistor of 5.50 $\Omega$ was used to protect the circuit from high currents. A power supply was directly used to supply the current and identify the effect of the currents applied to the microcoil. Table 6.3 lists the microcoil variations in the characterization arena and what type of tests they are used for.

### 6.4.4 Test Preparation

The microcoil workspace or characterization arena is first cleaned with isopropanol solution to remove dust and other residue. Next, a 25 $mm \times 25$ $mm$ No.1 cover glass (VWR VistaVision 16004-328) is placed on top of the workspace. About 200 $\mu L$ of

Table 6.3. : Characterization Parameters

| Microcoil Index | Length ($\mu m$) | Board Layer | Width ($\mu m$) | Characterization Test |
|---|---|---|---|---|
| 1 | 800 | 1 | 254 | Length |
| 2 | 1000 | 1 | 254 | Length |
| 3 | 1200 | 1 | 254 | Length |
| 4 | 2000 | 1 | 254 | Length |
| 5 | 1000 | 1 | 254 | Layer |
| 6 | 1000 | 2 | 254 | Layer |
| 7 | 1000 | 3 | 254 | Layer |
| 8 | 1000 | 4 | 254 | Layer |
| 9 | 1000 | 2 | 254 | Current/Range |
| 10 | 1000 | 2 | 254 | Current/Range |
| 11 | 1000 | 1 | 254 | Current/Range |
| 12 | 1000 | 1 | 254 | Current/Range |
| 13 | 800 | 1 | 76 | Width |
| 14 | 800 | 1 | 127 | Width |
| 15 | 800 | 1 | 178 | Width |
| 16 | 800 | 1 | 254 | Width |

Table 6.4. : Microcoil range characterization for different robot types

| Robot ID # | Shape | Grade | Dimensions | NAR | | GR |
|---|---|---|---|---|---|---|
| | | | | L1 ($\mu m$) | L2 ($\mu m$) | ($\mu m$) |
| R1 | Disc | N52 | $\phi$ 1.5 $mm$, 0.5 $mm$ thick | 1342 | 1483 | 1327 |
| R2 | Disc | N50 | $\phi$ 1.0 $mm$,0.5 $mm$ thick | 635 | 588 | 641 |
| R3 | Disc | N52 | $\phi$ 1.0 $mm$,0.5 $mm$ thick | 727 | 976 | 862 |
| R4 | Cube | N52 | $0.5 \times 0.5 \times 0.5$ $mm^3$ | 706 | 741 | 431 |

NAR: Net Actuation Range, $\phi$: Diameter,

L1: Layer 1, L2: Layer 2, GR: Geometric Range

silicone oil (A12728, Alfa Aesar) is deposited on the slide and spread out. This forms a uniform layer on the cover slide. The workspace microcoils can be seen through the transparent cover slip. Additionally, the absence of walls in the workspace eliminates wall effect forces in the workspace.

## 6.5 Characterization Tests

The characterization tests for the local magnetic field generating system are presented in the following section. The microcoils ability to actuate various types of magnetic robots is studied along with the microcoils current carrying capabilities. The impact of having multiple magnetic robots in the workspace and how this affects their motion is also analyzed. Finally, the motion of the robot at different locations in the workspace is examined when controlling it with either a single microcoil or multiple microcoils.

### 6.5.1 Robot Types

For testing, the four magnets shown in Table 6.4 are used. These magnets are neodymium with nickel coating and are commercially available (*SuperMagnetMan*).

These robots are oriented in the workspace with their north pole facing up (along the Z axis), which ensures that they can move in the plane, as discussed in Sec. 6.5.5. To keep track of the magnetization direction, the north pole of the robot is colored.

### 6.5.2 Operating Current Limits

The limits for the operating current intensity is dependent on the current control hardware, the PCB current limits, and the impact of the field generated by underlying traces. The current driver can supply $60W$ power at 2.50 $V$ to the microcoils. This is sufficient to power all the microcoils at 0.4 $A$ each. However, due to the varying resistances resulting from the use of multiple layers and microcoil thickness, the maximum attainable current for each microcoil is 0.37 $A$. The minimum current to move a R1 robot at each layer was experimentally determined (Table 6.5). However, the underlying traces can impact the movement of the robot if too much current is applied. Consider the cases where multiple traces overlap at the same point in the workspace. When a group of microcoils are activated, the fields due to these traces that lead to these microcoils can superimpose to generate a field in that location in the workspace. This limits the number of microcoils that can be activated at a time, although the microcoils themselves do not overlap. Therefore, the motion of the robot is restricted to either the X axis or Y axis by just activating either the horizontal microcoils or vertical microcoils at a particular time. This ensures that minimal number of traces overlap to generate unwanted magnetic fields.

### 6.5.3 Microcoil Actuation Range

The actuation range of each microcoil depends on the size and magnetization of the robot. In Sec. 2.3, the magnetic moment was considered as a point source, but in reality, the distribution is more complex. As a better estimate, one can consider the moment to be uniformly distributed on the surface of the robot. This distribution varies with the size of the robot and influences the magnetic force generated on the

Table 6.5. : Microcoil current for R3 type robot actuation

| Layer # | Height from surface ($\mu m$) | Minimum Current ($A$) |
|---|---|---|
| 1 | 146 | 0.04 |
| 2 | 311 | 0.14 |
| 3 | 782 | 0.34 |
| 4 | 923 | 0.58 |

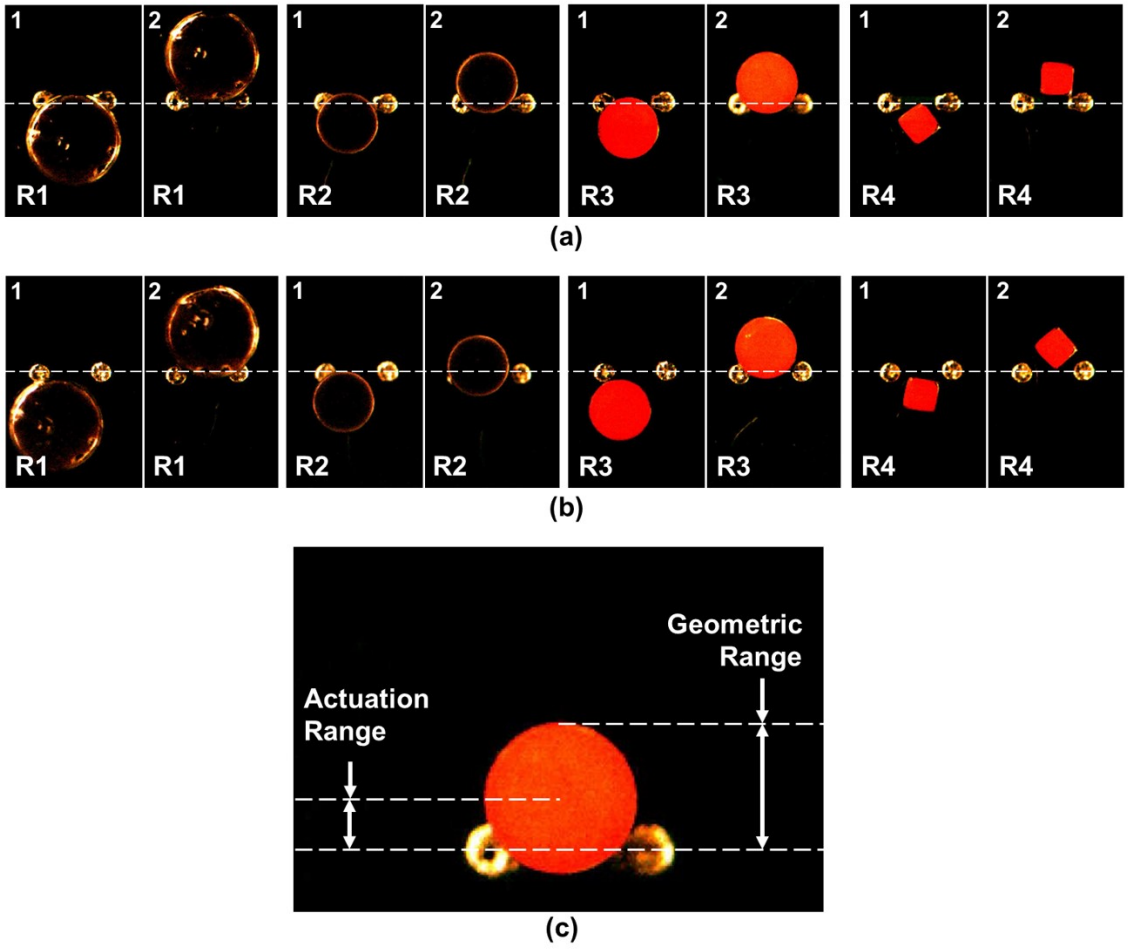


Figure 6.4. : Experiments comparing the range of robots R1, R2, R3, and R4, when current $0.2A$ flows through coils in (a) Layer 1 and (b) Layer 2. (c) Definition of actuation range and geometric range.

robot. The negative force generated at the outer ends of the microcoil limits the activation range of the microcoil on a robot as seen in Fig.2.5. A robot at the center of the microcoil can also be pushed outside its range due to the momentum generated by the large force from the microcoil. However, the same microcoil will not be able to pull the robot back since it will go outside the influence region of the microcoil. Hence, the actuation range of the robot is tested by slowly increasing the current until the robot reaches the end of its travel. The current in the reverse direction is applied to pull the robot back to the other end of the microcoil.

Another factor that affects the actuation range of the microcoil is which layer it resides in. The forces generated by the microcoils in the lower layer are smaller compared to the forces generated by the top microcoils for the same input current. However, the negative force in the workspace will be lower as well for the lower layer microcoils, which improves the range of actuation. This can be seen in Fig. 6.4 and the data in Table 6.4. The lower layer microcoils have a larger net range compared to the top layer among all the robots tested. Furthermore, the robot type R3 with higher magnetization has a larger range compared to that of R2 although both of them are the same size.

For continuous actuation of the robot, it is necessary that the geometry of the robot have sufficient reach to overlap at least one other microcoil in the workspace. Considering the minimum actuation range value of the robot in the workspace, the reach of the robot can be calculated using the geometric range of each robot as seen in Fig. 6.4(c). Geometric range is the sum of the minimum actuation range and half the length of the robot. For successful actuation, the geometric range of the robot should be at least greater than or equal to the spacing between the planar microcoils, which is equal to 860 $\mu m$. The list of geometric ranges for all robot types investigated can be found in Table. 6.4. The robots R1 and R3 have sufficient geometric range for moving in the workspace without any dead zones. However, robots R2 and R4 will not be able to reach the next microcoil (geometric range $<$ 860 $\mu m$) and are thus not considered for further tests.

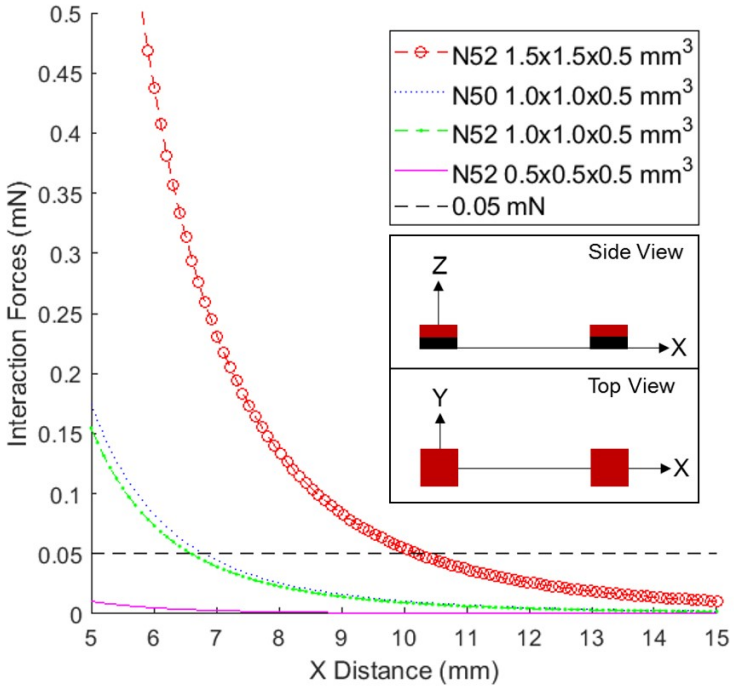


Figure 6.5. : Interaction force between two identical magnets. The static friction force of 0.05 $mN$ is denoted to estimate the minimum separation distance between the robots to withstand their interaction forces.

### 6.5.4 Multiple Robot Interactions

The activated microcoils are able to actuate the robots in their vicinities. However, if multiple hard magnets are used as robots, their mutual interactions have to be considered. For example, two disc magnets on a plane repulse each other when their north poles are aligned in the same direction while they attract each other when their poles are aligned in the opposite directions. To avoid the possibility of the robots sticking together, the robots are placed on the plane with both their north poles along the Z-direction. This also ensures that the microcoils exert the same forces on all the robots in the workspace.

To analyze the forces between the robots, the model given in [96] is used for rectangular magnets in the same plane with their magnetization axis parallel to each

other. The analytical solution gives the forces between two magnets when one magnet is fixed at the origin and the force on the other magnet is measured at different locations from the origin (or separation distances between the robots). The graph in Fig. 6.5 shows the interaction forces between two similar robots of the various types considered for these different distances. The microcoil actuation forces on these robots are around 0.4 $mN$ at the peak and about 0.1 $mN$ at the extents of actuation range. To prevent the interaction forces from affecting the robot motion, the interaction forces must be $< 0.05$ $mN$, which is an approximate static friction force. For robot type R1, this corresponds to a separation distance of about 10.25 $mm$; for robot type R3, this distance is about 6.82 $mm$. Since the workspace size is $7 \times 13$ $mm$, multiple robots of type R1 cannot be in the workspace at the same time without influencing each other. However, two R3 type robots can be actuated independently if they are located at opposite ends of the workspace. Robot type R2 and R4 also have lower interaction forces, but do not have sufficient geometric range for actuation in the workspace.

### 6.5.5 Robot Motion

The magnetic microrobots can move in the X direction with the microcoils aligned with the Y axis and in the Y direction with the help of the microcoils aligned with the X axis, as long as they are in the actuation range of the coil. The robots also experience a driving force when they are between two microcoils if they have sufficient geometric range and magnetization as shown in Fig. 6.6. The geometric range allows for a small overlap of the robot body over the two adjacent microcoils which superimpose their actuation forces on the robot. Sufficient magnetization allows for the robot to require low currents to actuate it. These properties ensure that there are no dead spots in the microcoil array where the robot will get stuck. Only robots of type R1 and R3 are able to move along the microcoils without any dead zones because of their geometry and magnetization.

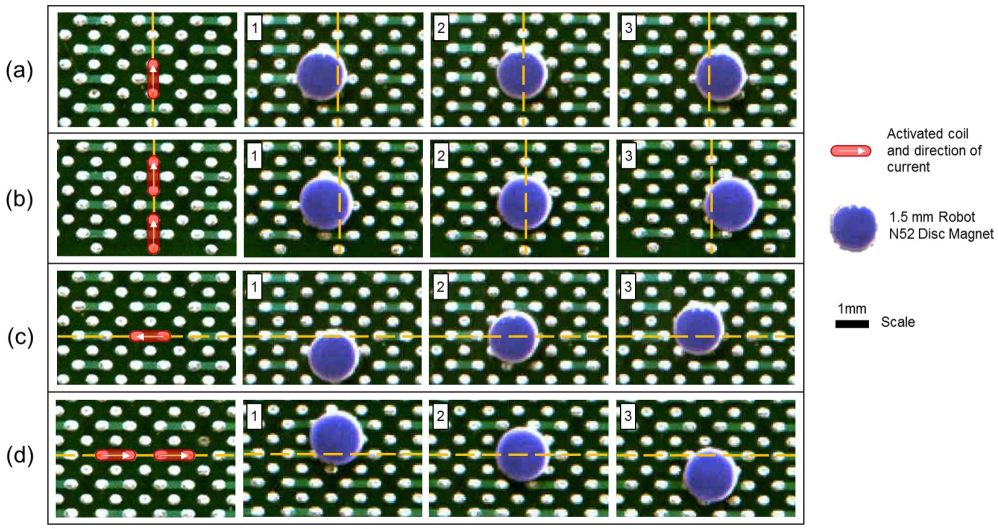


Figure 6.6. : Movement of 1.5 *mm* diameter, 0.5 *mm* thick disc robot (R1) in the workspace due to specified microcoil activation. (a) Movement in X axis due to single microcoil. (b) Movement in X axis due to two microcoils. (c) Movement in Y axis due to single microcoil. (d) Movement in Y axis due to two microcoils.

## 6.6 Actuation and Control

Manual actuation of the robots is time consuming which makes the overall operation slow and not practical for robot teams. To automate the movement of the robot, there are two steps: 1. Compute a path for the robot to move it from an initial state $\mathbf{S_i}$ to a goal state $\mathbf{S_g}$; and 2. Determine the microcoil that needs to be activated as well as magnitude and polarity of the current that the microcoil needs to be provided with. The feedback of the states of the robots are provided by the images from an overhead camera. The images can then be used to determine the states of the robots at any time instant.

Figure 6.7 shows the steps for automating the navigation of the robots. There might be obstacles in the scene that the robots need to avoid during the navigation. Presence of the dynamic obstacles in the scene may complicate the situation since the collision free paths need to be recomputed depending on the change in the environ-

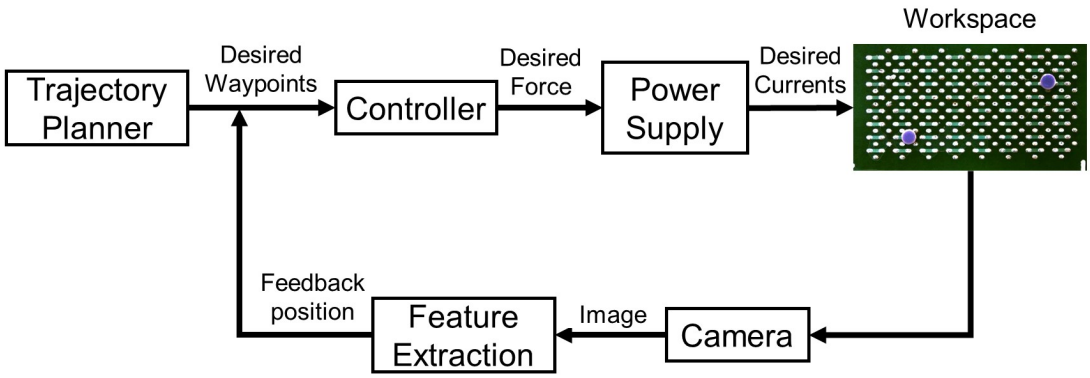


Figure 6.7. : Overall automation approach: The overhead camera takes an image of the workspace with the robots; the information of the states of the robots are extracted from the image; the planner takes the current states of the robots and computes the paths for the robots to respective goal locations, the desired force to move the robot towards the goal locations is computed using a bang-bang controller; and finally the microcoil that needs to be activated as well as its current is determined.

ment due to the moving obstacles. Since multiple robots are actuated independently, the planner needs to be fast enough to compute multiple collision-free paths at the same time. To compute a collision free path for a robot, the other robots in the workspace are considered dynamic obstacles.

### 6.6.1 Feedback Control

As discussed in Sec. 6.5.5, the horizontal microcoils generate force in the Y direction and the vertical microcoils generate forces in the X direction. If the geometric range of the robot is larger than the spacing between the microcoils, the robot will transition from one microcoil to the next. The forces generated, however, are nonlinear due to the nature of the magnetic field.

The microcoils have very low inductance due to the absence of turns, and hence allow for fast switching of currents. The ability to switch currents fast, and the neg-

ligible inertial forces allows for relatively easy control of the robot using a bang-bang controller. The intensity of current for actuation is the minimum current required (Table 6.5) for actuation to prevent the generation of unwanted magnetic fields in other locations in the workspace. This current is also low enough so that negligible heat is generated. The microcoils in the top layer require less current than that of the $2^{nd}$ layer to generate the same amount of force due to their closer proximity to the robots as discussed in Sec. 6.5.2. The magnitude of current flowing through the microcoil is kept constant during actuation, and the polarity is altered to change the direction of force.

To actuate a robot, the position error, the difference between the goal location and the position of the robot, is determined. Only the microcoils that have an actuation range inside the boundary of the robot are considered for actuation. Based on the error in the X or Y direction, the microcoils are actuated with the specified current with the correct polarity to generate forces along the direction of maximum error, as seen in Algorithm 5.

### 6.6.2 Path Planning

A rectangular grid is applied to the workspace. Each grid location represents a distinct state $\mathbf{s}$ for the robot. A discrete action set $\mathbf{a}$ is also defined that the robot can execute to transition from one state to a neighboring state. The action set consists of a finite number of actions that the robot is allowed to take at a given time instant. Each action in an action set will transition the robot to the neighboring states. An A* based graph search based planning algorithm is used to find a collision free path from initial state $\mathbf{s_i}$ to the goal state $\mathbf{s_g}$ of the robot since it is fast. Since the A* planner does not keep track of changes in the map, the path has to be recomputed every time the scene changes due to the presence of dynamic obstacles.

The planner starts by expanding the grid from the state $\mathbf{s_i}$ and stops after it reaches the $\mathbf{s_g}$ based on a cost function $c(\mathbf{s})$. Finally, the planner backtracks from the

**Algorithm 5** CoilActuation(): Determine the microcoils that need to be switched on and the associated polarity of current.

**Input:** Current state of the robot, $\mathbf{s_{curr}}$, desired state, $\mathbf{s_{des}}$, computed by the planner, the microcoil array $C_n$, waypoint threshold, $W_{th}$, magnetization of the robot $\mathbf{M}$, and the search update time, $t_c$.

**Output:** Desired microcoils $c_m \in C_n$ (a set of $m$ number of microcoils) that need to be activated and associated polarities $\{P_i\}_{i=1}^{m}$ .

1: **while** $\| \mathbf{x}_{des} - \mathbf{x}_{curr} \| \geq W_{th}$ **do**
2: Compute the desired magnetic force $\mathbf{F}_d$ based on position error. Find if desired movement is in the X or Y axis.
3: Determine the influence zone based on the current state $\mathbf{s_{curr}}$ of the robot and the required axis of motion
4: Find the $m$ number of microcoils $c_m$ associated to the zone, in the required axis.
5: Setup the polarities $\{P_i\}_{i=1}^{m}$ of the $m$ microcoils based on the required direction of motion in the given axis.
6: Activate microcoil for update time $t_c$.
7: Get feedback of the current state of the robot, $\mathbf{s_{curr}}$.
8: **end while**
9: **return** $c_m \in C_n$ and $\{P_i\}_{i=1}^{m}$ .

goal state $\mathbf{s_g}$ and registers the states with minimum cost until it gets to the initial state $\mathbf{s_i}$. The registered states define the collision free path for the robot.

The cost function $c(\mathbf{s})$ for a state $\mathbf{s}$ consists of two components: cost-to-come $g(\mathbf{s})$ that computes the cost to come from initial state $\mathbf{s_i}$ to the state $\mathbf{s}$ and cost-to-go $h(\mathbf{s})$ that computes the cost to go from state $\mathbf{s}$ to the goal state $\mathbf{s_g}$ as follows:

$$c(\mathbf{s}) = g(\mathbf{s}) + h(\mathbf{s}) \tag{6.1}$$

A heuristic cost function is defined to estimate the cost-to-go $h(\mathbf{s})$ that takes the cost due to the action taken to transition to the neighboring state into account as presented in the following equation:

$$h(\mathbf{s}) = t(\mathbf{s}, \mathbf{s}', \mathbf{a_t}) + e(\mathbf{s}', \mathbf{s_g}) \tag{6.2}$$

where, $t(\mathbf{s}, \mathbf{s}', \mathbf{a})$ is the transition cost from state $\mathbf{s}$ to the neighboring state $\mathbf{s}'$ with the execution of an action from action set $\mathbf{a_t}$, and $e(\mathbf{s}', \mathbf{s_g})$ is the Euclidean distance from the state $\mathbf{s}'$ to the goal state $\mathbf{s_g}$. Since the new microcoil system is capable of actuating the robot in any direction the transition cost $t(\mathbf{s}, \mathbf{s}', \mathbf{a})$ is calculated as the distance between the two neighboring states $\mathbf{s}$ and $\mathbf{s}'$.

## 6.7 Experimental Results

The autonomous actuation of the R3 type robot(s) using feedback control is demonstrated here. The single robot navigation test demonstrates the capability of the microcoil to actuate the microrobot in all locations in the workspace. The two robot navigation test shows the ability of the microcoils to independently actuate two microrobots in the workspace. Finally, a single robot navigation which avoids obstacles in the workspace is presented to illustrate the automated path planning and control technique.

### 6.7.1 Single Robot Navigation Tests

Single robot navigation tests are conducted first to demonstrate the capabilities of the microcoil platform. The local microcoils are used to move the microrobot towards the user-defined waypoints along the workspace. The control laws prescribed in Sec. 6.6 were used with feedback information from the captured images to keep the robot on track to reach the waypoints. The feedback image was first calibrated for the positions of the microcoils in the workspace. The position of the robot is measured through color thresholding and localized through the K means clustering function for

measurement of the center of the robot. This tracking approach produced a standard deviation of 1 $\mu m$ in both the X and Y axes with a feedback rate of 20 Hz. The 1 $mm$ diameter type R3 microrobot was used for the experiments. The switched on microcoils have 0.2 A current and each control action switches the microcoils on for 0.05s at a time.

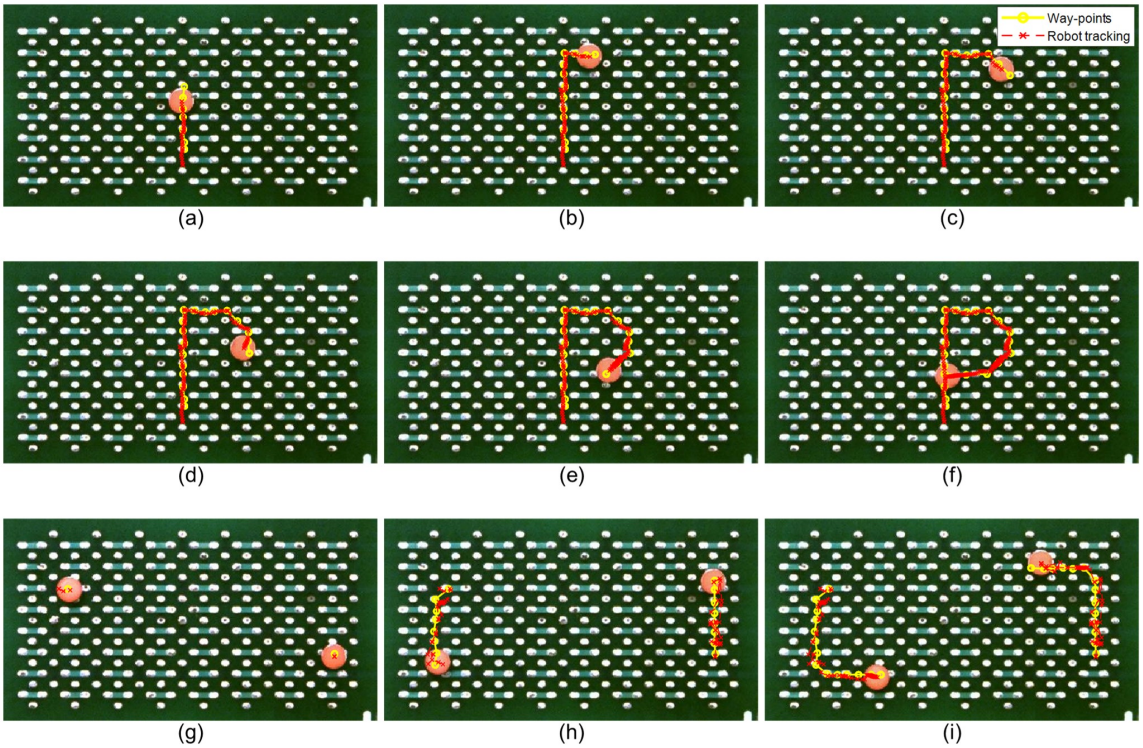


Figure 6.8. : (a)-(f):Closed loop control of a single R3 type robot moving along prescribed waypoints in a P-shaped trajectory. (a) R3 moving between two coils in the X axis (b) R3 moving in the +X axis (c) R3 moving in diagonal direction. (d) R3 moving in the Y axis along coils in the X axis (e) R3 moving in diagonal direction. (f) R3 moving in the -X direction. (g)-(i) Closed loop independent control of two R3 type robots moving along prescribed waypoints at two ends of the workspace.

The waypoints to define a P-shaped trajectory were chosen to showcase the different motion capabilities of the microcoil platform at different locations in the workspace. The control algorithm was successfully able to traverse the path au-

tonomously, as shown in Fig. 6.8(a)-(f). The velocity of the robot can slow down at times since the microcoil actuation force depends on the relative distance between the microcoil(s) and the robot as it traverses the workspace. In future, these attributes will be included in the path planner to choose waypoints that ensure the quickest path to the goal location is achieved.

### 6.7.2 Multi-Robot Navigation Tests

To demonstrate the capability of the microcoil platform for multi-robot independent control, two 1 $mm$ diameter type R3 robots are tested independently in the workspace. The control laws used here are similar to the one in Sec. 6.6. The waypoints are provided by the user and a time step of 0.4s was used. The time step is larger compared to the single robot navigation tests because of the interaction force between the robots. The larger time steps provide forces for longer periods which helps keep up the momentum of the robots in the workspace needed to overcome the interaction forces. Another consideration is the additional number of microcoils that need to be actuated at one time to operate multiple robots simultaneously. The limitations in hardware restrict the number of microcoils that can be switched on or off at a time. Therefore, activating all the microcoils can take additional time depending on the number of microcoils that need to be actuated. The control scheme was set such that both robots reach their respective intermediate waypoints before moving to their next waypoint. This is important to prevent the robot-robot interactions from affecting the motion of the robots in the workspace.

The robot motion is restricted due to their mutual interaction as discussed in Sec. 6.5.4. The independent horizontal, vertical, and diagonal motions of the robots are demonstrated when the robots are at a sufficient distance from each other in Fig. 6.8(g)-(i). The robot-robot interaction can also be seen in Fig. 6.8(i) where the goal point of robot 2 was not achieved due to the inability of the underlying microcoil to overcome the interaction force of robot type R3. The interaction forces, coupled

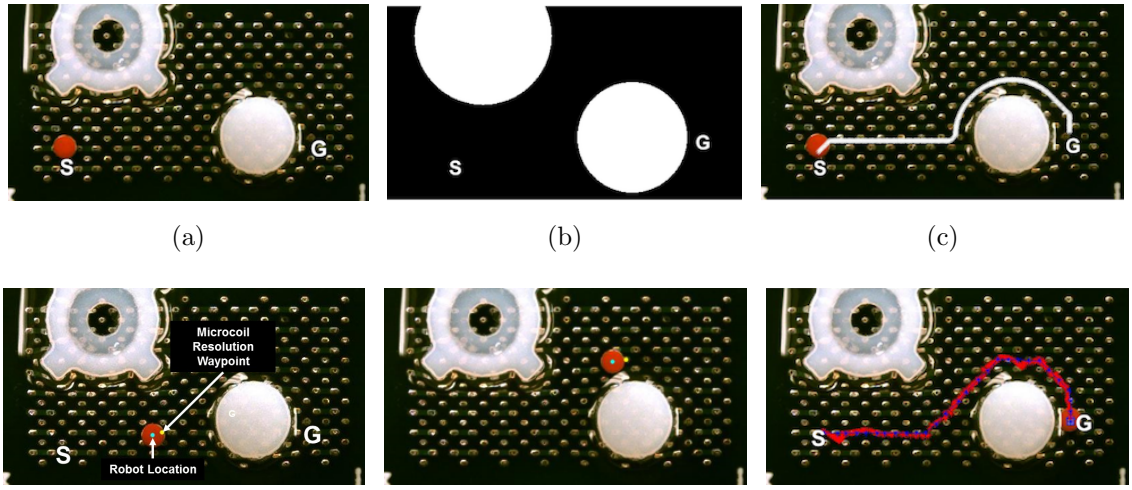


(a) (b) (c)

(d) (e) (f)

Figure 6.9. : Autonomous navigation of a robot by avoiding multiple obstacles in the workspace: (a) Initial scene with the robot placed at the starting location $S$ and goal location marked as $G$. (b) The obstacles are detected by processing the image with color thresholding and feature detection. (c) The computed path at pixel resolution. (d) Snapshot of the robot navigating autonomously along the planned path to a resampled microcoil resolution waypoint. (e) Snapshot of the robot avoiding obstacles and navigating along the planned path. (f) Robot successfully reaches the goal. The sampled waypoints (blue) and actual path (red) of the robot are shown.

with the workspace dimensions prevent the robots from getting too close to each other and hence they are restricted to the left and right ends of the workspace.

### 6.7.3 Single Robot Navigation with Obstacle Avoidance

The obstacle avoidance behavior of a robot is demonstrated by navigating it in an environment with multiple obstacles. Figure a shows the initial scene with the starting location of the robot marked as $S$ and the goal location as $G$. The locations are selected carefully to trigger the obstacle avoidance behavior of the robot during the navigation. The first step is to detect the obstacles. The image from the overhead

camera is processed with color thresholding and feature detection above a certain size to determine the locations of the obstacles as well as to store the initial and goal locations of the robot in image coordinate (shown in Fig. b). The obstacles are artificially grown to provide a safety zone so that the robot cannot get too close to the obstacles. The A* planning algorithm described in Sec. 6.6.2 then discretizes the workspace at a pixel resolution and computes the shortest path between initial and goal locations (shown in Fig. c). In this experiment, the workspace is discretized in a $290 \times 536$ rectangular grid. However, the waypoints are executed at a microcoil resolution and hence have to resample the path calculated by the planning algorithm. The resampled waypoints are passed into the microcoil activation algorithm described in Sec. 6.6.1 and shown in yellow in Figs. d-(e).

Figures d-(f) show the robot navigating in the workspace while avoiding obstacles autonomously. The instantaneous positions of the robot are detected from the image and the distance error between the actual position of the robot and the desired waypoint are used to determine the microcoils that need to be activated and the corresponding current values. The sampled waypoints are marked in blue and the instantaneous positions of the robot are marked in red (Fig. f). The robot follows the waypoints smoothly to reach the goal location.

## 6.8 Orientation Controls

As discussed in Sec. 6.5.5, the forces generated in the workspace do not allow control of orientation of the robot. This can make manipulation very challenging. With orientation control, a specific side of the robot can be designed for manipulation. The design of a new microrobot capable of orientation control along with a tailored manipulation side will be described in this section.

### 6.8.1 Microrobot Design For Orientation

The force generated on a robot by a set of microcoils is assumed to be along the centroid of the magnet, where the net magnetic moment acts. For a simple disc magnet as the robot, this location coincides with the center of mass. The torques generated by the microcoils around the center of mass are much lower than the actuation forces. Therefore, the robot will not rotate during its motion. However, if the center of mass of the robot is offset from the location of the magnetic moment, the net force is similar to a force-moment couple acting on the center of mass as shown in Fig. 6.10(a),(b). This moment attempts to align the center of mass and the magnetic moment location with the force generated by the microcoils. This feature aligns the robot along a desired direction of pushing at any point in the workspace. By designing a robot with the center of mass offset from the magnetic centroid, the orientation of the robot can be controlled using the motion of the magnet.

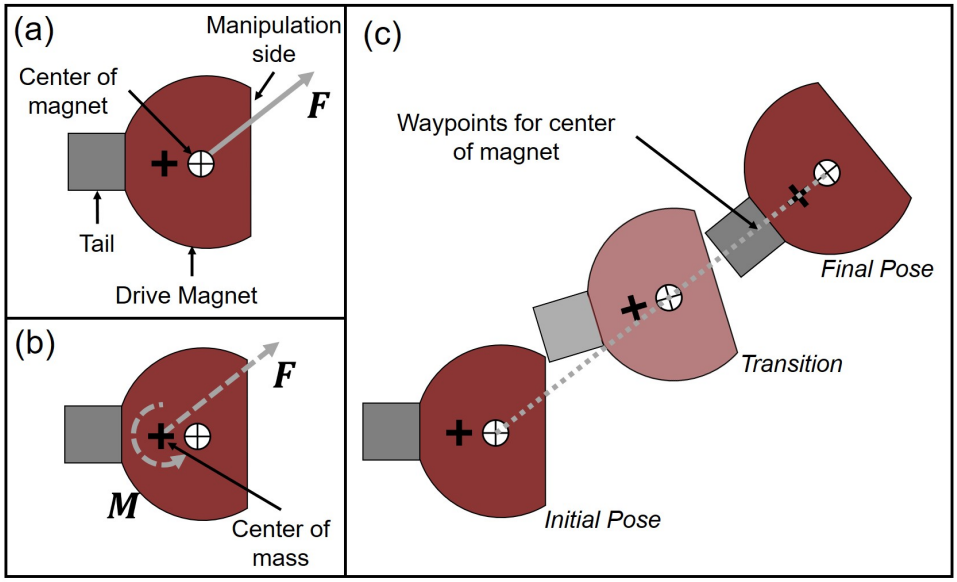


Figure 6.10. : (a) Robot with drive magnet (N52 grade 1.50 $mm$ diameter and 0.50 $mm$ thick disc magnet) and aligned tail (0.50 $mm$ side cube magnet) opposite to the manipulation side of the robot; (b) Equivalent force-moment couple for force shown in (a); (c) Sample path of a robot from an initial pose to a final pose.

### 6.8.2 Microrobot Fabrication

For this study, the robot was fabricated using a main 'drive' magnet which is a N52 disc magnet of diameter 1.50 $mm$ and 0.50 $mm$ thickness. A segment of this magnet was cut to form a flat surface for manipulation.The center of mass of the robot was shifted by using another N50 0.50 $mm$ cube magnet, which was stuck to the opposite end of the flat edge, as shown in Fig. 6.10(a). The position of the tail determines the robot heading. Therefore, the tail should be positioned opposite to the manipulation side. The magnetization of this 'tail' cube magnet is along the plane and hence does not affect the motion of the robot. The magnitude of torque generated to this magnetic tail is also negligible. This shifted the center of mass of the robot to the black cross as shown in Fig. 6.10(c).

### 6.8.3 Validation Experiments

A number of validation experiments were conducted. First, a robot with only the drive magnet segment is controlled to move along the workspace and was shown not to rotate during its motion. The magnetic center of the robot is the same as its center of mass. Thus, the orientation of the robot stays constant throughout its motion, as shown in Fig. 6.11. Next, a robot with an offset tail section from the manipulation side of the robot was then tested to observe that the robot orients along the direction of the tail. A robot with an aligned tail (as illustrated in Fig. 6.10) was tested next to show that it can successfully align the robot heading with the manipulation side of the robot. A turning radius of $\approx 5$ $mm$ was observed in these tests. Finally, to remove uncertainties due to the magnetic properties of the cube magnet, an aligned 0.60 $mm$ diameter steel ball was attached to the drive robot instead of the cube magnet. The mass of the attached ball shifted the overall center of mass of the microrobot and yielded similar controlled orientation behaviors.

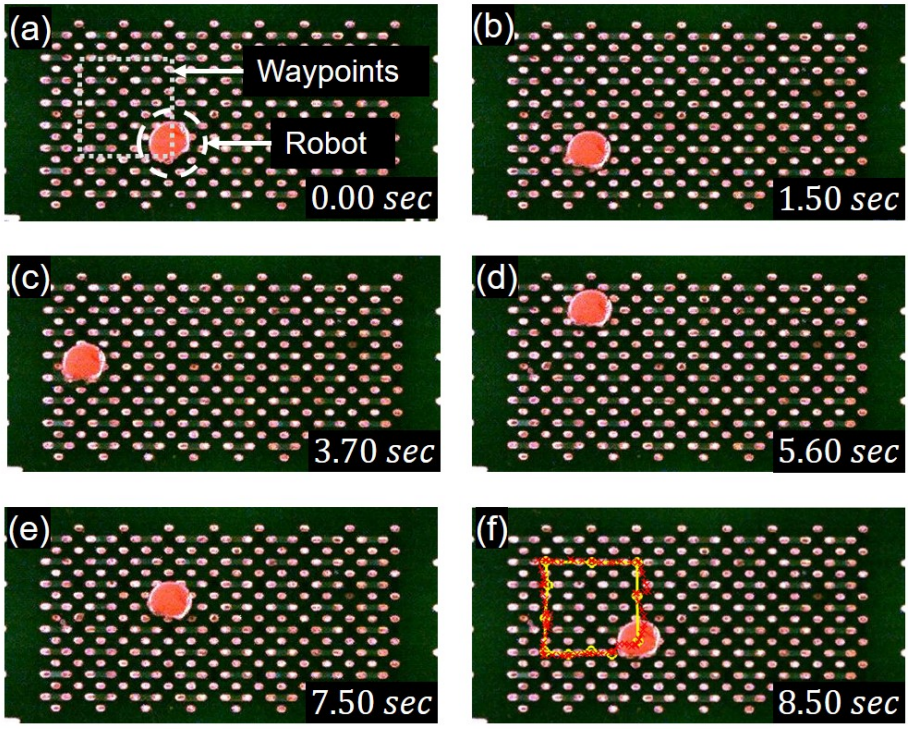


Figure 6.11. : (a)-(e) Path of a single N52 grade 1.50 *mm* diameter, 0.50 *mm* thick magnet segment as a robot. Note: the orientation of the robot does not change during its motion; the flat end of the robot is always at the the bottom. (f) The waypoints (yellow) and tracking of the robot.

### 6.8.4 Manipulation Experiments

Manipulation tasks taking advantage of the new orientation control of the robot were demonstrated. As shown in Fig. 6.12, the objective is to move the part from an initial pose (Fig. 6.12(a)) to a final pose Fig. 6.12(b)). The waypoints of the robot are generated manually to ensure that the robot pushes the object correctly and reaches the goal state (Fig. 6.12(c)-(h)). The manipulation was achieved by using the manipulation end of the robot for pushing the object.

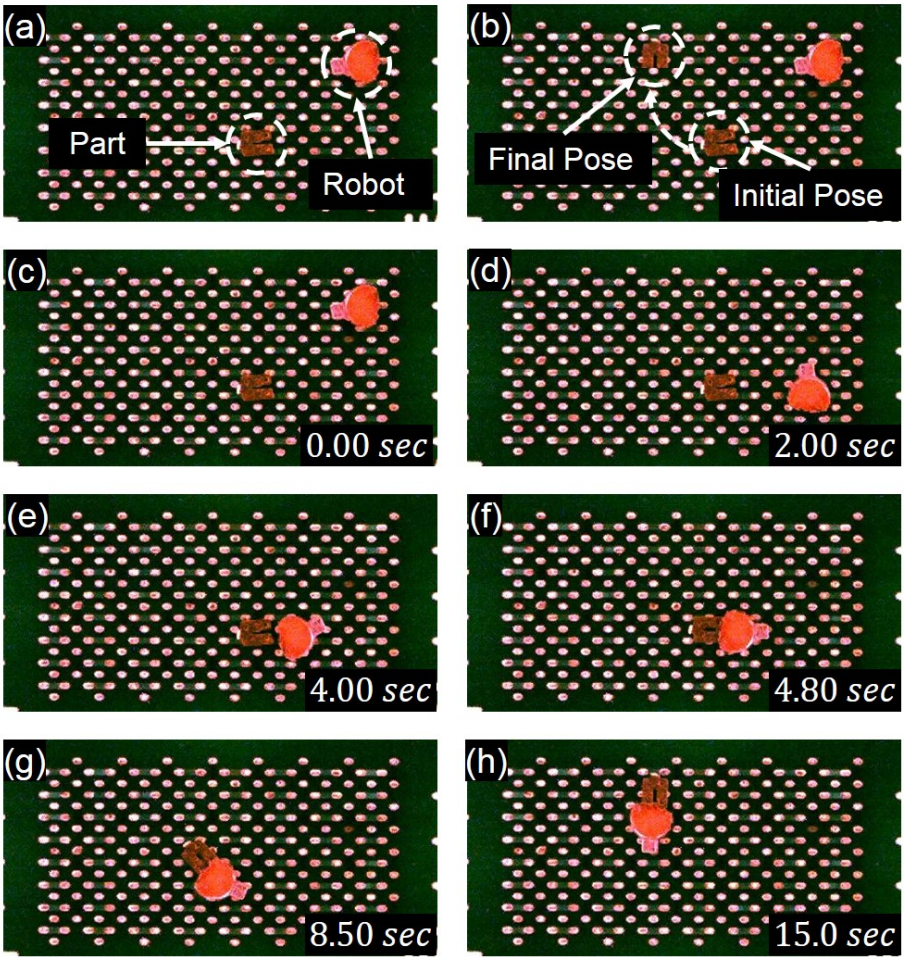


Figure 6.12. : (a) Newly designed robot and part in the workspace. (b) The initial and final poses of the part to be manipulated. (c)-(h) Manual control of the robot to transport the part from the initial to the final pose.

## 6.9 Expanded Microcoil System

The use of permanent magnets limits the number of robots that can be operated independently in the workspace using the microscale magnetic field generating system. The interaction between the robots are significant in the current workspace dimensions. To enable the independent actuation of multiple ($> 2$) robots, the workspace dimensions must be increased. However, since the robots themselves cannot come

closer to each other, the coils do not have to be localized as designed in the previous section. Hence, a larger workspace can be designed with the same number of coils. Longer coils can be used to form zones in the workspace to enable a larger number of robots to operate simultaneously. This can be visualized in Fig. 6.13 where the 16 coils used for generating local fields (Fig. 6.13(a)) can be scaled up to generate fields for an area four times larger (Fig. 6.13(b)). The new workspace would be 4 times larger than the existing workspace and would allow the actuation of up to four robots (Fig. 6.13(c)).

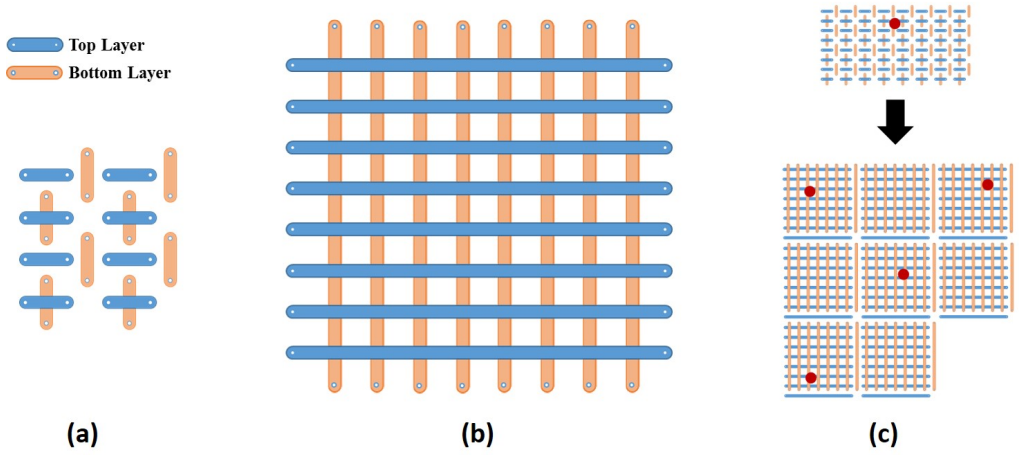


Figure 6.13. : Proposed coil design. (a) Old coils which use 16 coils, (b) New design which uses 16 coils, (c) Overview of the old coil design with a single robot and new design with multiple robots.

## 6.10 Discussion and Conclusion

In this chapter, the design and analysis of a new microscale local magnetic field generating system to independently actuate multiple microrobots in a 2D plane was presented. The newly designed system is able to generate magnetic field gradients in orthogonal directions in the plane. The microcoils in the second layer are also able to generate sufficient magnetic field gradients in the workspace, while the traces

below it are spaced adequately to eliminate their influence in the workspace. A fluid environment was used to minimize the frictional forces in the workspace, which enabled the magnetic forces generated to push the robot through the workspace. Robots which were disc magnets of diameter 1.5 $mm$ and 1.0 $mm$, and 0.5 $mm$ thick were successfully actuated in the workspace. The localized magnetic field was capable of driving the robots to their prescribed waypoints. The magnetic robot can autonomously navigate in the workspace smoothly while avoiding obstacles. An A* based graph search algorithm was also integrated in the automated computation of local magnetic fields to ensure the successful navigation of a robot in a realistic workspace with multiple obstacles.

A new microrobot design also enabled the orientation control of a microrobot for performing micromanipulation tasks. The actuation force is sufficient to manipulate small objects and the orientation capabilities allow pushing objects in specific directions using the manipulation end-effector. In future, other end-effectors types can be designed that provide specific functions such as force sensing or payload delivery to such robots. Path planning to find optimal trajectories to manipulate the objects and the implementation of multiple robots in the same workspace performing parallel tasks are also areas of future work.

Since the robots were magnets, their mutual interactions were significant and hence didn't allow for their close interaction in the workspace. This also restricted the number of robots that could be actuated in the workspace at a time. For the possibility to actuate multiple robots in a small workspace, the magnets used for the robots have to be smaller to reduce the interaction forces. However, the limitations in how close the vias can come together restricts the design discussed in this chapter to actuate smaller magnets. These issues will be tackled in the following chapter.

# 7. SERPENTINE COIL BASED MICRO SCALE ROBOTIC PLATFORM

In Chapter 4, planar spiral coils were designed into a PCB to control robots which were 3 $mm$ diameter and 0.5 $mm$ thick N52 disc magnets. The vias in this configuration were placed far apart as a prospective design to scale down the design to actuate micromagnets. However, these coils require advanced modeling and control to achieve simple motion tasks (Chapter 5). The design of local field generating coils resulted in lower current magnitudes that requires use of stronger neodymium magnets for generating sufficient actuation force. These magnets have inherent interactions between each other which restricts how close they can approach each other in the same workspace. Hence independent control of each robot is only possible in a specific zone which is sized at the minimum interaction distance.

In Chapter 6, the microcoils were designed into a PCB to generate local magnetic field in an area of 1 $mm \times 1$ $mm$ for a 1 $mm$ diameter, 0.50 $mm$ thick neodymium N52 disc robot. However, the required spacing between the vias that was manufacturable by advanced PCB manufacturing techniques restricted scaling down the size and spacing of the coils to enable actuation of smaller robots.

In this chapter, the design, development and analysis of a microrobot actuation system that is capable of simultaneous, independent control of up to four magnetic microrobots is presented. In Sec. 7.1, the design of a new magnetic coil system, which resembles in operation that of a stepper motor, is discussed. The design of 750 $\mu m \times$ 500 $\mu m \times 300$ $\mu m$ microrobot to be actuated with the coil system is then presented. The implementation and validation tests for the new coil system and microrobot designs are presented in Sec. 7.2. The capabilities of the system are showcased in Sec. 7.3 through independent closed-loop control tests with four microrobots and a demonstration of a sample micromanipulation task that involves pushing 3D printed

micro-parts. Finally, the results from these experiments are discussed, along with conclusions, in Sec. 7.4.

## 7.1 Actuation System and Microrobot Co-Design

The design of the new actuation system and microrobots are discussed in this section. The goal is to design a magnetic coil system that is able to actuate a sufficiently small neodymium magnet (250 $\mu$m cube) (which has sufficient magnetization for actuation at this scale) for use as a component of a new mobile microrobot design. The the new mobile microrobot must be designed in a way that that both position and orientation control are possible in the workspace using the magnetic coil system. Finally, the interaction between the new microrobots designs must be investigated for the practical aspects of using these microrobots to perform simultaneous independent tasks in the workspace.

### 7.1.1 Coil Design

The PCB traces that form the coil are laid out to attract a 250 $\mu m$ cube magnet into a stable local equilibrium area. This area is formed at the intersection of a pair of orthogonal serpentine shaped planar coils (Fig. 7.1 (top)). For a configuration of current directions, the coils generate net magnetic moments in the out-of-plane direction. However, the moments generated by a simple pair of these coils do not overlap and hence won't allow for motion of the robot in the 2D plane at any given configuration of currents. By adding another set of orthogonal traces circuits laid at the interval of the previous pair, intermediate stable equilibrium areas can be generated to obtain motion of the robot in the 2D plane.

The traces are spaced to ensure that a 250 $\mu m$ cube magnet fit inside the equilibrium zone. The gap between the centers of two adjacent traces of a single serpentine coil is 16 $mils$ ($\approx$ 406 $\mu m$), so that the gap between the inner edges of the traces would be equal to 250 $\mu m$ to fit the magnet. The width of the trace is set at 6 $mil$

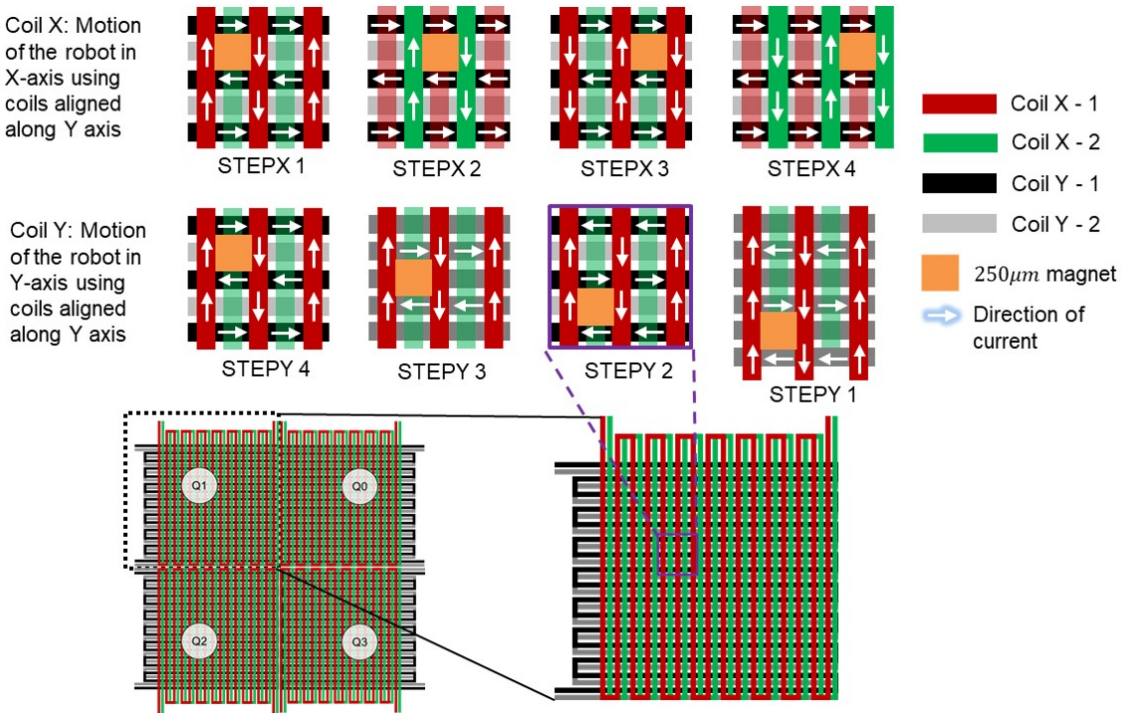


Figure 7.1. : Serpentine shaped planar magnetic coil actuation system: Actuation scheme for controlling a 250 $\mu m$ cube magnet using the four layer *Coil X* and *Coil Y* magnetic coils (top). Four layers of serpentine coils are laid out in four separate quadrants(Q0-Q3) where four robots can be independently actuated (bottom).

(approximately 150 $\mu m$) to ensure that the magnet microrobot is over the width of a trace at all times in the workspace. The configuration of currents in the coils can be replicated by designing the coil segment as part of a longer serpentine shaped coil system as shown in Fig. 7.1 (bottom).

### 7.1.2 Actuation Scheme

The design of the coil system resembles the serpentine shaped coils designed at SRI for the actuation of larger milli-scale robots made of an array of magnets using using diamagnetic levitation [86]. The robots used in this system are larger milli-scale robots made from an $4 \times 4$ array of $1.4 \times 1.4 \times 0.4$ $mm$ magnets. Although these

robots can be actuated in small increments of up to 40 $\mu m$, they are large in size and hence require a large workspace to independently actuate multiple robots. These orientation control of these robots are not possible without mechanical constraints in the workspace [99]. Several challenges exist for this design to actuate single magnets at the microscale. This includes the lower peak actuation force due to the reduced magnetic volume and the effect of the earth's magnetic field on a single micro-scale robot in the workspace. The actuation scheme used here to control a microrobot along each axis is shown in Fig. 7.1 (top). The actuation is similar to the operation of a two-phase bipolar stepper motor for motion along each axis. The steps for moving along each axis are shown in Fig. 7.1 (top), where four steps are shown to move the microrobot to a new equilibrium position. The set of coils that move the robot along the X-axis and Y-axis are named *Coil X* and *Coil Y*, respectively. (The -1 and -2 labels correspond to different layer locations in the PCB). Since the four coils are on different planes, the currents to the four coils are computed to generate equal fields in the workspace. The currents used in this actuation scheme is uniquely defined based on the step number, based on the total number of steps using a sine-cosine microstepping approach [100]. The currents in *Coil X* are given by

$$\phi = \frac{2\pi}{\#\ of\ steps} \tag{7.1}$$

$$I_1 = I_{1max} cos\phi \tag{7.2}$$

$$I_2 = I_{2max} sin\phi \tag{7.3}$$

where $\phi$ is the step angle in radians and $I_1$ and $I_2$ are the currents to *Coil X* based on the *step* value. Similarly, for *Coil Y*, $I_3$ and $I_4$ can be determined. The minimum count of steps is four, but the system can also be configured in microstepping mode to generate additional steps for the same segment of the coil by generating mixed signals on the two circuits based on the equations above. To enable independent control of multiple robots in the workspace, the serpentine coils are laid in four separate quadrants (Q0-Q3) where four robots can be independently actuated (Fig.7.1 (bottom)). The layout of the coils are designed so that the robots can transition from one

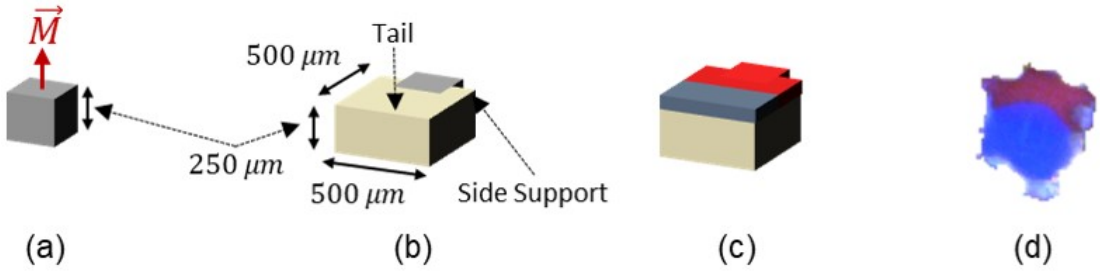


Figure 7.2. : Microrobot Design: (a) 250$\mu m$ cube magnet with magnetization vector **M** (b) Dimensions of the 3D printed part that attaches to the magnet with the side support and tail sections. (c) Red and blue colors added to the microrobot to calculate position and orientation. (d) Top-view of an assembled robot.

quadrant to another by ensuring the gaps between the quadrants are identical as the gap between the traces within each quadrant.

### 7.1.3 Microrobot Design

The 250 $\mu m$ cube magnet is the driver of the robot. For successful actuation of the robot, the magnet must be aligned such that its magnetization direction **M** is out of the plane of the surface of the workspace, as shown in Fig. 7.2(a). However, in the absence of field in the workspace, these tiny magnets tip over to align with the earth's magnetic field. This is prevented by providing sufficient side support structure for the magnet, as shown in Fig. 7.2(b).

To enable orientation control, the center of mass of the robot has to be offset from the magnetic center [97]. This can achieved by adding a *tail* segment at the back of the robot (Fig. 7.1(b)). To achieve these objectives, while keeping the size of the robot under 1 $mm$, a 3D printed part (Projet MJP2500, 3D Systems, Inc., USA) is designed to be attached to the 250 $\mu m$ cube magnet as shown in Fig. 7.2(c). The side walls provide support to prevent tipping when the robots are not being actuated by the coils. The tail section shifts the center of mass of the robot to enable preferred

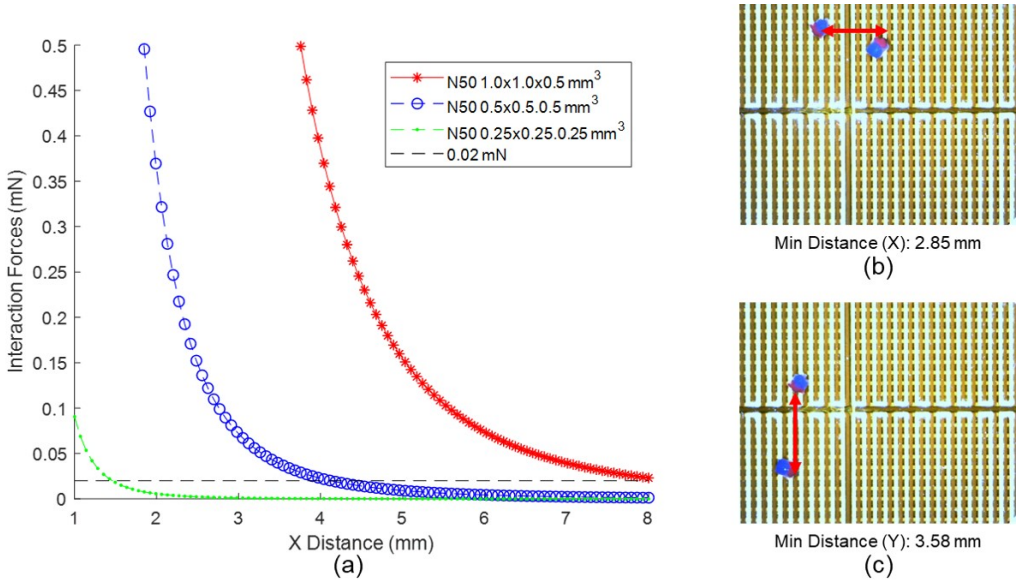


Figure 7.3. : (a) Interaction forces comparing the 250 $\mu m$ N50 cube magnet with a 500 $\mu m$ N50 cube magnet, and a 1 $mm \times 1$ $mm \times 0.50$ $mm$ N50 cube magnet for the peak actuation force of a magnetic coil at a depth of 85 $\mu m$ (current = 0.08 $A$). (b) Experimental verification of interaction force along X axis (c) Experimental verification of interaction force along Y axis.

orientation control. The tops of the robot is painted with blue and red colors to aid in feedback of position and orientation of the robot during actuation. An overhead view of the robot is shown in Fig. 7.2(d). For closed loop control, the position and orientation of the robot has to be measured. To enable this, colored features are added to the robot to allow detection using color thresholding algorithms. The position and orientation of the robot are calculated using methods in Sec. 3.5.

### 7.1.4 Multi-robot Interaction

The permanent magnetic nature of the microrobots introduce interactive forces between multiple robots in the workspace. To ensure that these robots do not collapse in to each other during actuation, the magnetization vector of all robots are main-

tained in the same direction which introduces repulsive forces between the robots. However, this restricts how close they can come together in the workspace due to these repulsive forces overcoming the actuation force. On evaluating the repulsive force between similar magnets, 250 $\mu m$ cube magnets experience far less interaction forces compared to 0.5 $mm$ cube magnets which enables them to work as close as 2 $mm$ to each other (Fig. 7.3(a)). This is also restricted by the peak force that can be applied to the magnet with the coils for a N50 cube magnet of size 250 $\mu m$ (SuperMagnetMan, USA). This is estimated to be 0.2 $mN$ for 0.08$A$ at a depth of 85 $\mu m$ underneath the magnet. Hence, the microrobots should be maintained at distances larger than 2 $mm$ to ensure unaffected motion through the workspace from the other microrobots.

## 7.2 Implementation and Validation

### 7.2.1 Microcoil Platform

The microcoil platform is shown in Fig. 7.4(a). The platform consists of the workspace where the serpentine coils are fixed, an overhead camera-lens system for image feedback of the workspace, a coil controller board to control the current in the coils, and an Arduino microcontroller that is capable of communicating between the coil controller board and the computer that processes the feedback images.

The specifications of the workspace is shown in Table. 7.1. The workspace consists of two flexible PCBs, each containing two layers of coils capable of moving a robot along a single axis (*Coil X* or *Coil Y*). Two-layer flexible PCBs were chosen due to their low thickness (100$\mu m$ for a 2-layer board) which maximizes the magnetic field generated by lower coils at the surface of the workspace. Each PCB has eight inputs for current for the two sets of coils in each quadrant. The PCBs are aligned and attached with double sided tape (89 $\mu m$ thick, 3M 665) at an orthogonal angle to allow motion in both the X and Y axes. This ensures that the surfaces do not move, and that working fluid doesn't get in between the two PCBs during actuation.

Table 7.1. : Serpentine Coil Based Microrobot Actuation System

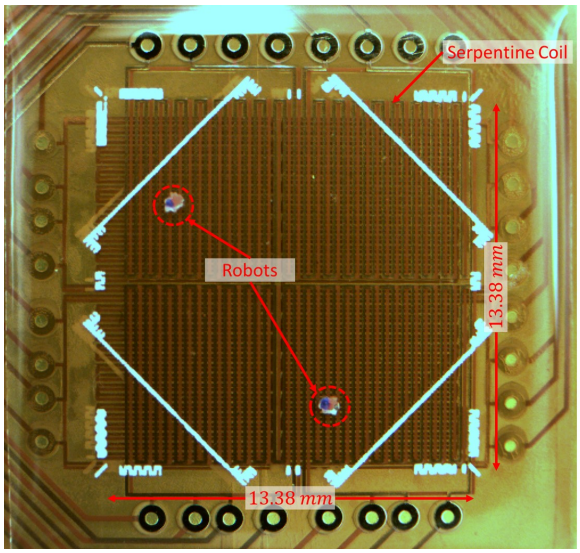


| | |
|---|---|
| References | [97] |
| Coil Type | Serpentine |
| Number of coil layers | 4 |
| Number of coils | 8; One each in X and Y in four quadrants |
| Coil Dimensions | 6.69 $mm \times 152\ \mu m$ |
| Coil Spacing | $193\ \mu m - 211\ \mu m$ |
| Workspace Dimensions | 13.38 $mm \times 13.38\ mm$ |
| Movement Type | Microstepping |
| Robot Footprint | $\geq 250\ \mu m$ |
| Direction Control | X and Y |

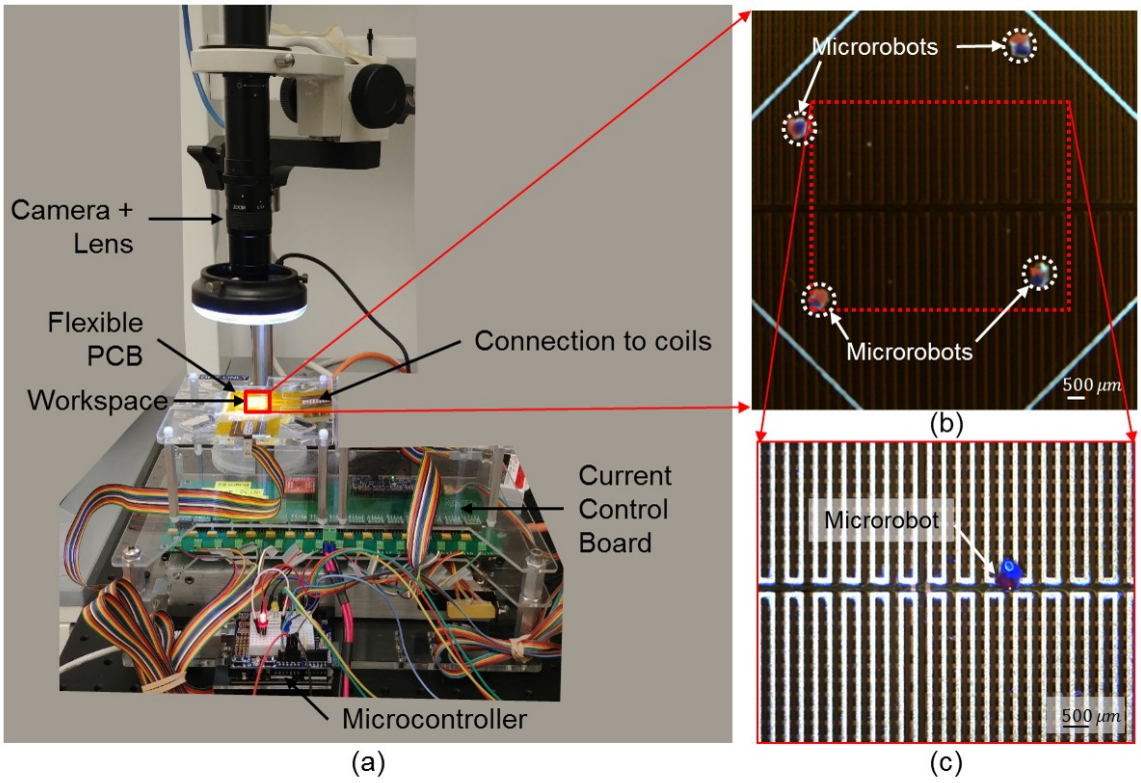


Figure 7.4. : (a) Overview of the microcoil platform: the workspace is formed at the intersection of the two flexible PCBs, the current control board supplies the current to the coils, the microcontroller is used to communicate between the computer and the coils, and the camera+lens system to capture images for feedback. (b) Overhead view of the workspace using a wide-angle lens (zoomed in). (c) Overhead view of the workspace using a zoom lens.

The position and orientation feedback is achieved through images captured by an overhead camera-lens system shown in Fig. 7.4(a). The camera (Point Grey FL3-U3-13E4C-C) is used to capture the overall workspace of 13.38 $mm \times 13.38$ $mm$ (Fig. 7.4(b)) while using a wide-angle lens (Tamron C-Mount 4-13mm Manual Iris Varifocal Lens) at a resolution of $750 \times 750$ $pixels$. For improved resolution of the motion and feedback images, a zoom lens (VZM™ 450i Zoom Imaging Lens, Edmund Optics) is used

to observe a smaller segment of the workspace of size 9.38 $mm \times 8.33$ $mm$ covered by a portion of all four quadrants (Fig. 7.4(c)) at a resolution of $1280 \times 1024$ $pixels$.

The currents in the serpentine coils are controlled using a single current control board discussed in Sec. 3.3. The current control board can power up to 16 coils, which is enough for all the coils in the workspace (4 coils in each quadrant). The current control board is accessible through an $I^2C$ interface that allows the control of all the coils using an Arudino microcontroller. Commands are sent from the computer (Intel® Core™ i7-4790 CPU @ 3.60GHz processor, 16.0GB RAM) to the arduino using serial communication through a visual studio program. The currents are generated through an external power supply (Mean Well RSP-320-2.5) that can supply up to 60 $A$ of current at 2.50 $V$. This allows for sufficient current to be supplied to the 16 serpentine coils at the same time. However, to eliminate excessive heat generation, the peak value of current is restricted to 0.65 $A$.

### 7.2.2 Workspace Preparation

Peak dry friction forces on glass cover-slips are in the range of 0.1 $mN$ [101]. Since this is comparable to the actuation forces of the magnetic coils, the microrobots are actuated in silicone oil medium to reduce these friction forces. The microcoil workspace is prepared for actuation by setting up a 22 $mm \times 22$ $mm$ No.0 (Thermofisher Scientific Gold Seal Cover Glass #3206) glass coverslip on top of the cleaned workspace. About 250 $\mu L$ of silicone oil (A12728, Alfa Aesar) is added to the middle of the coverslip and allowed to spread. This forms an uniform layer of the fluid that is thick enough to submerge the microrobot. The absence of walls prevent wall effects that may affect the movement of the robots.

### 7.2.3 Microstepping

The motion of the microrobots are controlled by regulating the currents in the four layers of coils as shown in Fig. 7.5(a). The motion in the X-axis is controlled

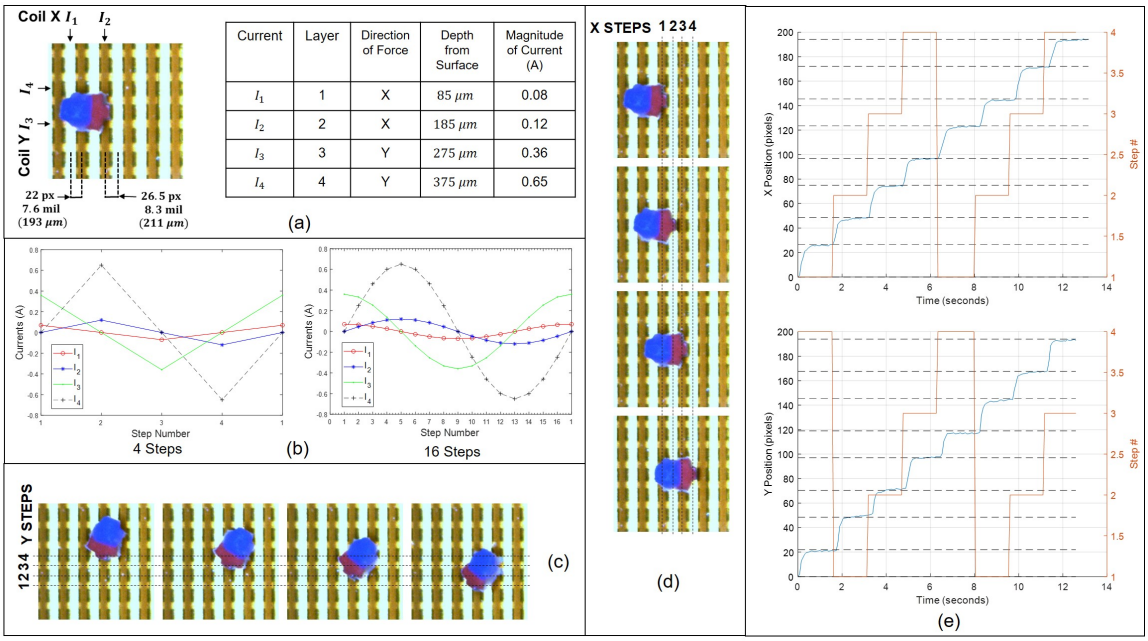


| Current | Layer | Direction of Force | Depth from Surface | Magnitude of Current (A) |
|---|---|---|---|---|
| $I_1$ | 1 | X | 85 $\mu m$ | 0.08 |
| $I_2$ | 2 | X | 185 $\mu m$ | 0.12 |
| $I_3$ | 3 | Y | 275 $\mu m$ | 0.36 |
| $I_4$ | 4 | Y | 375 $\mu m$ | 0.65 |

Figure 7.5. : Implementation and Validation: (a) *Coil X* and *Coil Y* dimensions and coil current variables. (b) Sine-cosine microstepping current values for four steps and sixteen steps cases. (c) Microrobot position for all *Coil X* steps. (d) Validation experiment of microrobot moving through steps in *Coil X* and *Coil Y*.

using the *Coil X* vertical traces that use currents $I_1$ and $I_2$. Similarly, motion in the Y-axis is controlled using the *Coil Y* horizontal traces that use currents $I_3$ and $I_4$. The magnitude of current has to be adjusted to account for the layer height of each coil to ensure equal generated magnetic fields in the workspace.

For four steps, the currents can be regulated as shown in Fig. 7.5(a) for moving the robot to the respective stable equilibrium points as shown in Fig. 7.5(c),(d). The current configuration for each step is shown in Fig. 7.5(b) for a total of 4 steps and a total of 16 steps, which can provide smoother motion in the workspace. The path of the robot in each axis is shown in Fig. 7.5(e) where the coil-microrobot system represents a first-order system of a time constant of $\approx 0.35$ *seconds* with a settling time of $\approx 0.45$ *seconds*. It should also be noted that the interval spacing between the upper and lower coils (eg. *Coil X* -1 and *Coil X* -2) are not uniform due to

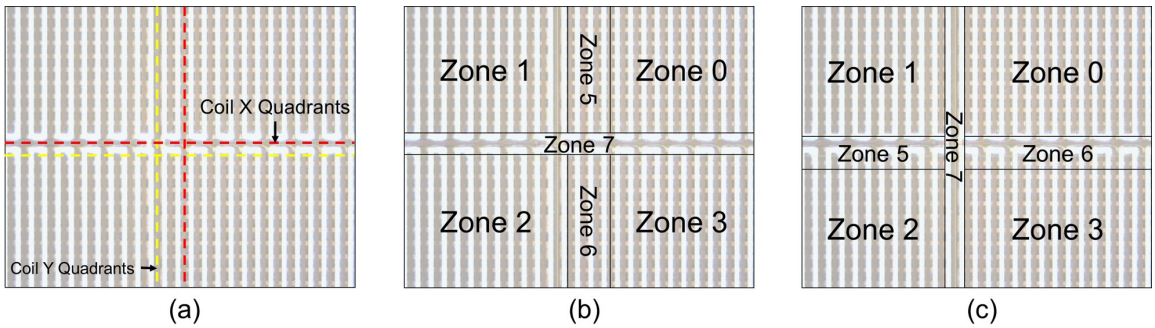


Figure 7.6. : *Coil X* and *Coil Y* divisions and zones for control: (a) *Coil X*-red and *Coil Y*-yellow divisions for quadrants Q0-Q3. (b) *Coil X* Zones for actuation along the X-axis. (b) *Coil Y* Zones for actuation along the Y-axis.

manufacturing tolerances as shown in Fig. 7.5(c),(d). However, the equilibrium points are reached during actuation due to the close packing of the coils. Also, the currents are tuned to ensure that the robots reach the equilibrium point between the coils during their step motion.

The motion of a robot can be independently controlled in each quadrant. The quadrant for each *Coil X* and *Coil Y* are shown in Fig. 7.6(a). To ensure that the microrobots can transition from one quadrant to another, the workspace is divided in to several zones as shown in Fig. 7.6(b),(c). Zones 0-3 require coils from a single quadrant to actuate the microrobot. Zones 5 and 6 require the adjacent quadrants to be in sync to ensure that the transition areas between the quadrants have the correct resultant field to ensure smooth motion between the quadrants. For this, when the microrobot enters zone 5 or 6, the step number of the quadrant in which the robot lies is equated to the adjacent quadrant. Zone 7 is a dead zone in the workspace for motion in each axis. Only a small (300 $\mu m \times 300\ \mu m$) area in the workspace is dead zone for both axes. However, in case a microrobot accidentally enters this zone, it can be moved in one axis using all the four coils surrounding this dead zone.

Zones 5 and 6 also include segments of the serpentine coil where it turns. This segment produces stray fields that impact the motion of the robot during motion

in the orthogonal axis. Hence, in zones 5 and 6 for *Coil X*, actuation using *Coil Y* is switched off to ensure that the stray fields do not interfere in the motion of the robot. Similarly, zones 5 and 6 for *Coil Y*, actuation along the X axis is disabled. This restricts the controllability of the robot in zones 5 and 6, but any point in these zones can be reached using the correct path planning techniques. Additionally, diagonal movements are possible in overlapping zones 0-3 in both *Coil X* and *Coil Y* by activating the steps in both axes.

### 7.2.4 Closed Loop Control

Closed loop control is achieved by maintaining the step count for X and Y axes on each quadrant of the microcoil platform. Each step has a combination of currents in the underlying coil that allow the robot reach the required equilibrium point. The algorithm to estimate how the steps change to move the robot from the current position, $\mathbf{r}_{pos}$, to $\mathbf{r}_{des}$, is shown in Algorithm 6. The strategy is to adjust the step count based on the error in position while making sure that the microrobots can cross across quadrants and prevent effects from stray fields. Delay time, $t$, is the time between steps and hence, it determines the speed of the microrobot.

### 7.2.5 Multi-robot Interaction

The interaction between multiple robots was tested by actuating two robots to approach each other in both the X and Y axes. The interaction distance was estimated as the distance at which one of the robots cannot repeatedly go to the next step during its motion. The interaction distance for the X-axis motion was found to be 2.65 $mm$ and 3.58 $mm$ for the y-axis motion, as shown in Fig. 7.3(b),(c). The higher distance for the y-axis motion is attributed to the lower position of the coils in layer 3 and 4 where the actuation force was observed to be less in spite of higher current settings.

**Algorithm 6** Determine the currents in the serpentine coils in the workspace.

**Input:** $\mathbf{r}_{pos}$: position of the robot, $\mathbf{r}_{des}$: desired goal position, $q\epsilon\{0,1,2,3\}$: quadrant of the robot, $stepX_q$: current step position of each quadrant of *Coil X*, $stepY_q$ current position in *Coil Y*, and delay time $t$.

**Output:** Desired step number of each quadrant of the platform to adjust the currents in the coils to ensure motion of robot towards goal .

**while** $\parallel \mathbf{r}_{des} - \mathbf{r}_{curr} \parallel \geq W_{th}$ **do**
  **for all** $a\epsilon\{x, y\}$ **do**
    Find $q$ using Algorithm 7.
    If size($q$)$>1$, equate the step number of both quadrants to the step number of the current quadrant of the robot.
    **for all** $q\epsilon q_a$ **do**
      **if** $a_{des} - a_{curr} \geq 0$ **then**
        $stepa_q = stepa_q + 1$
      **else**
        $stepa_q = stepa_q - 1$
      **end if**
    **end for**
  **end for**
  Set the appropriate currents for all quadrants according to values of $StepX_q$ and $StepY_q$.
  Wait for $t$.
  Get feedback of the current state of the robot, $\mathbf{r}_{curr}$.
**end while**

**Algorithm 7** Determine the quadrants for control of the robot.

**Input:** $q\epsilon\{0,1,2,3\}$: quadrant of the robot, $a$: current axis ($x$ or $y$), $z_x\epsilon\{0,1,2,3,5,6,7\}$: zone of the robot in X, and $z_y\epsilon\{0,1,2,3,5,6,7\}$ zone of the robot in Y.

**Output:** Desired quadrants that need adjustment for movement in axis $a$.

```
1: if z_a ∈ {0,1,2,3} then
2:    q = z_a
3: else
4:    if z_a = 5 then
5:       if a = x then
6:          q_1 = 0, q_2 = 1
7:       else
8:          q_1 = 1, q_2 = 2
9:       end if
10:   else
11:      if z_a = 6 then
12:         if a = x then
13:            q_1 = 2, q_2 = 3
14:         else
15:            q_1 = 0, q_2 = 3
16:         end if
17:      else
18:         Not controllable in axis a
19:      end if
20:   end if
21: end if
```

## 7.3 EXPERIMENTAL RESULTS

### 7.3.1 Visual Studio-Arduino Interface

The open and closed loop control of the robots in the workspace are achieved through a visual studio-arduino interface. The shift from the matlab-arduino interface (Sec. 3.4) was necessary to improve the frequency of control of the robot. This version of the code accelerated the feedback signal capability to 20 $Hz$. The magnitude of current in each coil is designated based on the step number of each coil. To restrict the serial command length, hexadecimal value is used to represent the magnitude of current. By individually controlling the step number of each coil, it is possible to switch off individual coils for transitioning between zones. The arduino code converts the serial commands to equivalent step numbers and converts to the appropriate currents based on the step angle (Eq.7.1,7.2,7.3).

For example, for a total of 16 steps, a serial command consisting of 16 characters for each of the 16 coils is used to represent the step number of each coil. For a serial command: '01012323A5A5B4B4', the currents in all the coils are shown in Table. 7.2.

### 7.3.2 Multi-robot Independent Motion

The ability of the platform to simultaneously control multiple robots independently has been achieved. Four microrobots are placed on the four quadrants of the 9.33 $mm \times 8.38$ $mm$ workspace. Five waypoints are defined for each microrobot (Fig. 7.7(a)). The coils are configured for microstepping with 16 steps and feedback was processed at 10 $Hz$ using Algorithm 6. The waypoints were updated only when all the robots reached their respective goal locations. The robots successfully traverse the workspace to reach the waypoints along the direction specified by the arrows (Fig. 7.7(b)). The motion of the robot is restricted to just $X$ or $Y$ axis at one time in this experiment. The path of these robots were controlled independently in their respective zones, and a tracked points representing the letters "PUWL".

Table 7.2. : Decoded coils from the string from Visual Studio

| Coil Number | Coil Axis | Layer | Quadrant Q(0-3) | Serial Command | Equivalent Step # | Step Angle $\phi$ ($^o$) | Current ($A$) |
|---|---|---|---|---|---|---|---|
| 1 | X | 1 | 1 | 0 | 0 | 0 | 0.040 |
| 2 | X | 1 | 0 | 1 | 1 | 22.50 | 0.037 |
| 3 | X | 2 | 1 | 0 | 0 | 0 | 0 |
| 4 | X | 2 | 0 | 1 | 1 | 22.50 | 0.038 |
| 5 | X | 1 | 2 | 2 | 2 | 45.00 | 0.028 |
| 6 | X | 1 | 3 | 3 | 3 | 67.50 | 0.015 |
| 7 | X | 2 | 2 | 2 | 2 | 45.00 | 0.071 |
| 8 | X | 2 | 3 | 3 | 3 | 67.50 | 0.092 |
| 9 | Y | 3 | 2 | A | 10 | 225.00 | -0.177 |
| 10 | Y | 3 | 1 | 5 | 5 | 112.50 | -0.096 |
| 11 | Y | 4 | 2 | A | 10 | 225.00 | -0.354 |
| 12 | Y | 4 | 1 | 5 | 5 | 112.50 | 0.462 |
| 13 | Y | 3 | 3 | B | 11 | 247.50 | -0.096 |
| 14 | Y | 3 | 0 | 4 | 4 | 90.00 | 0 |
| 15 | Y | 4 | 3 | B | 11 | 247.50 | -0.462 |
| 16 | Y | 4 | 0 | 4 | 4 | 90.00 | 0.500 |

### 7.3.3 Orientation Control

The offset between the center of mass of the robot and center of the magnets generates force-moment couple that orients the robot in the direction of motion. This is useful to push objects in the workspace in a desired orientation. The 3D printed tail of the robot offsets the center of mass of the robot from the center of the magnet. However, due to the large difference in the density of the magnet and the 3D printed material, this offset is low and hence the torque generated is low.

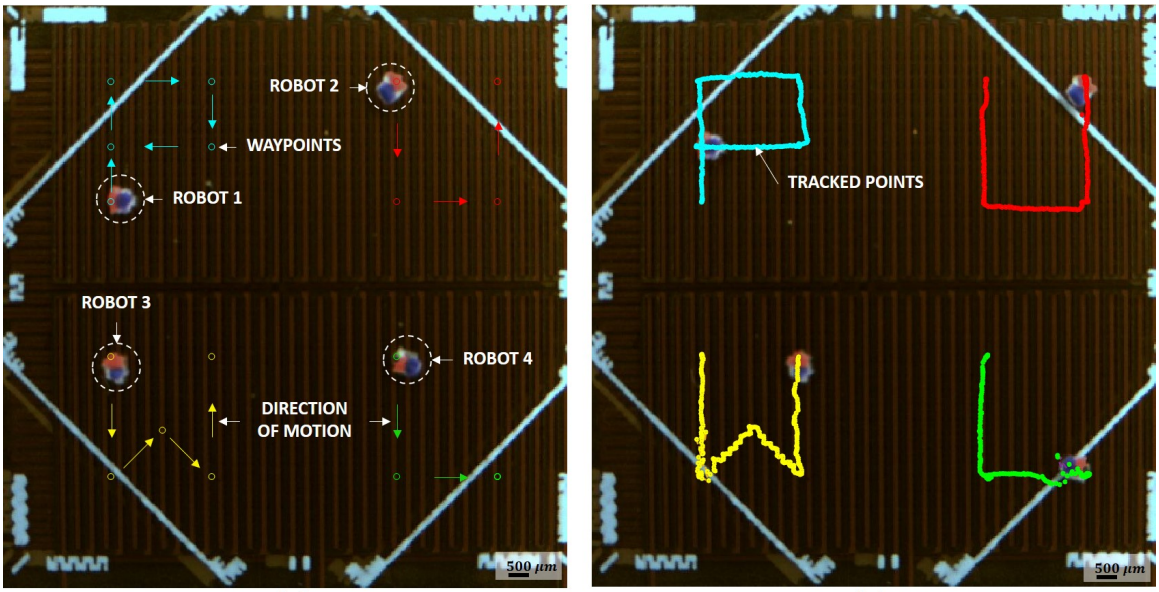


Figure 7.7. : Experimental Results: (a) Four microrobots and waypoints defined for each robot along the arrows. (b) Tracked path of the four robots to form the letters "PUWL".

The torque generated can be improved by increasing the velocity of motion of the robot which generates continuous force in the direction specified. This method is effective only through long paths and requires additional path planning to ensure correct orientation during manipulation tasks. The torque generated is highest when the force is orthogonal to the orientation of the robot. By dividing the workspace in to a higher step count, forces in orthogonal directions can be generated. An example of such a task done manually is shown in Fig. 7.8 where a total of 16 steps is used. The mean position of the robot is maintained while the position of the magnet follows the orthogonal force generated in the coils to adjacent equilibrium points. Also, slower motion of the robot doesn't produce as much torque and maintains the orientation which is useful in making small adjustments in position without changing the orientation.

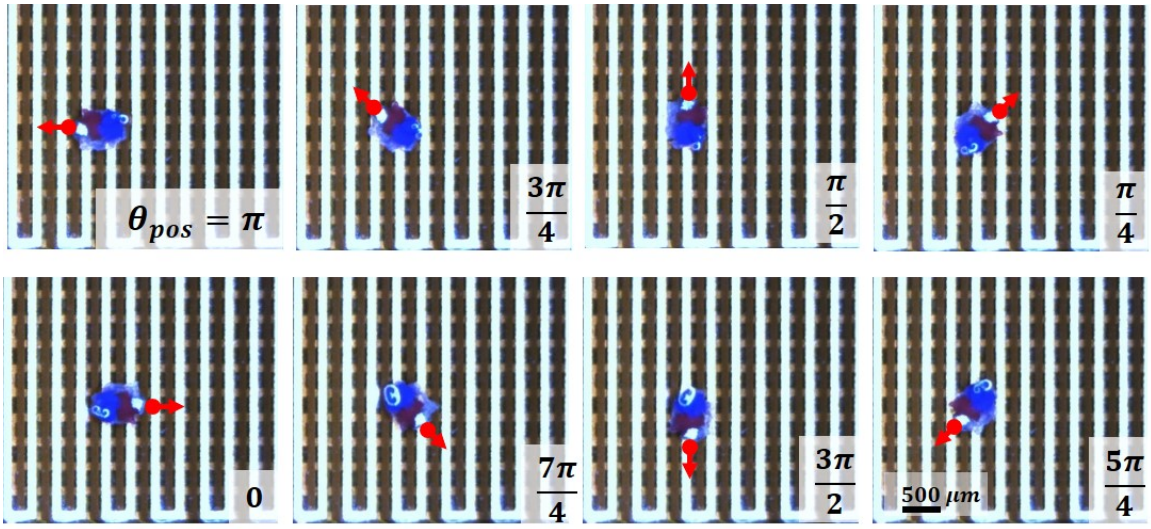


Figure 7.8. : Experimental Results: Orientation control of a microrobot by manually adjusting the steps to orient the robot in increments of $\frac{\pi}{4}$ *radians*.

### 7.3.4 Manipulation Tasks

The ability of these robots to work together to assemble parts at the microscale is demonstrated here. Two robots are used to assemble five parts (approx. dimensions of 1 $mm \times 1$ $mm$) moved from various areas of the workspace to form the letter "P" as shown in Fig. 7.9(a)-(i). The robots are able to operate independently when placed in separate quadrants. This task was achieved by using feedback control to move the robot from one area of the workspace to other using prescribed waypoints that force the robot to push the parts. In some cases, manual control of the robot was used to control the orientation and push the parts to increase the delay time needed to achieve sufficient force for successful manipulation.

The main challenges of manipulation was the variability in force required to push different parts, which is attributed to surface finish of the 3D printed parts. Also, the coils in lower layers that generate motion of the microrobot in the Y axis were observed to not be powerful enough at times to complete the pushing task in the first attempt and hence cycles through the steps were required to ensure that the waypoint

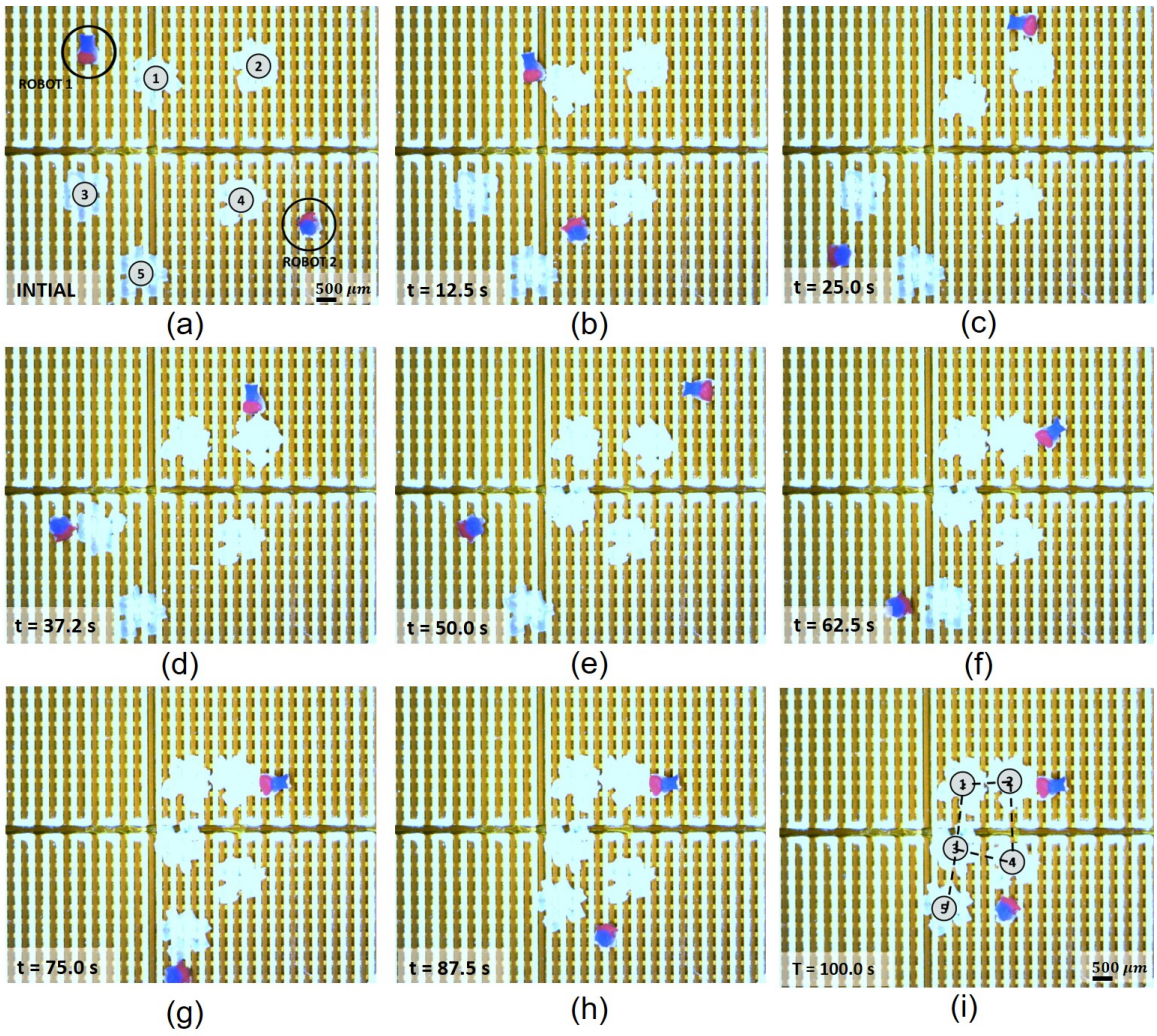


Figure 7.9. : Experimental Results: Manipulation tasks setup with two microrobots and four 3D printed parts numbered 1-5.

is reached. In some instances, manually controlled pushes were implemented to limit the number of cycles executed by increasing the delay time to ensure that robots reached the desired step. Another aspect is the tight workspace required for the image resolution needed needed for closed loop controls restricts the workspace for the robots to move in. A higher resolution camera and a wider field of view lens will enable the use of the entire workspace for fine motion control for micromanipulation tasks, and allow additional robots to work in the same workspace.

## 7.4 Results and Discussion

In this chapter, the design and analysis of a serpentine coil based micro-scale robotic system that is capable of simultaneous independent control of robots as small as 750 $\mu m$ was presented. The main driver of each robot is a neodymium 250 $\mu m$ N50 cube magnet which is attached to a 3D printed part for stability and orientation control. The overall robot is sized 750 $\mu m \times 500$ $\mu m$ in size and is painted to get feedback of its position and orientation for closed loop control. The motion of the robot using the coils resembled that of a stepper motor which enabled the use of sine-cosine functions to specify currents in the coils for smooth motion of the microrobot in the workspace. The experiments demonstrated the capability of the microrobot and platform to simultaneously actuate up to four robots independently and successfully perform manipulation tasks. The ability to control the orientation of the magnet is also demonstrated that has improved ability to perform manipulation tasks. This microrobotic platform has several advantages over the previous design that could do orientation control for sub-mm microrobots (Chapter 6). The smaller size of the magnet has reduced the interaction distance greatly, from $\approx$ 7 $mm$ to $\approx$ 3 $mm$. This has allowed the independent control of up to four microrobots in a comparable workspace. Another major improvement is the independent orientation control of each magnet by using the smaller step size and faster movements to achieve orientation control while staying in the same approximate position instead of the requirement to move long distances to orient the microrobot in a preferred direction.

This new coil system is somewhat restricted in the force generated for pushing and manipulation tasks. This can be improved by using stronger magnets of the same size. The size of the microrobot can also be decreased by using optimized designs that enable efficient shifting of the center of mass while offering side support to prevent accidental tipping. Feedback control would also include closed loop orientation control, which is currently only done manually or through moving long distances through the workspace. More sophisticated path planning techniques can also be used to consider

the zones that the robots operate to ensure successful transitions from one quadrant to another, which is an area of future work.

# 8. SUMMARY, CONTRIBUTIONS AND FUTURE WORK

## 8.1 Summary

In this dissertation, several local magnetic field generating systems for microrobot actuation was designed and analyzed. Robots ranging from mm sized (Chapter 4 and Chapter 5) to sub-mm sized (Chapter 6, 7) were designed that could move freely in a 2D workspace. The key aspect of local magnetic field control enabled the independent actuation of multiple robots in the workspace. These robots were under closed-loop control in the workspace on paths generated by path planning algorithms considering LTL specifications (Chapter 4), Potential Field based MDP planning (Chapter 5) and A* planning (Chapter 6). The robots were also designed to ensure that both position and orientation of the robot could be controlled in the workspace.

In Chapter 4, a mm-scale local magnetic field generating system used to control 3.175 *mm* size N52 magnets as robots independently in the workspace. The controller used a set of local equilibrium points that were generated from a sequence of coil currents around the robots from one state to the next. The robots moved along paths computed through optimal control synthesis approach to solve complex micromanipulation tasks captured by global LTL formulas. However, the use of local equilibrium points as the states limited the motion of the robot in the workspace to simple tasks. Also, the interaction between the robots limited the robots to stay within far distances with each other.

In Chapter 5, the mm-scale coils are modeled extensively to understand the forces generated by various coil combinations of the array, and solutions for different actuation force directions are discovered. The path planning problem is formulated as a Markov decision process that solves a policy to reach a goal from any location in the workspace. The MDP formulation is also expanded to work when other robots are

present in the workspace. The formulation considers the interaction force between the robots and changes the policy to reach the goal location. However, the experiments presented consider only a stationary second robot in the workspace.

In Chapter 6, a microscale local magnetic field system was investigated. This system used $8 \times 8$ small strips of wire aligned in a single layer that could be independently controlled. The coils in this system couldn't actuate the proposed 1mm robots successfully in X and Y axes. Hence a new microscale local magnetic field system which consisted of two $8 \times 8$ array of coils aligned in two axes in two layers of a PCB was designed. The newly designed system is able to generate localized magnetic field gradients in orthogonal directions in the plane. The microcoils in the second layer are also able to generate sufficient magnetic field gradients in the workspace, while the traces below it are spaced adequately to eliminate their influence in the workspace. A new microrobot design enabled the orientation control of the microrobot for performing micromanipulation tasks. However, due to the magnetic nature of the robots, not more than two robots could be independently actuated in the workspace.

In pursuit of actuation smaller and multiple robots in a small workspace, a serpentine coil based local magnetic field generating system was designed in Chapter 7. This system is capable of simultaneous independent control of up to 4 microrobots. The main driver of each robot is a neodymium 250 $\mu m$ N50 cube magnet which is attached to a 3D printed part for stability and orientation control. The overall robot is sized 1 $mm \times 1$ $mm$ in size and is painted to get feedback of its position and orientation for closed loop control. The smaller sized magnets decreased the interaction forces between the robots compared to Chapter 6. The motion of the robot using the coils resembled that of a stepper motor which enabled the use of sine-cosine functions to specify currents in the coils for smooth motion of the microrobot in the workspace. The experiments demonstrated the capability of the microrobot and platform to simultaneously actuate up to four robots independently and successfully perform manipulation tasks. The ability to control the orientation of the robot in place is also demonstrated that has improved ability to perform manipulation tasks.

## 8.2 Contributions

The key contributions from this dissertation are listed below:

- The modeling of the magnetic field and gradients to identify forces generated on permanent magnets in the workspace. Analysis of surface forces on the robot helped in identifying size and magnetization of magnets used to design robots in the workspace (Chapter 2).

- An experimental test-bed was developed to test the different local magnetic field generating systems. The electronics consisted of a set of eight current control boards which could each control the magnitude and direction of 16 coils independently. An I2C interface helped communicate with these 128 coils through an Arduino microcontroller. Software like Matlab and Visual Studio were used to get transmit user commands to the microcontroller to actuate the robots. The closed loop control methods used feedback information of position and orientation of the robot through processing images captured through the camera (Chapter 3).

- Using local equilibrium points for actuation in the mm scale v1 and v2 local magnetic field generating system. Planning for microrobot motion in the workspace and executing planned paths from a optimal control synthesis approach (Chapter 4).

- The mm Scale v1 system was able to actuate only three robots independently in the workspace due to manufacturing issues and was redesigned to form a larger workspace with robust activation of coils for actuation which resulted in independent actuation of four robots in the workspace (Chapter 4).

- The advanced modeling of the coils to provide smooth motion for the robot in the workspace. The use of interaction force models ensured that the interactions between the robots were used to determine appropriate actions for the robot to reach its goal location (Chapter 5).

- The design of the microcoil array which involved a ten layer PCB board with 128 microcoils wired to be actuated independently. This local magnetic field generating system could provide smooth motions in the workspace for robots as small as 1 $mm$ and independently control up to two robots in the workspace (Chapter 6).

- The newly designed robot enabled orientation control of the robot in the workspace which improved the ability of the robot to perform manipulation tasks (Chapter 6).

- The design of the serpentine coil system resulted in the actuation of microrobots as small as 750 $\mu m$. The new robot design also enabled the orientation control of the robot in the workspace. The zonal nature of the coils required new strategies for robots to cross quadrants. The robots were also used to push objects in the workspace and independent actuation of four microrobots were demonstrated (Chapter 7).

- The first demonstration of independent, closed-loop position and orientation control of multiple (four) magnetic microrobots using local magnetic fields (Chapter 7).

## 8.3 Future Work

Many aspects of the design of local magnetic field actuation system for multirobot actuation can be improved. The work presented in this dissertation is a good reference for designing actuation systems at this scale. Some areas of potential future work are presented in this section.

### 8.3.1 Local Magnetic Field Generating System Design

The system that is the best representation of the objectives of this dissertation is the serpentine coil based local magnetic field generating system. The independent

control of 4 microrobots in the 4 zones of the workspace is ideal for manipulation tasks in this scale. However, the limitations in flexible PCB manufacturing limits the number of zones to 4, and hence the independent control of four microrobots. In future, by use of multilayer PCBs, the number of zones can be increased. For larger robots (1 $mm$ N52 disc magnet based), the expanded coil design presented in Sec. 6.9 could enable independent control of up to 8 robots in the 8 zones.

### 8.3.2 Microrobot Design

In future, other end-effectors types can be designed that provide specific functions such as force sensing or payload delivery to such robots. The robot design can also be improved to make the true size of robot closer to 250 $\mu m$ while achieving stable position and orientation control in the workspace. This could be possible by using other denser materials for shifting the center of mass and for supporting the robot from tipping efficiently.

### 8.3.3 Path Planning

Path planning to find optimal trajectories to manipulate the objects and the implementation of multiple robots in the same workspace performing parallel tasks are also areas of future work. Also, the MDP formulation can be expanded to include the trajectory of other moving robots in the workspace. The computation of the policy takes $\approx 100$ seconds to complete which makes it hard to implement in real time applications, which could be solved by using faster planners which use the interaction force models.

### 8.3.4 Workspace Environment and Applications

Another area of future work is expanding these solutions to other liquids (other than silicone oil), dry surfaces or gel media conditions for applications in manufac-

turing and biology. The use of flexible PCBs can also facilitate the manufacturing of the serpentine coils on thin films that can be easily adapted to microscope surfaces.

# REFERENCES

# REFERENCES


[1] M. Sitti, H. Ceylan, W. Hu, J. Giltinan, M. Turan, S. Yim, and E. Diller. Biomedical applications of untethered mobile milli/microrobots. *Proceedings of the IEEE*, 103(2):205–224, Feb 2015.

[2] D. Cappelleri, D. Efthymiou, A. Goswami, N. Vitoroulis, and M. Zavlanos. Towards mobile microrobot swarms for additive micromanufacturing. *International Journal of Advanced Robotic Systems*, 11(150), 2014. DOI: 10.5772/58985.

[3] G. Yang, J. A. Gaines, and B. J. Nelson. A supervisory wafer-level 3d microassembly system for hybrid mems fabrication. *Journal of Intelligent and Robotic Systems*, 37(1):43–68, 2003.

[4] D. O. Popa and H. E. Stephanou. Micro and mesoscale robotic assembly. *Journal of manufacturing processes*, 6(1):52–71, 2004.

[5] D. J. Cappelleri and Z. Fu. Towards flexible, automated microassembly with caging micromanipulation. In *2013 IEEE International Conference on Robotics and Automation*, pages 1427–1432, May 2013.

[6] D. Cappelleri, C. Peng, J. Fink, B. Gavrea, and V. Kumar. Automated assembly for meso-scale parts. *IEEE Transactions on Automation Science and Engineering*, 8(3):598–613, July 2011.

[7] J. Wason, J. Wen, J. Gorman, and N. Dagalakis. Automated multiprobe microassembly using vision feedback. *Robotics, IEEE Transactions on*, 28(5):1090 –1103, oct. 2012.

[8] D. J. Cappelleri and Z. Fu. Cooperative micromanipulators for 3d micromanipulation and assembly. In *ASME 2012 International Design Engineering Technical Conferences and Computers and Information in Engineering Conference*, pages 177–185. American Society of Mechanical Engineers, 2012.

[9] D. J. Cappelleri, G. Piazza, and V. Kumar. A two dimensional vision-based force sensor for microrobotic applications. *Sensors and Actuators A: Physical*, 171(2):340–351, 2011.

[10] D. J. Cappelleri, M. Fatovic, and Z. Fu. Caging grasps for micromanipulation & microassembly. In *Intelligent Robots and Systems (IROS), 2011 IEEE/RSJ International Conference on*, pages 925–930. IEEE, 2011.

[11] G. Yang, J. A. Gaines, and B. J. Nelson. Optomechatronic design of microassembly systems for manufacturing hybrid microsystems. *IEEE Transactions on Industrial Electronics*, 52(4):1013–1023, Aug 2005.

[12] N. Dechev, W. Cleghorn, and J. Mills. Microassembly of 3-d microstructures using a compliant, passive microgripper. *Microelectromechanical Systems, Journal of*, 13(2):176 – 189, april 2004.

[13] D. Popa, W. H. Lee, R. Murthy, A. Das, and H. Stephanou. High yield automated mems assembly. In *Automation Science and Engineering, 2007. CASE 2007. IEEE International Conference on*, pages 1099 –1104, sept. 2007.

[14] L. Ren, L. Wang, J. Mills, and D. Sun. 3-d automatic microassembly by vision-based control. In *Intelligent Robots and Systems, 2007. IROS 2007. IEEE/RSJ International Conference on*, pages 297 –302, 29 2007-nov. 2 2007.

[15] K. Rabenorosoa, C. Clevy, P. Lutz, S. Bargiel, and C. Gorecki. A microassembly station used for 3d reconfigurable hybrid moems assembly. In *Assembly and Manufacturing, 2009. ISAM 2009. IEEE International Symposium on*, pages 95 –100, nov. 2009.

[16] B. Tamadazte, N. Le Fort-Piat, S. Dembele, and E. Marchand. Microassembly of complex and solid 3d mems by 3d vision-based control. In *Intelligent Robots and Systems, 2009. IROS 2009. IEEE/RSJ International Conference on*, pages 3284 –3289, oct. 2009.

[17] A. Hsu, W. Chu, C. Cowan, B. McCoy, A. Wong-Foy, R. Pelrine, J. Lake, J. Ballard, and J. Randall. Diamagnetically levitated milli-robots for heterogeneous 3d assembly. *Journal of Micro-Bio Robotics*, 14(1-2):1–16, 2018.

[18] B. J. Nelson, I. K. Kaliakatsos, and J. J. Abbott. Microrobots for minimally invasive medicine. *Annual review of biomedical engineering*, 12:55–85, 2010.

[19] J. Li, B. E.-F. de Ávila, W. Gao, L. Zhang, and J. Wang. Micro/nanorobots for biomedicine: Delivery, surgery, sensing, and detoxification. *Science Robotics*, 2(4), 2017.

[20] W. Andr and C. Werner. *Remote-Controlled Drug Delivery in the Gastrointestinal Tract*, chapter 4.3, pages 499–510. John Wiley & Sons, Ltd, 2007.

[21] V. Magdanz, S. Sanchez, and O. G. Schmidt. Development of a sperm-flagella driven micro-bio-robot. *Advanced Materials*, 25(45):6581–6588, 2013.

[22] S. Byun, J.-M. Lim, S.-J. Paik, A. Lee, K.-i. Koo, S. Park, J. Park, B.-D. Choi, J. M. Seo, K.-a. Kim, et al. Barbed micro-spikes for micro-scale biopsy. *Journal of Micromechanics and Microengineering*, 15(6):1279, 2005.

[23] O. Ergeneman, G. Dogangil, M. P. Kummer, J. J. Abbott, M. K. Nazeeruddin, and B. J. Nelson. A magnetically controlled wireless optical oxygen sensor for intraocular measurements. *IEEE Sensors Journal*, 8(1):29–37, 2008.

[24] H. Zhang, D. W. Hutmacher, F. Chollet, A. N. Poo, and E. Burdet. Microrobotics and mems-based fabrication techniques for scaffold-based tissue engineering. *Macromolecular bioscience*, 5(6):477–489, 2005.

[25] J. Abbott, Z. Nagy, F. Beyeler, and B. Nelson. Robotics in the small. *IEEE Robotics and Automation Magazine*, 14:92–103, 2007.

[26] M. Sitti. Miniature devices: Voyage of the microrobots. *Nature*, 458(7242):1121–1122, 2009.

[27] M. Sitti. Microscale and nanoscale robotics systems [grand challenges of robotics]. *Robotics Automation Magazine, IEEE*, 14(1):53–60, March 2007.

[28] E. Diller, M. Sitti, et al. Micro-scale mobile robotics. *Foundations and Trends in Robotics*, 2(3):143–259, 2013.

[29] J. J. Abbott, M. C. Lagomarsino, L. Zhang, L. Dong, and B. J. Nelson. How should microrobots swim? *The international journal of Robotics Research*, 2009.

[30] S. Martel. Microrobotics in the vascular network: present status and next challenges. *Journal of Micro-Bio Robotics*, 8(1):41–52, 2013.

[31] S. Martel. Magnetic therapeutic delivery using navigable agents. *Therapeutic delivery*, 5(2):189–204, 2014.

[32] S. Martel. Magnetic nanoparticles in medical nanorobotics. *Journal of Nanoparticle Research*, 17(2):1–15, 2015.

[33] S. Chowdhury, W. Jing, and D. Cappelleri. Controlling multiple microrobots: recent progress and future challenges. *Journal of Micro-Bio Robotics*, pages 1–11, 2015.

[34] S. Hollar, A. Flynn, C. Bellew, and K. S. J. Pister. Solar powered 10 mg silicon robot. In *The Sixteenth Annual International Conference on Micro Electro Mechanical Systems, 2003. MEMS-03 Kyoto. IEEE*, pages 706–711, Jan 2003.

[35] B. R. Donald, C. G. Levey, C. D. McGray, I. Paprotny, and D. Rus. An untethered, electrostatic, globally controllable mems micro-robot. *Journal of Microelectromechanical Systems*, 15(1):1–15, Feb 2006.

[36] O. J. Sul, M. R. Falvo, R. M. T. II, S. Washburn, and R. Superfine. Thermally actuated untethered impact-driven locomotive microdevices. *Applied Physics Letters*, 89(20):203512, 2006.

[37] E. Y. Erdem, Y. M. Chen, M. Mohebbi, J. W. Suh, G. T. A. Kovacs, R. B. Darling, and K. F. Bohringer. Thermally actuated omnidirectional walking microrobot. *Journal of Microelectromechanical Systems*, 19(3):433–442, June 2010.

[38] M. Pac and D. Popa. Laser-powered sub-mm untethered microrobotics. In *Proceedings of the ASME 2010 International Design Engineering Technical Conferences & Computers and Information in Engineering Conference, Montreal, Canada*, 2010.

[39] H. Chen and D. Sun. Moving groups of microparticles into array with a robot tweezers manipulation system. *IEEE Transactions on Robotics*, 28(5):1069–1080, Oct 2012.

[40] W. Hu, K. S. Ishii, and A. T. Ohta. Micro-assembly using optically controlled bubble microrobots in saline solution. In *2012 IEEE International Conference on Robotics and Automation*, pages 733–738, May 2012.

[41] S. Chowdhury, P. Švec, C. Wang, K. T. Seale, J. P. Wikswo, W. Losert, and S. K. Gupta. Automated cell transport in optical tweezers-assisted microfluidic chambers. *IEEE Transactions on Automation Science and Engineering*, 10(4):980–989, 2013.

[42] S. Chowdhury, A. Thakur, P. Švec, C. Wang, W. Losert, and S. Gupta. Automated manipulation of biological cells using gripper formations controlled by optical tweezers. *IEEE Transactions on Automation Science and Engineering*, 11(2):338–347, April 2014.

[43] K. Oldham, R. Choong-Ho, R. Jeong-Hoon, R. Polcawich, and J. Pulskamp. Lateral thin-film piezoelectric actuators for bio-inspired micro-robotic locomotion. In *Proceedings of the ASME 2009 International Design Engineering Technical Conferences & Computers and Information in Engineering Conference, San Diego, CA, USA*, 2009.

[44] N. Darnton, L. Turner, K. Breuer, and H. Berg. Moving fluid with bacterial carpets. *Biophysical Journal*, 86:1863–1870, 2004.

[45] B. Behkam and M. Sitti. Design methodology for biomimetic propulsion of miniature swimming robots. *Journal of Dynamic Systems, Measurement, and Control*, 128(1):36–43, 2006.

[46] E. B. Steager, J. A. Patel, C.-B. Kim, D. K. Yi, W. Lee, and M. J. Kim. A novel method of microfabrication and manipulation of bacterial teamsters in low reynolds number fluidic environments. *Microfluidics and Nanofluidics*, 5(3):337–346, 2008.

[47] S. Martel, O. Felfoul, J.-B. Mathieu, A. Chanu, S. Tamaz, M. Mohammadi, M. Mankiewicz, and N. Tabatabaei. Mri-based medical nanorobotic platform for the control of magnetic nanoparticles and flagellated bacteria for target interventions in human capillaries. *The International journal of robotics research*, 28(9):1169–1182, 2009.

[48] D. Kim, A. Liu, E. Diller, and M. Sitti. Chemotactic steering of bacteria propelled microbeads. *Biomedical microdevices*, 14(6):1009–1017, 2012.

[49] K. Vollmers, D. R. Frutiger, B. E. Kratochvil, and B. J. Nelson. Wireless resonant magnetic microactuator for untethered mobile microrobots. *Applied Physics Letters*, 92(14):144103, 2008.

[50] C. Pawashe, S. Floyd, and M. Sitti. Modeling and experimental characterization of an untethered magnetic micro-robot. *The International Journal of Robotics Research*, 28(8):1077–1094, 2009.

[51] G.-L. Jiang, Y.-H. Guu, C.-N. Lu, P.-K. Li, H.-M. Shen, L.-S. Lee, J. A. Yeh, and M. T.-K. Hou. Development of rolling magnetic microrobots. *Journal of Micromechanics and Microengineering*, 20(8):085042, 2010.

[52] I. A. Ivan, G. Hwang, J. Agnus, M. Rakotondrabe, N. Chaillet, and S. R?gnier. First experiments on magpier: A planar wireless magnetic and piezoelectric microrobot. In *2011 IEEE International Conference on Robotics and Automation*, pages 102–108, May 2011.

[53] B. R. Donald, C. G. Levey, C. D. McGray, D. Rus, and M. Sinclair. Power delivery and locomotion of untethered microactuators. *Journal of Microelectromechanical Systems*, 12(6):947–959, Dec 2003.

[54] B. R. Donald, C. G. Levey, I. Paprotny, and D. Rus. Planning and control for microassembly of structures composed of stress-engineered mems microrobots. *The International Journal of Robotics Research*, 32(2):218–246, 2013. PMID: 23580796.

[55] R. Zhang, A. Sherehiy, Z. Yang, D. Wei, C. K. Harnett, and D. O. Popa. Chevbot an untethered microrobot powered by laser for microfactory applications. In *2019 International Conference on Robotics and Automation (ICRA)*, pages 231–236, May 2019.

[56] A. G. Banerjee, S. Chowdhury, W. Losert, and S. K. Gupta. Real-time path planning for coordinated transport of multiple particles using optical tweezers. *IEEE Transactions on Automation Science and Engineering*, 9(4):669 –678, Oct 2012.

[57] A. Banerjee, S. Chowdhury, and S. Gupta. Optical tweezers: Autonomous robots for the manipulation of biological cells. *IEEE Robotics Automation Magazine*, 21(3):81–88, Sept 2014.

[58] C. C. Cheah, Q. M. Ta, and R. Haghighi. Robotic manipulation of a biological cell using multiple optical traps. In *Robotics and Automation (ICRA), 2015 IEEE International Conference on*, pages 803–808, May 2015.

[59] U. K. Cheang and M. J. Kim. Self-assembly of robotic micro-and nanoswimmers using magnetic nanoparticles. *Journal of Nanoparticle Research*, 17(3):1–11, 2015.

[60] S. Chowdhury, P. Svec, C. Wang, K. Seale, J. P. Wikswo, W. Losert, and S. K. Gupta. Automated cell transport in optical tweezers assisted microfluidic chamber. *IEEE Trans. Autom. Sci. Eng.*, 10(4):980–989, Oct. 2013.

[61] S. Hu and D. Sun. Automated transportation of biological cells with a robot-tweezer manipulation system. *Int. J. Robot. Res.*, 30(14):1681–1694, Dec. 2011.

[62] M. A. Rahman, J. Cheng, Z. Wang, and A. T. Ohta. Cooperative micromanipulation using the independent actuation of fifty microrobots in parallel. *Scientific Reports*, 7, 2017.

[63] A. Thakur, S. Chowdhury, P. Švec, C. Wang, W. Losert, and S. K. Gupta. Indirect pushing based automated micromanipulation of biological cells using optical tweezers. *The International Journal of Robotics Research*, page 0278364914523690, 2014.

[64] Y. Alapan, O. Yasa, B. Yigit, I. C. Yasa, P. Erkoc, and M. Sitti. Microrobotics and microorganisms: Biohybrid autonomous cellular robots. *Annual Review of Control, Robotics, and Autonomous Systems*, 2(1):205–230, 2019.

[65] M. P. Kummer, J. J. Abbott, B. E. Kratochvil, R. Borer, A. Sengul, and B. J. Nelson. Octomag: An electromagnetic system for 5-dof wireless micromanipulation. *Robotics, IEEE Transactions on*, 26(6):1006–1017, 2010.

[66] S. Floyd, C. Pawashe, and M. Sitti. An untethered magnetically actuated microrobot capable of motion on arbitrary surfaces. In *Robotics and Automation, 2008. ICRA 2008. IEEE International Conference on*, pages 419–424. IEEE, 2008.

[67] W. Jing, X. Chen, S. Lyttle, Z. Fu, Y. Shi, and D. J. Cappelleri. Design of a micro-scale magnetostrictive asymmetric thin film bimorph ($\mu$mab) microrobot. In *ASME 2010 International Mechanical Engineering Congress and Exposition*, pages 599–607. American Society of Mechanical Engineers Digital Collection, 2010.

[68] W. Jing, X. Chen, S. Lyttle, Z. Fu, Y. Shi, and D. Cappelleri. A magnetic thin film microrobot with two operating modes. In *2011 IEEE International Conference on Robotics and Automation (ICRA)*, pages 96–101, May 2011.

[69] W. Jing and D. Cappelleri. Incorporating in-situ force sensing capabilities in a magnetic microrobot. In *2014 IEEE/RSJ International Conference on Intelligent Robots and Systems (IROS 2014)*, pages 4704–4709, Sept 2014.

[70] W. Jing and D. Cappelleri. A magnetic microrobot with in situ force sensing capabilities. *Robotics*, 3(2):106–119, 2014.

[71] E. B. Steager, M. S. Sakar, C. Magee, M. Kennedy, A. Cowley, and V. Kumar. Automated biomanipulation of single cells using magnetic microrobots. *The International Journal of Robotics Research*, 32(3):346–359, 2013.

[72] E. Diller, J. Giltinan, G. Z. Lum, Z. Ye, and M. Sitti. Six-degree-of-freedom magnetic actuation for wireless microrobotics. *The International Journal of Robotics Research*, 35(1-3):114–128, 2016.

[73] W. Jing, N. Pagano, and D. J. Cappelleri. A novel micro-scale magnetic tumbling microrobot. *Journal of Micro-Bio Robotics*, 8(1):1–12, 2013.

[74] W. Jing and D. J. Cappelleri. Towards functional mobile magnetic microrobots. In *Small-Scale Robotics. From Nano-to-Millimeter-Sized Robotic Systems and Applications*, pages 81–100. Springer, 2014.

[75] M. Sitti. *Mobile Microrobotics*. Intelligent Robotics and Autonomous Agents series. MIT Press, 2017.

[76] SuperMagnetMan. *Micro Magnets*.

[77] J. Zhang, M. Salehizadeh, and E. Diller. Parallel pick and place using two independent untethered mobile magnetic microgrippers. In *2018 IEEE International Conference on Robotics and Automation*, May 2018.

[78] I. S. M. Khalil, A. F. Tabak, Y. Hamed, M. Tawakol, A. Klingner, N. E. Gohary, B. Mizaikoff, and M. Sitti. Independent actuation of two-tailed microrobots. *IEEE Robotics and Automation Letters*, 3(3):1703–1710, July 2018.

[79] E. Diller, C. Pawashe, S. Floyd, and M. Sitti. Assembly and disassembly of magnetic mobile micro-robots towards deterministic 2-d reconfigurable microsystems. *The International Journal of Robotics Research*, 2011.

[80] E. Diller, S. Floyd, C. Pawashe, and M. Sitti. Control of multiple heterogeneous magnetic microrobots in two dimensions on nonspecialized surfaces. *IEEE Transactions on Robotics*, 28(1):172–182, 2012.

[81] D. R. Frutiger, K. Vollmers, B. E. Kratochvil, and B. J. Nelson. Small, fast, and under control: wireless resonant magnetic micro-agents. *The International Journal of Robotics Research*, 29(5):613–636, 2010.

[82] D. DeVon and T. Bretl. Control of many robots moving in the same direction with different speeds: a decoupling approach. In *American Control Conference, 2009. ACC'09.*, pages 1794–1799. IEEE, 2009.

[83] D. Wong, J. Wang, E. Steager, and V. Kumar. Control of multiple magnetic micro robots. In *Proceedings of the ASME 2015 International Design Engineering Technical COnferences & Computers and Information in Engineering Conference*, Boston, Massachusetts, USA, August 2 -5 2015.

[84] M. Salehizadeh and E. Diller. Two-agent formation control of magnetic microrobots. In *2016 International Conference on Manipulation, Automation and Robotics at Small Scales (MARSS)*, pages 1–6, July 2016.

[85] T. Inoue, K. Iwatani, I. Shimoyama, and H. Miura. Micromanipulation using magnetic field. In *Robotics and Automation, 1995. Proceedings., 1995 IEEE International Conference on*, volume 1, pages 679–684. IEEE, 1995.

[86] R. Pelrine, A. Wong-Foy, B. McCoy, D. Holeman, R. Mahoney, G. Myers, J. Herson, and T. Low. Diamagnetically levitated robots: An approach to massively parallel robotic systems with unusual motion properties. In *2012 IEEE International Conference on Robotics and Automation (ICRA),*, pages 739–744, 2012.

[87] A. Beyzavi and N.-T. Nguyen. Modeling and optimization of planar microcoils. *Journal of Micromechanics and Microengineering*, 18(9):095018, 2008.

[88] Y. Kantaros, B. V. Johnson, S. Chowdhury, D. J. Cappelleri, and M. M. Zavlanos. Control of magnetic microrobot teams for temporal micromanipulation tasks. *IEEE Transactions on Robotics*, pages 1–18, 2018.

[89] S. Chowdhury, W. Jing, and D. J. Cappelleri. Independent actuation of multiple microrobots using localized magnetic fields. In *Manipulation, Automation and Robotics at Small Scales (MARSS), International Conference on*, pages 1–6. IEEE, 2016.

[90] S. Chowdhury, W. Jing, P. Jaron, and D. Cappelleri. Path planning and control for autonomous navigation of single and multiple magnetic mobile microrobots. In *Proceedings of the ASME 2015 International Design Engineering Technical Conferences & Computers and Information in Engineering Conference*, Boston, Massachusetts, USA, August 2-5 2015.

[91] S. Chowdhury, W. Jing, and D. J. Cappelleri. Towards independent control of multiple magnetic mobile microrobots. *Micromachines*, 7(1):3, 2015.

[92] B. V. Johnson and D. J. Cappelleri. Modeling, control and planning for multiple mobile microrobots. In *Proceedings of the ASME 2019 International Design Engineering Technical Conferences & Computers and Information in Engineering Conference*, Anaheim, California, USA, August 18-21 2019.

[93] O. Sigaud and O. Buffet. *Markov decision processes in artificial intelligence*. John Wiley & Sons, 2013.

[94] R. Bellman. The theory of dynamic programming. *Bulletin of the American Mathematical Society*, 60(6):503–515, 1954.

[95] I. Chadès, G. Chapron, M.-J. Cros, F. Garcia, and R. Sabbadin. Mdptoolbox: a multi-platform toolbox to solve stochastic dynamic programming problems. *Ecography*, 37(9):916–920, 2014.

[96] G. Akoun and J.-P. Yonnet. 3d analytical calculation of the forces exerted between two cuboidal magnets. *IEEE Transactions on magnetics*, 20(5):1962–1964, 1984.

[97] B. V. Johnson, S. Chowdhury, and D. J. Cappelleri. Local magnetic field design and characterization for independent closed-loop control of multiple mobile microrobots. *IEEE/ASME Transactions on Mechatronics*, 25(2):526–534, April 2020.

[98] S. Chowdhury, B. V. Johnson, W. Jing, and D. J. Cappelleri. Designing local magnetic fields and path planning for independent actuation of multiple mobile microrobots. *Journal of Micro-Bio Robotics*, 12(1-4):21–31, 2017.

[99] R. Pelrine, A. Hsu, and A. Wong-Foy. Methods and results for rotation of diamagnetic robots using translational designs. In *2019 International Conference on Manipulation, Automation and Robotics at Small Scales (MARSS)*, pages 1–6, July 2019.

[100] Zaber Technologies Inc. *Microstepping Tutorial*.

[101] G. Adam and D. J. Cappelleri. Design of a 3d vision-based micro-force sensing probe. In *2019 International Conference on Manipulation, Automation and Robotics at Small Scales (MARSS)*, pages 1–6, July 2019.

VITA

# VITA

Benjamin V Johnson was born in Kerala, India. During his childhood, he had his schooling done in Kochi (India), Muscat (Oman), and Chennai (India). He obtained his Bachelor of Technology in Mechanical Engineering from the Indian Institute of Technology Guwahati, Assam, India, and was awarded the Honda Young Engineer and Scientist Award in 2012. He joined Purdue University in 2013 to pursue Master of Science in Mechanical Engineering. His master's thesis was supervised by Prof. David J. Cappelleri and was on the design of robotic surgical tools for lumbar discectomy surgical procedures. He continued his graduate studies with Prof. Cappelleri on the doctoral work on the design of microrobot platforms to actuate multiple robots independently. His research work during graduate school resulted in several publications in international conferences and journals. Benjamin was also a recipient of the Bilsland Dissertation Fellowship from the Purdue Graduate School which is awarded to outstanding Ph.D. students at Purdue in their final year of study.